PHYSICAL IMMOBILIZATION OF PHOTOSYSTEM I (PSI) AT SELF-ASSEMBLED

MONOLAYERS ON GOLD: DIRECTED ADSORPTION, ELECTRON TRANSFER, AND

BIOMIMETIC ENTRAPMENT

By

Helen A. Kincaid

Dissertation

Submitted to the Faculty of the

Graduate School of Vanderbilt University

in partial fulfillment of the requirements

for the degree of

DOCTOR OF PHILOSOPHY

in

Chemical Engineering

May, 2006

Nashville, Tennessee

Approved:

Professor G. Kane Jennings

Professor M. Douglas LeVan

Professor Bridget Rogers

Professor Peter T. Cummings

Professor David E. Cliffel

To my beloved father, James H. Kincaid, whose vision made me successful at any

endeavor

and

To my wonderful mother, Nancy H. Kincaid, who is infinitely supportive and generous

ACKNOWLEDGEMENTS

I am especially indebted to my advisor Dr. G. Kane Jennings, who made my graduate school experience enjoyable. I couldn't have asked for a better advisor. Dr. Jennings has a real passion for his career and it shows in his teaching and mentoring. I thank him for his many hours of regular meeting times and his time beyond that with organization of group activities. I thank the group members, Dr. Eric Brantley, Dongshun Bai, Brad Berron, and Chris Faulkner for all of their help, support, and friendship. I will always remember and value my time in the Jennings group. I especially thank Tom Niedringhaus, a Vanderbilt undergraduate student participating in the Vanderbilt Undergraduate Summer Research Program, and Megan Weick, an undergraduate participating in the VINSE summer program, for their contributions to this project.

I thank all of my committee members, Dr. LeVan, Dr. Peter Cummings, Dr. Cliffel, and Dr. Rogers for their suggestions and advice. I especially thank Dr. Rogers for her great listening skills and for her resourcefulness anytime I happened to drop by her office. Thanks to Dr. LeVan for being so gracious and helpful. I will always be in awe of his ability to lecture without notes. Thanks to Dr. Cummings for his

TABLE OF CONTENTS

LIST OF TABLES

LIST OF FIGURES

xi

CHAPTER I

INTRODUCTION

The Energy Crisis

Researchers and engineers have been intrigued with the concept of converting light into electrical power since the discovery of the photoelectric effect[1] by Becquerel in 1839.[2] The amount of energy supplied by the sun (165,000 terawatts (TW) or 165,000 x 10^{12} watts)[3] is more than 10,000 times greater than mankind's energy consumption (~ 12 TW[4] to 14.5 TW[3]). In other words, if solar cells with 10% efficiency covered only 0.16% of the Earth, our consumption needs could be fulfilled.[5] Currently, 85%[4] of the world's energy demand is being met primarily through the use of fossil fuels. Not only are we depleting our fossil fuels rapidly, our consumption of these fuels is contributing to global warming through an increase in the production of carbon dioxide.[6] In a recent report by Rignot and Kanagaratnam[7] of NASA's Jet Propulsion Laboratory and the Center for Remote Sensing of Ice Sheets, respectively, Greenland's glaciers have discharged more than twice as much ice in 2005 as they did in 1996 (enough water to supply all of Los Angeles for 220 years) most likely because of global warming. Along with the issues associated with the rapid use of fossil fuels, comes the issue of peak production of crude oil. If the world population reaches 10 billion people and we assume that each person would require a couple of kilowatt-hours per person on average, then 60 TW would need to be generated worldwide, the equivalent of 900 million barrels of oil per day. This

demand will far surpass the present capabilities of oil production[3] estimated at 72 million barrels per day in 2004.[8]

Other alternatives to fossil fuels account for a very small percentage of the world-wide energy mix. In 2004, renewable energy contributed only 8% and nuclear electric power 6%.[8] In order to decrease the dependence on fossil fuels, a radical increase in the contributions of alternative energy sources is needed. However, the capabilities of hydroelectric, wind, geothermal, and nuclear do not appear promising. The theoretical capabilities of hydroelectric power are less than 2 TW and ~ 2 - 4 TWe (terawatt electric) for wind power.[5] In order to produce 10 TW of power by nuclear power, a 1-GWe (gigawatt electric) reactor would need to be constructed every other day for the next 50 years.[5] Even if all of the nuclear power plants desired were constructed, the reserves of uranium would only last for a minimum of six years.[4] With the exception of solar energy, various alternatives to fossil fuels cannot meet the future energy.

Current solar cells are dominated by single-crystal[9] and polycrystalline silicon modules, called first generation photovoltaics, with costs higher than that of fossil fuel derived energy.[10] If solar cells are to be competitive with the current costs of energy derived from fossil fuels, the efficiencies and/or the materials of construction must be improved. Second generation photovoltaics focus on reducing the cost of the materials of construction at the expense of reduced efficiencies, while third generation photovoltaics concentrate on improving efficiency at the expense of high cost materials and fabrication.[5, 10] The second generation photovoltaics include organic-based devices such as dye-sensitized[11] nanostructured oxide cells, multilayer devices of small molecule organic semiconductors,[12-14] organic-inorganic composites,[15] organic-inorganic

composites with nanocrystals of conventional semiconductors,[16] and conjugated polymers with liquid electrolyte.[17] Current organic photovoltaics are not efficient at harvesting red photons,[10] which contain a significant fraction of the energy in the solar spectrum; however, nature's photoelectrochemical devices, plants, have optimized their conversion of solar energy utilizing red photons.

In order to gain an enhanced understanding of the optimum conversion of solar energy, we could examine the fundamental basis in which nature converts sunlight into useful chemical energy. If we could harness the energy-converting center of plants, thereby reducing the size of the active component to the nanoscale-level, and integrate it with a device, we could theoretically meet energy consumption needs with much less space required as well as a significant improvement over current photovoltaics in cost. The preparation of such a device would require significant advances in nanoscale science and engineering.

Nanotechnology has received much attention in the past decade with a high percentage of that focused on "bottom-up" processing. Many aspects of current research examine the integration of biological nanostructures with organic materials at a surface, particularly through the use of self-assembled monolayers (SAMs). Immobilization of biological nanostructures on a surface, while maintaining functionality, can prove useful for a variety of devices such as chemical and biological sensors. Many proteins will adsorb nonspecifically on a surface and lose biological functionality, believed to be due in part to the binding of various regions on the protein, which alters its orientation and structure.[18] The use of self-assembled monolayers (SAMs) allows for a more controlled adsorption of proteins through physical and chemical binding events.[19-27]

Self-Assembled Monolayers (SAMs)

Langmuir[28]-Blodgett[29] (LB) monolayers represented one of the earliest methods for the preparation of an organic monolayer on a substrate. LB monolayers are formed by spreading an insoluble compound on an aqueous subphase, compressing the film, and then transferring the monolayer to a solid substrate.[30] This type of monolayer is still being used, but the process does suffer from several drawbacks, including lack of film stability since the molecules are not chemically bonded to the substrate, requirement of a clean room to minimize the effects of dust, and restriction to compounds that can form films on water and be transferred intact to a substrate.[30]

In the early 1980s, Nuzzo and Allara[31] developed a more versatile and robust method, through chemisorption, for forming organic monolayers on substrates using simple immersion in solution. Alkanethiols ($X(CH_2)_nSH$), dialkyl disulfides ($X(CH_2)_mS-S(CH_2)_nX$), and dialkyl sulfides ($X(CH_2)_mS(CH_2)_nX$), where n and m are the number of methylene units and X is the terminal group, chemisorb onto gold surfaces to form densely packed monomolecular films referred to as self-assembled monolayers (SAMs). The adsorption of thiols into SAMs can also occur on silver, copper, mercury, GaAs, and InP, but the preferred surface is gold since it does not readily oxidize or contaminate after exposure to air.[32, 33] Alkyltrichlorosilanes can be used for the formation of monolayers on glass[31] or silicon[34, 35] and can also be used to form multilayers.[36]

The adsorption and growth of a SAM from alkanethiols on Au (111) can be summarized by the initial stage of adsorption as a physisorbed state, with the thiol molecules lying almost parallel to the surface followed by a chemisorption to the gold surface through a thiolate bond by the reaction

$$RS\text{-}H + Au_n^0 \rightarrow RS^-Au^+ \bullet Au_n^0 + \tfrac{1}{2} H_2 \qquad\qquad (1\text{-}1)$$

where the S-H bond is cleaved and the thiolate occupies a three-fold hollow site on Au (111) surfaces.[33, 37] The very early stages of adsorption of thiolates on a substrate can be thought of as disorganized and isolated, eventually transitioning to a phase of intermediate density with islands, and gradual nucleation of solid phases surrounded by a disorganized liquid phase.[38-40] As the coverage of the chemisorbed state increases, the hydrocarbon chains pack to maximize van der Waals interactions and develop a lower equilibrium tilt angle (~30°).[41] Upon saturation, the hexagonal ($\sqrt{3}$ x $\sqrt{3}$) R30° lattice and the c(4 x 2) superlattice structures are formed with approximately 5 Å spacing between adsorbed sulfur atoms.[42]

The kinetics of formation for *n*-alkanethiols on gold has been examined by *in situ*[39, 43, 44] and *ex situ*[45] methods. Early studies indicated that the formation of a monolayer occurs within the first minute of growth followed by an ordering of the monolayer that occurs over a period of hours.[45, 46] Later, these ex situ studies were confirmed by in situ methods that demonstrated a single monolayer is formed very rapidly with a slower 'healing' of defects.[47] The kinetics of assembly of alkanethiolate monolayers is affected by the nature of the solvent used during the adsorption process.[48-50] Bensebaa et al.[51] reported that a long-chained alkanethiolate SAM formed from a poorer solvent (ethanol) contributed to a more crystalline SAM than that formed from a better solvent (hexane) for short adsorption times. Yan et al.[52, 53] have shown that both the overall chain density within $C_{16}S/Au$ SAMs and the solvent stability of the monolayer increases when more polar solvents are used for the assembly process: aqueous micellar

solution > ethanol > isooctane. Not only do the kinetics depend on the solvent used in the formation, but the kinetics of formation of long-chained thiols has been observed to be slower than short-chained thiolates on gold.[44, 50, 54]

The structure of a SAM is highly dependent upon the chain length of the hydrocarbon backbone and the terminal group. Alkanethiols that terminate in various functional groups ($X(CH_2)_nSH$; $X=OH$, CO_2H, NH_2, CH_3, CF_3, etc.) can be purchased or synthesized.[32] These ω-alkanethiols adsorb to present uniform chemical functionalities varying from high-energy (hydrophilic) to low-energy (hydrophobic) surfaces. The surface energies of these model surfaces can be qualitatively assessed through the use of wetting measurements, which will be explained in Chapter II. One assessment used in the determination of structural conformation of alkanethiolate SAMs includes the assignment of the alignment of the thiol on the surface, which can be done through analysis of reflectance-absorption infrared (RAIR) spectra. The alignment of the alkanethiol on the surface can be described by the angle formed with the molecular backbone of the hydrocarbon and the plane of the surface, termed the cant (α), and the twist (β) of the thiolate within the plane as seen in Figure 1.1.

For alkanethiolate SAMs on gold, the cant (or tilt) observed for a defect free structure is approximately $27°$ from the surface normal with a twist of $53°$ around its molecular axis.[55, 56] Structural order can be examined directly with methods such as atomic force microscopy (AFM) or scanning tunneling microscopy (STM), or inferred indirectly by reflectance absorption infrared spectroscopy (RAIRS), wetting measurements, and electrochemistry. Bain et al.[45] observed that methylene chain $(CH_2)_n$ lengths of n > 10 exhibit a higher degree of structural order than short-chained n-

alkanethiols due to the increased van der Waals interactions of the long-chain hydrocarbon backbones. This structural information is based upon the surface selection rules for RAIRS,[56, 57] where only components oriented normal to the surface contribute to observable modes (see Chapter II).
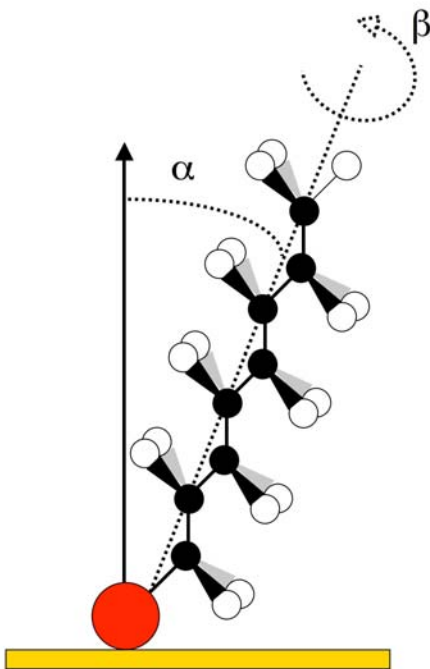
Figure 1.1. Illustration of an *n*-alkanethiolate adsorbate on a gold substrate that is canted (α) from the surface normal and twisted (β) around its molecular axis. The sulfur atom is indicated in red, the carbon atoms in black, and the hydrogen atoms in white.

For the work described in this project, we have chosen to use the assembly of ω-terminated alkanethiols on gold as a model system due to (1) the chemical and electrochemical stability of gold as an electrode, (2) the synthetic flexibility of producing various molecular compositions for assembly of a chemically diverse range of surfaces,[32] (3) the abundance of published work on this system, and (4) the potential applications of

thiol-on-gold chemistry in future devices based on molecular electronics and/or soft lithography.[58]

Proteins on SAMs

Modification of the surface chemistry of a substrate has a direct effect on the adsorption of proteins. SAMs can be used to increase both physical and chemical binding events of proteins on a substrate. Typically the control of the orientation of proteins on a surface is a difficult task and is dictated by the binding events between the amino acid residues on the periphery of the protein and the surface functionality.[18, 59] This lack of control of the orientation of the proteins can lead to nonspecific binding and loss of protein functionality. To control nonspecific binding events, SAMs with poly(ethylene glycol) terminal groups have been shown to resist the adsorption of proteins.[60, 61]

The resistance or increase of protein adsorption has been attributed to the wettability of each surface. Sigal et al.[61] demonstrated that small proteins such as RNAse A, and lysozyme were sensitive to the wettability of the surface, while larger proteins were not specifically controlled by the surface wettability. Harder et al.[62] determined that the resistance of the poly(ethylene glycol) surface to protein adsorption is a function of its interaction with water as opposed to a steric repulsion[63] effect of the polymer with the protein.

Photosynthesis

Photosynthesis is the biological process in which plants, green algae, and cyanobacteria convert solar energy into chemical energy. The biochemistry of photosynthesis can be written as[64]

$$6CO_2 + 12H_2O + 18ATP + 12NADPH \rightarrow C_6H_{12}O_6 + 18ADP + 18P_i + 12NADP^+ + 12H^+ + 6O_2 \qquad (1\text{-}2)$$
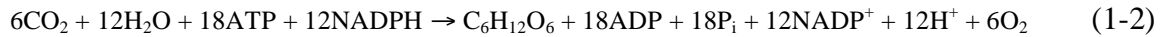
Photosynthesis occurs within the thylakoid membrane of chloroplasts. The thylakoid membrane consists of cylindrical stacks of appressed thlakoids (grana) and single-layered thylakoid membranes joining the grana regions (stroma). The thylakoid membrane includes all of the proteins necessary for photosynthesis as well as ion channels that lower the membrane potential. The thylakoid membrane has a large amount of polyunsaturated fatty acids that allow for diffusion of protein complexes. Within the thylakoid membrane, Photosystem I and ATP synthase are concentrated in the stroma region, whereas Photosystem II is concentrated in the grana region.[65] If Photosystem I and II were not separated from each other, Photosystem I would cause an imbalance in Photosystem II excitation energy.[66]

The two key protein complexes that participate in photosynthesis are known as Photosystems I and II (PSI and PSII) along with an ATP synthase that produces ATP. PSI and PSII function according to the Z-scheme[67] (Figure 1.2) by which electrons from water pass through PSII and on to PSI, which generates the strong reductant necessary for the conversion of $NADP^+$ to NADPH.[68] The two photosystems catalyze the initial and fundamental steps of oxygenic photosynthesis. They trap sunlight through extended

antenna systems, called light harvesting complexes, and use the energy to excite the primary electron donors (P700 in PSI and P680 in PSII), each releasing one electron per reaction cycle.[69] The light harvesting complexes increase the spectral range of PSI to allow more efficient photon capture.[70] The photosynthetic process is driven by visible light (wavelengths from 400 to 700 nm) that is adsorbed by pigment molecules (mainly chlorophyll a and b, and carotenoids).[71] The primary electron donors, P700 and P680, are given their names for the wavelength of light that causes maximal bleaching upon oxidation[72] such as 700 nm and 680 nm respectively.
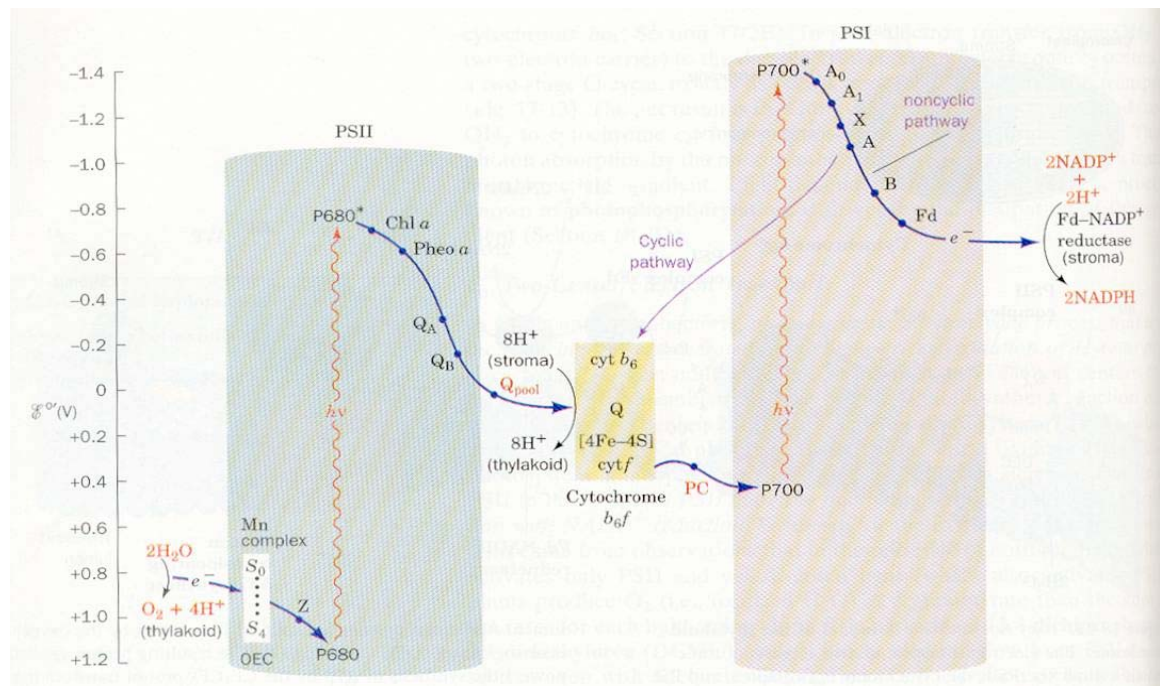
Figure 1.2. Z-scheme of the photosynthetic apparatus as taken from Voet et al.[73]

The PSI complex is a 660 kDa protein complex consisting of a 380 kDa reaction center core and a 280 kDa peripheral light harvesting apparatus, LHCI.[74] The PSI reaction center consists of up to fourteen polypeptides. They vary in molecular weight, hydrophobicity, and location with respect to the lipid bilayer. The polypeptides that make up the PSI reaction center are *PsaA*, *PsaB*, *PsaC*, *PsaD*, *PsaE*, *PsaF*, *PsaG*, *PsaH*, *PsaI*, *PsaJ*, *PsaK*, *PsaL*, *PsaN*, *PsaO*. *PsaA* and *PsaB* form the core complex while *PsaC*, *PsaD*, *PsaH*, and *PsaE* form the domain responsible for the ferredoxin-docking site. *PsaN* and *PsaF* form the plastocyanin docking site of PSI. Table 1.1 lists the polypeptide subunits of PSI and their various associated functions reported by Chitnis[75] and Jensen et al.[76] *PsaA* and *PsaB* form the two branches of cofactors responsible for electron transport called the A-branch and B-branch respectively. Upon excitation, P700* releases an electron to form P700$^+$ and the electron travels via one of the available branches. According to electron paramagnetic resonance (EPR) and Fourier transform infrared (FTIR) difference spectra, two active branches with different kinetics for electron transfer are supported.[69]

Table 1.1. Composition of PSI in higher plants as compiled from Chitnis[75] and Jensen et al.[76]

Subunit	Predicted Mass	Cofactors	Functions	Properties
PsaA and *PsaB*, PSI-A and PSI-B	83.2 (66) 82.5 (66)	85 chlorophyll *a* P700 22 β carotenes 2 phylloquinones 1 [4Fe-4S] cluster (F_X)	Light-harvesting Charge separation Photoprotection Charge stabilization Charge stabilization	11 transmembrane α-helices each
PsaC, PSI-C	8.9 (8)	2[4Fe-4S] clusters (F_A, F_B)	Terminal electron acceptor donates e^- to ferredoxin	Peripheral on stromal side
PsaD, PSI-D	17.8 (17.7)		Binding of ferredoxin Binding of PSI-C	Peripheral on stromal side
PsaE, PSI-E	10.4 (8)		Binding of ferredoxin Involved in cyclic electron transport	Peripheral on stromal side
PsaF, PSI-F	17.3 (15.8)		Binding of plastocyanin Binding of LHCI	Two transmembrane α-helices
PsaG, PSI-G	11	1-2-β-carotene	Stabilization of LHCI Regulation of PSI	Two transmembrane helices
PsaH, PSI-H	10.4	2 Chlorophyll *a*	Binding of LHCII Stabilization of PSI-D	Peripheral on the stromal side
PsaI, PSI-I	4.1 (3.4)		Stabilization of PSI-L	One transmembrane α-helix
PsaJ, PSI-J	5.0 (3.0)	3 Chlorophyll *a*	Stabilization of PSI-F	One transmembrane α-helix
PsaK, PSI-K	8.5 (5.1)	2 Chlorophyll *a*	Binding of LHCI	Two transmembrane α-helices
PsaL, PSI-L	18.0 (14.3)	3 Chlorophyll *a*	Stabilization of PSI-H and PSI-O	Two transmembrane α-helices
PsaN, PSI-N	9.7		Docking of plastocyanin	Peripheral on the lumenal side
PsaO, PSI-O	10.1	Chlorophyll *a*?	Binding of LHCII (state transitions)	
Lhca1	21.5	~ 10 Chl *a*, ~ 2 Chl *b* ~ 2 carotenoids	Light-harvesting LHCI-730	
Lhca2	23.2	~ 10 Chl *a*, ~ 2 Chl *b* ~ 2 carotenoids	Light-harvesting LHCI-680B	
Lhca3	24.9	~ 10 Chl *a*, ~ 2 Chl *b* ~ 2 carotenoids	Light-harvesting LHCI-680A	
Lhca4	22.3	~ 10 Chl *a*, ~ 2 Chl *b* ~ 2 carotenoids	Light-harvesting LHCI-730	

According to the crystal structure of cyanobacterial PSI at 2.5 Å resolution, determined by Jordan et al.,[77] cyanobacterial PSI consists of 12 subunits as shown in Figure 1.3, while higher plants have additional subunits. The structural model for cyanobacterial PSI can be found in the Protein Data Bank under the accession code of 1 JB0. The number of cofactors bound to PSI in cyanobacteria include 90 chlorophyll *a* (Chl *a*) in the antenna systems and five Chl *a*, one Chl *a'*, two phylloquinones (vitamin K_1), and three Fe_4S_4 clusters that form the electron transfer chain.[77-79] In addition, 22 carotenoids, four lipids, one putative Ca^{2+}, and 201 water molecules were identified.[69]

Recently, the crystal structure of higher plant PSI at 4.4 Å resolution was determined by Ben-Shem et al.[80, 81] such that 12 core subunits, 4 different light-harvesting membrane proteins (LHCI), 45 transmembrane helices, 167 chlorophylls, 3 Fe-S clusters and 2 phylloquinones were observed. An atomic level computational model of higher plant PSI can be found in the Protein Data Bank with the code 1YO9. The 4 different light-harvesting complexes are *Lhca1-4*, which have been shown to exist as a single copy of each with earlier discrepancies based on the presence of 'gap' and 'linker' chlorophylls bound at the interface between PSI and LHCI that are possibly removed after detergent treatment.[82, 83] Triton X-100 isolations of PSI have been shown to strip away LHCI complexes while glycosidic detergents appear to maintain the LHCI complexes.[70]

The light harvesting complexes gather light and pass the energy of adsorbed photons to the photosynthetic center. The photosynthetic center, P700, was first identified as a 'special pair' of chlorophyll *a*, but was later identified as a dimer.[84] Eventually, experiments suggested that it was a dimer of chlorophyll.[85, 86] After determination of the crystal structure of cyanobacteria, it was confirmed that P700 is a heterodimer of chlorophyll *a* and *a'* (the $C13^2$ epimer of chlorophyll *a*) that undergoes light-induced oxidation producing $P700^+$.[77] The redox potential of P700 has been reported to vary from 360 mV to 520 mV.[87] Sétif and Mathis[88] reported that the potential of P700 in spinach can be shifted negatively by 23 to 61 mV upon detergent treatment with Triton X-100 or sodium dodecyl sulfate. Nakamura et al.[89] recently reported that the redox potential of P700 of Triton X-100 treated spinach PSI is approximately 475 mV, and that Triton X-100 stripped PSI, such that only *PsaA*, *PsaB*, and one third of the antenna Chl *a* molecules are present, is lowered to 466 mV. One of their most interesting

points is that the redox potential of P700 in higher plants as compared to cyanobacteria, is

approximately 50 mV higher.
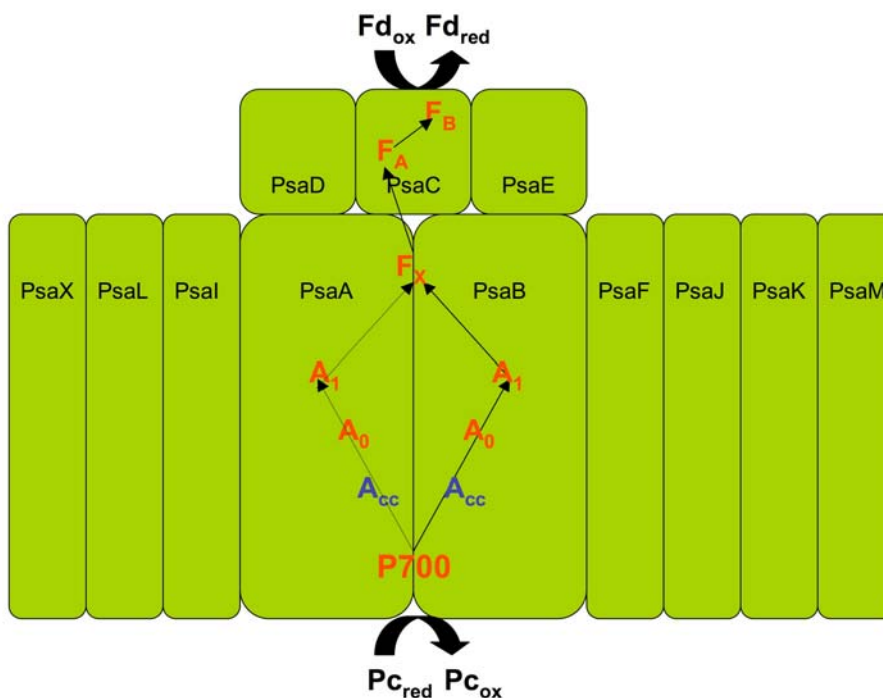
Figure 1.3. Schematic of cyanobacterial PSI subunits and electron transfer cofactors and proteins as adapted from Saenger et al.[69] Cofactors of the electron transfer chain are denoted in red with an accessory chlorophyll in blue. Plastocyanin (Pc) and ferredoxin (Fd) are the proteins involved in the donation and acceptance of electrons from PSI, respectively.

The electron lost from P700 is transferred to A_0, a monomeric Chl *a* molecule and

then to A_1, a phylloquinone (vitamin K_1).[90] Electron transfer proceeds from A_1 to a series

of membrane-bound Fe-S clusters. The first acceptor is F_X and the terminal acceptors are

F_A and F_B. In nature, PSI functions to transfer electrons from the soluble electron carrier

plastocyanin to the soluble electron carrier ferredoxin. In particular, electrons from F_A/F_B

are donated to soluble ferredoxin which in turn shuttles them to ferredoxin:NADP$^+$

14

reductase to catalyze the reduction of $NADP^+$.[91] The PSI reductants are the strongest

produced in any biological system and pose significant problems in terms of protection

against adverse reactions with oxygen. The midpoint potential values of several electron

carriers are summarized in Table 1.2.[68]

Table 1.2. Electron carriers and their midpoint potentials versus a normal hydrogen electrode.[68]

Electron Carrier	E_m (mV)
P700	+500
A_0	-1000
A_1	-800
F_X	-730
F_A	-590
F_B	-530

Photoelectrochemical Device Based on PSI

The integration of PSI with other materials, such as in photoelectrochemical

devices, requires controlling PSI adsorption, orienting its electron transfer vector,

ensuring stability under various conditions, and facilitating electron transfer to and

through PSI on a surface. There has been an increasing interest in the development of

devices based on PSI particularly because of the attractive quantum efficiency of almost

1,[72] the nanometer size dimension,[77, 92] and the low cost and renewability. In the area of

biologically inspired devices, Choi et al.[93] examined the adsorption of bacteriorhodopsin,

a purple membrane photosynthetic protein, on a poly-$_L$-lysine modified SAM on Au that

exhibited a photocurrent of 10 nA/cm^2 at an optimum solution pH of 8.0. Crittenden et

al.[94] observed that an optimal photovoltage occurred at a relative humidity of 15% with

bacteriorhodopsin on an indium tin oxide substrate. Lu et al.[95] utilized bacteriorhodopsin

15

entrapped mesoporous WO_3-TiO_2 films to achieve a photocurrent of 30 $\mu A/cm^2$. Recently, Das et al.[96] have prepared a solid-state electronic device by sandwiching bacterial reaction centers or spinach-extracted PSI between monolayer-coated gold and an organic semiconductor. Frolov et al.[97] modified cysteine residues in cyanobacterial Photosystem I to obtain immobilization on a gold surface utilizing the same Au-S bond obtained by SAMs. Using the same methods as Frolov et al.[97] for measurement of electrostatic potentials above photosynthetic reaction centers with Kelvin probe force microscopy, Lee et al.[92] demonstrated photo-induced voltages on top of physisorbed PSI substrates. Rusling, Frank, and co-workers[98] have investigated electron transfer to a bacterial photosynthetic redox center, adsorbed onto positively charged polymers atop a thin, negatively charged SAM on gold. They observed more rapid electron transfer in this case than for that measured between the redox center and a bare gold surface, suggesting a strong orientational influence on the electron transfer rate. This team has also demonstrated reversible electron transfer between electrodes and spinach PSI contained in thick, micron-scale lipid films to identify specific electroactive cofactors of PSI.[99] In contrast, Brudvig[100] had very limited success using conventional physisorbed, aminothiol-promoter methods to observe direct PSI electrochemistry. Collectively, these results demonstrate the ability for extracting PSI from the plant, interfacing it with both organic and inorganic materials, and measuring its photo-induced, vectorial electron transfer properties.

The project described herein will address preliminary steps in the integration of PSI with advanced materials. Our approach involves the fundamental investigation and optimization of each required step for PSI integration. We have investigated the behavior

of PSI at model surfaces prepared by self-assembly of alkanethiols on gold. Based on the results of Lee et al.,[101] PSI adsorbs onto hydroxyl-terminated monolayers with the electron transfer vector oriented generally (~70%) upwards and normal to the surface. This is crucial for the successful integration of PSI on a conductive surface, since the acceptor end would be required to interact with the conductive surface while the donor end would need to be free to release electrons from the top of PSI either to conducting elements for a hard-wired device or to solution-phase redox species for a photoelectrochemical cell. To complete the circuit for a device, the donor end of PSI can be platinized[102] and interfaced with a conducting polymer as shown in Figure 1.4.
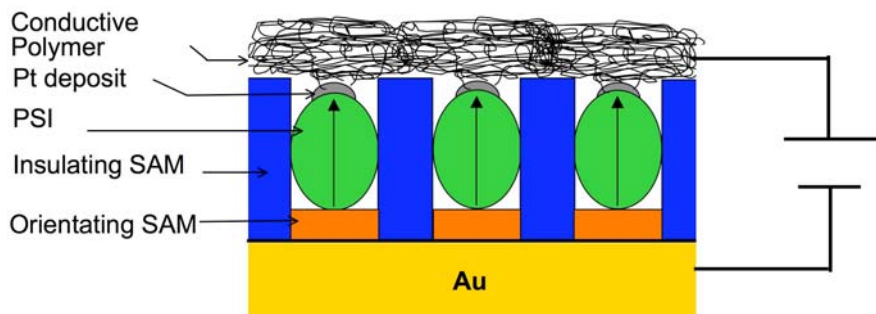
Figure 1.4. Schematic of a prototype of a photoelectrochemical device based on PSI.

Previous Work Done at Vanderbilt

Earlier work from the Jennings and Cliffel groups at Vanderbilt proved to demonstrate that the adsorption of PSI on a surface can be controlled by the chemical functionality presented at the surface. PSI adsorbs onto high-energy surfaces such as hydroxyl- and carboxylic acid-terminated surfaces, and is repelled from low-energy

surfaces such a methyl- and perfluoromethyl-terminated surfaces.[103] This result, which is opposite to that normally seen with most proteins and surfaces, is a product of the interaction of the nonionic surfactant, Triton X-100, used to stabilize the protein in an aqueous solution. On a low-energy surface, the nonionic surfactant forms a dense bilayer of polyethylene oxide groups that repel the adsorption of PSI while on a hydroxyl-terminated surface the nonionic surfactant forms sparse micelles allowing available surface sites for adsorption. Not only does PSI adsorb to a high-energy surface as opposed to a low-energy surface, a maximum adsorption occurs on an intermediate surface energy produced through the use of mixed self-assembled monolayers on gold.

Focus of Dissertation

For this dissertation we have focused on the preliminary steps in the fabrication of a prototypical photoelectrochemical device based on PSI as shown in Figure 1.4. The goals of this work includes:

(1)   Direct the adsorption of PSI on the surface.

We have utilized the adsorption properties of PSI on various surface functionalities to direct the adsorption of PSI on the surface through the use of microcontact printing of SAMs on gold.

(2)   Demonstrate the direct electrochemistry of PSI immobilized on a gold surface with both light and dark reaction events.

(3)   Entrap immobilized PSI on a substrate for the potential aspect of reducing background current and electron recombination effects between adjacent PSI complexes.

(a)   Backfill the inter-protein spaces by place exchange of the orienting

SAM with a longer methyl-terminated SAM.

(b)   Vary the spacing of the orienting SAM to enhance the place

exchange of the orienting SAM with a longer methyl-terminated

SAM.

References

1.   Axelrod, N., Volume Photoelectric Effect in Metals. *Journal of the Optical Society of America* **1966,** 56, (2), 203.

2.   Becquerel, E., *Comptes Rendus* **1839,** 9, 561.

3.   Smalley, R. E., Future Global Energy Prosperity: The Terawatt Challenge. *Materials Research Society Bulletin* **2005,** 30, (4), 412-417.

4.   Hoffert, M. I.; Caldeira, K.; Benford, G.; Criswell, D. R.; Green, C.; Herzog, H.; Jain, A. K.; Kheshgi, H. S.; Lackner, K. S.; Lewis, J. S.; Lightfoot, H. D.; Manheimer, W.; Mankins, J. C.; Mauel, M. E.; Perkins, J.; Schlesinger, M. E.; Volk, T.; Wigley, T. M. L., Advanced Technology Paths to Global Climate Stability: Energy for a Greenhouse Planet. *Science* **2002,** 298, (5595), 981-987.

5.   Lewis, N. S.; Crabtree, G. *Basic Research Needs for Solar Energy Utilization*; April 18-21, 2005, 2005; pp 1-276.

6.   Hoffert, M. I.; Caldeira, K.; Jain, A. K.; Haites, E. F.; Danny Harvey, L. D.; Potter, S. D.; Schlesinger, M. E.; Schneider, S. H.; Watts, R. G.; Wigley, T. M. L.; Wuebbles, D. J., Energy Implications of Future Stabilization of Atmospheric CO_2 Content. *Nature* **1998,** 395, (6705), 881-884.

7.   Rignot, E.; Kanagaratnam, P., Changes in the Velocity Structure of the Greenland Ice Sheet. *Science* **2006,** 311, (5763), 986-990.

8.   *Annual Energy Review 2004*; Department of Energy: Energy Information Administration: August 2005, 2005; pp 1-435.

9.   Chapin, D.; Fuller, C.; Pearson, G., A New Silicon p-n Junction Photocell for Converting Solar Radiation into Electrical Power. *Journal of Applied Physics* **1954,** 25, 676.

10.   Shaheen, S. E.; Ginley, D. S.; Jabbour, G. E., Organic-Based Photovoltaics: Toward Low-Cost Power Generation. *Materials Research Society Bulletin* **2005,** 30, (1), 10-19.

11.   Gratzel, M., Dye-Sensitized Solar Cells. *Journal of Photochemistry and Photobiology C: Photochemistry Reviews* **2003,** 4, (2), 145-153.

12.   Rand, B.; Xue, J.; Uchida, S.; Forrest, S., Mixed Donor-Acceptor Molecular Heterojunctions for Photovoltaic Applications. I. Material Properties. *Journal of Applied Physics* **2005,** 98, (12), 124902.

13.   Kattamis, A.; Holmes, R.; Cheng, I.; Long, K.; Sturm, J.; Forrest, S.; Wagner, S., High Mobility Nanocrystalline Silicon Transistors on Clear Plastic Substrates. *IEEE Electron Device Letters* **2006,** 27, (1), 49-51.

14.   Xue, J.; Rand, B.; Uchida, S.; Forrest, S., Mixed Donor-Acceptor Molecular Heterojunctions for Photovoltaic Applications. II. Device Performance. *Journal of Applied Physics* **2005,** 98, (12), 124903.

15.   Coakley, K.; Liu, Y.; Goh, C.; McGehee, M., Ordered Organic-Inorganic Bulk Heterojunction Photovoltaic Cells. *Materials Research Society Bulletin* **2005,** 30, (1), 37-40.

16.   Milliron, D.; Gur, I.; Alivisatos, A., Hybrid Organic- Nanocrystal Solar Cells. *Materials Research Society Bulletin* **2005,** 30, (1), 41-44.

17.   Chen, J.; Officer, D.; Pringle, J.; MacFarlane, D.; Too, C.; Wallace, G., Photoelectrochemical Solar Cells Based on Polyterthiophenes Containing Porphyrins Using Ionic Liquid Electrolyte. *Electrochemical and Solid State Letters* **2005,** 8, (10), A528-A530.

18.   Rao, S. V.; Anderson, K. W.; Bachas, L. G., Oriented Immobilization of Proteins. *Mikrochimica Acta* **1998,** 128, 127-143.

19.   Prime, K. L.; Whitesides, G. M., Self-Assembled Organic Monolayers: Model Systems for Studying Adsorption of Proteins at Surfaces. *Science* **1991,** 252, (5009), 1164-1167.

20.   Martins, M. C. L.; Ratner, B. D.; Barbosa, M. A., Protein Adsorption on Mixtures of Hydroxyl- and Methyl-Terminated Alkanethiols Self-Assembled Monolayers. *Journal of Biomedical Materials Research Part A* **2003,** 67A, (1), 158-171.

21.   Mrksich, M., What Can Surface Chemistry Do For Cell Biology? *Current Opinion in Chemical Biology* **2002,** 6, (6), 794-797.

22.   Mrksich, M.; Chen, C. S.; Xia, Y.; Dike, L. E.; Ingber, D. E.; Whitesides, G. M., Controlling Cell Attachment on Contoured Surfaces with Self-Assembled Monolayers of Alkanethiolates on Gold. *Proceedings of the National Academy of Sciences of the United States of America* **1996,** 93, (20), 10775-10778.

23.   Mrksich, M.; Whitesides, G. M., Using Self-Assembled Monolayers to Understand the Interactions of Man-Made Surfaces with Proteins and Cells. *Annual Review of Biophysics and Biomolecular Structure* **1996,** 25, 55-78.

24.   Patel, N.; Davies, M. C.; Hartshorne, M.; Heaton, R. J.; Roberts, C. J.; Tendler, S. J. B.; Williams, P. M., Immobilization of Protein Molecules onto Homogeneous and Mixed Carboxylate-Terminated Self-Assembled Monolayers. *Langmuir* **1997,** 13, 6485-6490.

25.   Ratner, B. D.; Bryant, S. J., Biomaterials: Where We Have Been and Where We Are Going. *Annual Review of Biomedical Engineering* **2004,** 6, 41-75.

26.   Sethuraman, A.; Belfort, G., Protein Structural Perturbation and Aggregation on Homogeneous Surfaces. *Biophysical Journal* **2005,** 88, 1322-1333.

27.   Tegoulia, V. A.; Rao, W. S.; Kalambur, A. T.; Rabolt, J. R.; Cooper, S. L., Surface Properties, Fibrinogen Adsorption, and Cellular Interactions of a Novel Phosphorylcholine-Containing Self-Assembled Monolayer on Gold. *Langmuir* **2001,** 17, (14), 4396-4404.

28.   Langmuir, I., Mechanical Properties of Monomolecular Films. *Journal of the Franklin Institute* **1934,** 218, (2), 143-171.

29.   Blodgett, K. B., Films Built by Depositing Successive Monomolecular Layers on a Solid Surface. *Journal of the American Chemical Society* **1935,** 57, (6), 1007-1002.

30.   Bain, C. D.; Whitesides, G. M., Modeling Organic-Surfaces with Self-Assembled Monolayers. *Angewandte Chemie-International Edition in English* **1989,** 28, (4), 506-512.

31.   Nuzzo, R. G.; Allara, D. L., Adsorption of Bifunctional Organic Disulfides on Gold Surfaces. *Journal of the American Chemical Society* **1983,** 105, (13), 4481-4483.

32.   Laibinis, P. E.; Palmer, B. J.; Lee, S.-W.; Jennings, G. K., The Synthesis of Organothiols and Their Assembly into Monolayers on Gold. In *Thin Films*, Ulman, A.; Powell, R.; Francombe, M. H., Eds. Academic Press: 1998; Vol. 24, pp 1-41.

33.   Ulman, A., *Characterization of Organic Thin Films*. Manning Publications Co.: 1994; p 276.

34.   Wasserman, S. R.; Tao, Y. T.; Whitesides, G. M., Structure and Reactivity of Alkylsiloxane Monolayers Formed by Reaction of Alkyltrichlorosilanes on Silicon Substrates. *Langmuir* **1989,** 5, (4), 1074-1087.

35.   Wasserman, S. R.; Whitesides, G. M.; Tidswell, I. M.; Ocko, B. M.; Pershan, P. S.; Axe, J. D., The Structure of Self-Assembled Monolayers of Alkylsiloxanes on Silicon: A Comparison of Results from Ellipsometry and Low-Angle X-Ray Reflectivity. *Journal of the American Chemical Society* **1989,** 111, (15), 5852-5861.

36.   Tillman, N.; Ulman, A.; Penner, T. L., Formation of Multilayers by Self-Assembly. *Langmuir* **1989,** 5, (1), 101-111.

37.   Schreiber, F., Structure and Growth of Self-Assembling Monolayers. *Progress in Surface Science* **2000,** 65, (5-8), 151-256.

38.   Schwartz, D. K., Mechanisms and Kinetics of Self-Assembled Monolayer Formation. *Annual Review of Physical Chemistry* **2001,** 52, 107-137.

39.   Yamada, R.; Uosaki, K., *In Situ*, Real Time Monitoring of the Self-Assembly Process of Decanethiol on Au(111) in Liquid Phase. A Scanning Tunneling Microscopy Investigation. *Langmuir* **1997,** 13, (20), 5218-5221.

40.   Yamada, R.; Uosaki, K., In Situ Scanning Tunneling Microscopy Observation of the Self-Assembly Process of Alkanethiols on Gold(111) in Solution. *Langmuir* **1998,** 14, (4), 855-861.

41.   Laibinis, P. E.; Bain, C. D.; Nuzzo, R. G.; Whitesides, G. M., Structure and Wetting Properties of ω-Alkoxy-n-alkanethiolate Monolayers on Gold and Silver. *Journal of Physical Chemistry* **1995,** 99, 7663-7676.

42.   Yourdshahyan, Y.; Rappe, A. M., Structure and Energetics of Alkanethiol Adsorption on the Au(111) Surface. *Journal of Chemical Physics* **2002,** 117, (2), 825-833.

43.   Peterlinz, K. A.; Georgiadis, R., In Situ Kinetics of Self-Assembly by Surface Plasmon Resonance Spectroscopy. *Langmuir* **1996,** 12, 4731-4740.

44.   Xu, S.; Cruchon-Dupeyrat, S. J. N.; Garno, J. C.; Liu, G. Y.; Jennings, G. K.; Yong, T. H.; Laibinis, P. E., In Situ Studies of Thiol Self-Assembly on Gold from Solution Using Atomic Force Microscopy. *Journal of Chemical Physics* **1998,** 108, (12), 5002-5012.

45.   Bain, C. D.; Troughton, E. B.; Tao, Y. T.; Evall, J.; Whitesides, G. M.; Nuzzo, R. G., Formation of Monolayer Films by the Spontaneous Assembly of Organic Thiols from Solution onto Gold. *Journal of the American Chemical Society* **1989,** 111, (1), 321-335.

46.   Hahner, G.; Woll, C.; Buck, M.; Grunze, M., Investigation of Intermediate Steps in the Self-Assembly of *n*-Alkanethiols on Gold Surfaces by Soft X-Ray Spectroscopy. *Langmuir* **1993,** 9, (8), 1955-1958.

47.   Shimazu, K.; Yagi, I.; Sato, Y.; Uosaki, K., In Situ and Dynamic Monitoring of the Self-Assembling and Redox Processes of a Ferrocenylundecanethiol Monolayer by Electrochemical Quartz Crystal Microbalance. *Langmuir* **1992,** 8, (5), 1385-1387.

48.   Kim, Y. T.; McCarley, R. L.; Bard, A. J., Observation of n-Octadeanethiol Multilayer Formation from Solution onto Gold. *Langmuir* **1993,** 9, (8), 1941-1944.

49.   Schneider, T. W.; Buttry, D. A., Electrochemical Quartz Crystal Microbalance Studies of Adsorption and Desorption of Self-Assembled Monolayers of Alkyl Thiols on Gold. *Journal of the American Chemical Society* **1993,** 115, (26), 12391-12397.

50.   Dannenberger, O.; Buck, M.; Grunze, M., Self-Assembly of n-Alkanethiols: A Kinetic Study by Second Harmonic Generation. *Journal of Physical Chemistry B* **1999,** 103, 2202-2213.

51.   Bensebaa, F.; Voicu, R.; Huron, L.; Ellis, T. H., Kinetics of Formation of Long-Chain *n*-Alkanethiolate Monolayers on Polycrystalline Gold. *Langmuir* **1997,** 13, (20), 5335-5340.

52.   Yan, D.; Jordan, J. L.; Burapatana, V.; Jennings, G. K., Formation of n-Alkanethiolate Self-Assembled Monolayers onto Gold in Aqueous Micellar Solutions of n-Alkyltrimethylammonium Bromides. *Langmuir* **2003,** 19, (8), 3357-3364.

53.   Yan, D.; Saunders, J. A.; Jennings, G. K., Formation and Stability of Hexadecanethiolate SAMs Prepared in Aqueous Micellar Solutions of C12E6. *Langmuir* **2003,** 19, (22), 9290-9296.

54.   DeBono, R. F.; Loucks, G. D.; Dellamanna, D.; Krull, U. J., *Canadian Journal of Chemistry* **1996,** 74, 677-688.

55.   Laibinis, P. E.; Whitesides, G. M.; Allara, D. L.; Tao, Y. T.; Parikh, A. N.; Nuzzo, R. G., Comparison of the Structures and Wetting Properties of Self-Assembled Monolayers of *n*-Alkanethiols on the Coinage Metal-Surfaces, Cu, Ag, Au. *Journal of the American Chemical Society* **1991,** 113, (19), 7152-7167.

56.   Parikh, A. N.; Allara, D. L., Quantitative-Determination of Molecular-Structure in Multilayered Thin-Films of Biaxial and Lower Symmetry from Photon Spectroscopies. 1. Reflection Infrared Vibrational Spectroscopy. *Journal of Chemical Physics* **1992,** 96, (2), 927-945.

57.   Greenler, R. G., Infrared Study of Adsorbed Molecules on Metal Surfaces by Reflection Techniques. *The Journal of Chemical Physics* **1966,** 44, (1), 310-314.

58.   Tien, J.; Xia, Y.; Whitesides, G. M., *Microcontact Printing of SAMs*. Academic: Boston, 1998; Vol. 24, p 227-254.

59.   Whitesides, G. M.; Mathias, J. P.; Seto, C. T., Molecular Self-Assembly and Nanochemistry: A Chemical Strategy for the Synthesis of Nanostructures. *Science* **1991,** 254, 1312-1319.

60. Pale-Grosdemange, C.; Simon, E.; Prime, K. L.; Whitesides, G. M., Formation of Self-Assembled Monolayers by Chemisorption of Derivatives of Oligo(ethylene glycol) of Structure $HS(CH_2)_{11}(OCH_2CH_2)_mOH$ on Gold. *Journal of the American Chemical Society* **1991,** 113, (1), 12-20.

61. Sigal, G.; Mrksich, M.; Whitesides, G. M., Effect of Surface Wettability on the Adsorption of Proteins and Detergents. *Journal of the American Chemical Society* **1998,** 120, (14), 3464-3473.

62. Harder, P.; Grunze, M.; Dahint, R.; Whitesides, G. M.; Laibinis, P. E., Molecular Conformation in Oligo(Ethylene Glycol)-Terminated Self-Assembled Monolayers on Gold and Silver Surfaces Determines Their Ability to Resist Protein Adsorption. *Journal of Physical Chemistry B* **1998,** 102, 426-436.

63. Jeon, S. I.; Lee, J. H.; Andrade, J. D.; deGennes, P. G., Protein-Surface Interactions in the Presence of Polyethylene Oxide: I. Simplified Theory. *Journal of Colloid and Interface Science* **1991,** 142, (1), 149-158.

64. Ke, B., *Advances in Photosynthesis*. Kluwer Academic Publishers: Norwell, MA, 2001; Vol. 10, p 737.

65. Anderson, J. M., Changing Concepts About the Distribution of Photosystems I and II Between Grana-Appressed and Stroma-Exposed Thylakoid Membranes. *Photosynthesis Research* **2002,** 73, 157-164.

66. Nalwa, H. S., *Supramolecular Photosensitive and Electroactive Materials*. Academic Press: 2001.

67. Hill, R.; Bendall, F., Function of Two Cytochrome Components in Chloroplast: A Working Hypothesis. *Nature* **1960,** 186, 136-137.

68. Raghavendra, A. S., *Photosynthesis: A Comprehensive Treatise*. Cambridge University Press: 1998.

69. Saenger, W.; Jordan, P.; Krauss, N., The Assembly of Protein Subunits and Cofactors in Photosystem. *Current Opinion in Structural Biology* **2002,** 12, (2), 244-254.

70. Horspool, W. M.; Song, P.-S., *CRC Handbook of Organic Photochemistry and Photobiology*. CRC Press, Inc.: 1994.

71. Singhal, G. S.; Renger, G.; Sopory, S. K.; Irrgang, K.-D.; Govindjee, *Concepts in Photobiology*. Kluwer Academic Publishers: 1999.

72. Brettel, K., Electron Transfer and Arrangement of the Redox Cofactors in Photosystem I. *Biochimica Et Biophysica Acta* **1997,** 1318, 322-373.

73. Voet, D.; Voet, J.; Pratt, C., *Fundamentals of Biochemistry*. 1st ed.; John Wiley & Sons Inc.: 1999; p 1018.

74. Nelson, N.; Ben-Shem, A., Photosystem I Reaction Center: Past and Future. *Photosynthesis Research* **2002,** 73, 193-206.

75. Chitnis, P. R., Photosystem I: Function and Physiology. *Annual Review of Plant Physiology and Plant Molecular Biology* **2001,** 52, 593-596.

76. Jensen, P. E.; Haldrup, A.; Rosgaard, L.; Scheller, H. V., Molecular Dissection of Photosystem I in Higher Plants: Topology, Structure and Function. *Physiologia Plantarum* **2003,** 119, 313-321.

77. Jordan, P.; Fromme, P.; Witt, H. T.; Klukas, O.; Saenger, W.; Krauss, N., Three-Dimensional Structure of Cyanobacterial Photosystem I at 2.5 Angstrom Resolution. *Nature* **2001,** 411, (6840), 909-917.

78. Jolley, C.; Ben-Shem, A.; Nelson, N.; Fromme, P., Structure of Plant Photosystem I Revealed by Theoretical Modeling. *The Journal of Biological Chemistry* **2005,** 280, (39), 33627-33636.

79. Grotjohann, I.; Fromme, P., Structure of Cyanobacterial Photosystem I. *Photosynthesis Research* **2005,** 85, 51-72.

80. Ben-Shem, A.; Frolow, F.; Nelson, N., Crystal Structure of Plant Photosystem I. *Nature* **2003,** 426, (December 11, 2003), 630-635.

81.   Ben-Shem, A.; Nelson, N.; Frolow, F., Crystallization and Initial X-ray Diffraction Studies of Higher Plant Photosystem I. *Acta Crystallographica Section D* **2003,** D59, 1824-1827.

82.   Ballottari, M.; Govoni, C.; Caffarri, S.; Morosinotto, T., Stoichiometry of LHCI Antenna Polypeptides and Characterization of Gap and Linker Pigments in Higher Plants Photosystem I. *European Journal of Biochemistry* **2004,** 271, 4659-4665.

83.   Klimmek, F.; Ganeteg, U.; Ihalainen, J. A.; Roon, H. v.; Jensen, P. E.; Scheller, H. V.; Dekker, J. P.; Jansson, S., Structure of the Higher Plant Light Harvesting Complex I: In Vivo Characterization and Structural Interdependence of the Lhca Proteins. *Biochemistry* **2005,** 44, 3065-3073.

84.   Norris, J. R.; Uphaus, R. A.; Crespi, H. L.; Katz, J. J., Electron Spin Resonance of Chlorophyll and the Origin of Signal I in Photosynthesis. *Proceedings of the National Academy of Sciences* **1971,** 68, (3), 625-628.

85.   Maeda, H.; Watanabe, T.; Kobayashi, M.; Ikegami, I., Presence of 2 Chlorophyll a' Molecules at the Core of Photosystem I. *Biochimica Et Biophysica Acta* **1992,** 1099, 74-80.

86.   Davis, I. H.; Heathcote, P.; Maclachlan, D. J.; Evans, M. C. W., Modulation Analysis of the Electron Spin Echo Signals of *In Vivo* Oxidized Primary Donor N-14 Chlorophyll Centers in Bacterial, P870 and P960, and Plant Photosystem-I, P700, Reaction Centers. *Biochimica Et Biophysica Acta* **1993,** 1143, 183-189.

87.   Golbeck, J. H., Structure, Function and Organization of the Photosystem-I Reaction Center Complex. *Biochimica Et Biophysica Acta* **1987,** 895, (3), 167-204.

88.   Setif, P.; Mathis, P., The Oxidation-Reduction Potential of P-700 in Chloroplast Lamellae and Subchloroplast Particles. *Archives of Biochemistry and Biophysics* **1980,** 204, (477-485).

89.   Nakamura, A.; Suzawa, T.; Kato, Y.; Watanabe, T., Significant Species-Dependence of P700 Redox Potential as Verified by Spectroelectrochemistry: Comparison of Spinach and *Thermosynechococcus elongatus*. *FEBS Letters* **2005,** 579, 2273-2276.

90.   Golbeck, J. H., The Binding of Cofactors to Photosystem I Analyzed by Spectroscopic and Mutagenic Methods. *Annual Review of Biophysics and Biomolecular Structure* **2003,** 32, 237-256.

91.   Munge, B.; Das, S. K.; Ilagan, R.; Pendon, Z.; Yang, J.; Frank, H. A.; Rusling, J. F., Electron Transfer Reactions of Redox Cofactors in Spinach Photosystem I Reaction Center Protein in Lipid Films on Electrodes. *Journal of the American Chemical Society* **2003,** 125, 12457-12463.

92.   Lee, I.; Lee, J.; Stubna, A.; Greenbaum, E., Measurement of Electrostatic Potentials above Oriented Single Photosynthetic Reaction Centers. *Journal of Physical Chemistry B* **2000,** 104, 2439-2443.

93.   Choi, H. G.; Min, J. H.; Lee, W. H.; Choi, J. W., Adsorption Behavior and Photoelectric Response Characteristics of Bacteriorhodopsin Thin Films Fabricated by Self-Assembly Technique. *Colloids and Surfaces B-Biointerfaces* **2002,** 23, (4), 327-337.

94.   Crittenden, S.; Howell, S.; Reifenberger, R.; Hillebrecht, J.; Birge, R. R., Humidity-Dependent Open-Circuit Photovoltage From a Bacteriorhodopsin/Indium Tin Oxide Bioelectronic Heterostructure. *Nanotechnology* **2003,** 14, 562-565.

95.   Lu, Y.; Yuan, M.; Liu, Y.; Tu, B.; Xu, C.; Liu, B.; Zhao, D.; Kong, J., Photoelectric Performance of Bacteria Photosynthetic Proteins Entrapped on Tailored Mesoporous WO_3-TiO_2 Films. *Langmuir* **2005,** 21, 4071-4076.

96.   Das, R.; Kiley, P. J.; Segal, M.; Norville, J.; Yu, A. A.; Wang, L.; Trammell, S. A.; Reddick, L. E.; Kumar, R.; Stellacci, F.; Lebedev, N.; Schnur, J.; Bruce, B. D.; Zhang, S.; Baldo, M., Integration of Photosynthetic Protein Molecular Complexes in Solid-State Electronic Devices. *Nano Letters* **2004,** 4, (6), 1079-1083.

97.   Frolov, L.; Rosenwaks, Y.; Carmeli, C.; Carmeli, I., Fabrication of a Photoelectronic Device by Direct Chemical Binding of the Photosynthetic Reaction Center Protein to Metal Surfaces. *Advanced Materials* **2005,** 17, (20), 2434-2437.

98.   Kong, J.; Lu, Z.; Lvov, Y. M.; Desamero, R. Z. B.; Frank, H. A.; Rusling, J. F., Direct Electrochemistry of Cofactor Redox Sites in a Bacterial Photosynthetic Reaction Center Protein. *Journal of American Chemical Society* **1998,** 120, (29), 7371-7372.

99.   Munge, B.; Das, S. K.; Ilagan, R.; Pendon, Z.; Yang, J.; Frank, H. A.; Rusling, J. F., Electron Transfer Reactions of Redox Cofactors in Spinach Photosystem I Reaction Center Protein in Lipid Films on Electrodes. *Journal of American Chemical Society* **2003,** 125, (41), 12457-12463.

100.   Kievit, O.; Brudvig, G. W., Direct Electrochemistry of Photosystem I. *Journal of Electroanalytical Chemistry* **2001,** 497, (1-2), 139-149.

101.   Lee, I.; Lee, J.; Greenbaum, E., Biomolecular Electronics: Vectorial Arrays of Photosynthetic Reaction Centers. In *Physical Review Letters*, 1997; Vol. 79, pp 3294-3297.

102.   Lee, J. W.; Lee, I.; Laible, P. D.; Owens, T. G.; Greenbaum, E., Chemical Platinization and its Effect on Excitation Transfer Dynamics and P700 Photooxidation Kinetics in Isolated Photosystem I. *Biophysical Journal* **1995,** 69, 652-659.

103.   Ko, B. S.; Babcock, B.; Jennings, G. K.; Tilden, S. G.; Peterson, R. R.; Cliffel, D.; Greenbaum, E., Effect of Surface Composition on the Adsorption of Photosystem I onto Alkanethiolate Self-Assembled Monolayers on Gold. *Langmuir* **2004,** 20, (10), 4033-4038.

CHAPTER II

EXPERIMENTAL PROCEDURES AND CHARACTERIZATION METHODS

Experimental Procedures

Materials

Na$_4$P$_2$O$_7$ · H$_2$O, MgCl$_2$ · 6H$_2$O, NaH$_2$PO$_4$ · H$_2$O, HCl, MnCl$_2$ · 4H$_2$O, NaCl, KCl, 30% H$_2$O$_2$, N, N- dimethyl formamide, acetone, 2-butanol, isooctane, dichloromethane (CH$_2$Cl$_2$, 99.9%), K$_4$Fe(CN)$_6$ · 3H$_2$O (used in Chapters III and VI), K$_3$Fe(CN)$_6$ (used in Chapters III and VI) and Na$_2$SO$_4$ (anhydrous) were purchased from Fisher Scientific. 6-mercapto-1-hexanol (HSC$_6$OH), and 4-mercapto-1-butanol (HSC$_4$OH), and pentaethylene monododecyl glycol ether (C$_{12}$E$_5$) were purchased from Fluka. KPF$_6$, 11-mercapto-1-undecanol (HSC$_{11}$OH) (97%), 8-bromo-1-octanol, 3-mercaptopropionic acid (HSC$_2$COOH), EDTA, KHCO$_3$ (98%), Br$_2$ (99%), KOH (85%), K$_3$Fe(CN)$_6$ (99%), and K$_4$Fe(CN)$_6$ · 3H$_2$O (99%), pyridine (99+%), and pentadecafluorooctanoyl chloride (C$_7$F$_{15}$COCl, 97%) were used as received from Aldrich. 1-Docosanethiol (C$_{22}$SH) was purchased from Narchem. Sorbitol, ascorbic acid, 1-dodecanethiol (HSC$_{11}$CH$_3$), 2-mercaptoethanol (HSC$_2$OH), 1-hexanethiol (HSC$_5$CH$_3$), 2-aminoethanethiol hydrochloride (HSC$_2$NH$_2$), methyl viologen dichloride hydrate (MVCl$_2$ or MV^{2+}), thiourea, Triton X-100, HEPES, Tricine, tris(hydroxymethyl)aminomethane DNase, RNase, Protease free (TRIS), and hexammineruthenium(III) chloride were purchased from Acros. Sodium ascorbate, Na$_2$HPO$_4$ · 7H$_2$O, N-(2-mercaptopropionyl)-glycine

31

(HSCH(CH$_3$)CONHCH$_2$COOH, tiopronin), and DL-dithiothreitol were purchased from Sigma. H$_2$SO$_4$ and NaOH were purchased from EM Science. Ethanol (absolute proof) was purchased from AAPER. Hexane (99.9%) and tetrahydrofuran (THF, 99.9%) were used as received from Burdlick & Jackson. Hydroxylapatite fast-flow was purchased from Calbiochem. Ferrocenylmethyltrimethylammonium iodide was purchased from Strem Chemicals. Conductive silver epoxy was purchased from Epoxy Technology. White Sealant Hysol Epoxi-Patch was purchased from Dexter Corporation. Sylgard 184 silicone elastomer base and curing agent were purchased from Dow Corning Corporation. Nitrogen was purchased from A-L Compressed Gases and Gibbs Welding Supply. Deionized water (16.7 MΩ · cm) was purified with a Modu-Pure system and used for rinsing of substrates in Chapters IV and V. ASTM Type I (18 MΩ) analytical grade deionized water (DW) was obtained with a Solution 2000 Water Purification System from Solution Consultants and used for experiments in Chapters III and VI. C$_{18}$OC$_{19}$SH was available from prior studies.[1, 2] Bis (11-hydroxyundecyl) disulfide was available from earlier studies.[3] Ferrocenylmethyltrimethylammonium hexafluorophosphate (FcTMA) was prepared according to the method of Mirkin and co-worker.[4] Gold shot (99.99%) and chromium-coated tungsten filaments were purchased from J&J Materials and R. D. Mathis, respectively. Silicon (100) wafers, p-doped with boron, were purchased from Montco Silicon. Gold interdigitated arrays (Au IDAs) with 10 μm Au lines separated by 10 μm glass lines were obtained from Abtech Scientific, Inc. 0.2 μm syringe filters from Fisher were used to filter solutions in Chapters III and VI.

Synthesis of 8-mercapto-1-octanol (HSC₈OH)

8-Mercapto-1-octanol (HSC$_8$OH) was synthesized according to the method of Iglesias et al.[5] 8-Mercapto-1-octanol was prepared through the reaction of ω-bromo-1-octanol with thiourea followed by hydrolysis as shown in Figure 2.1.
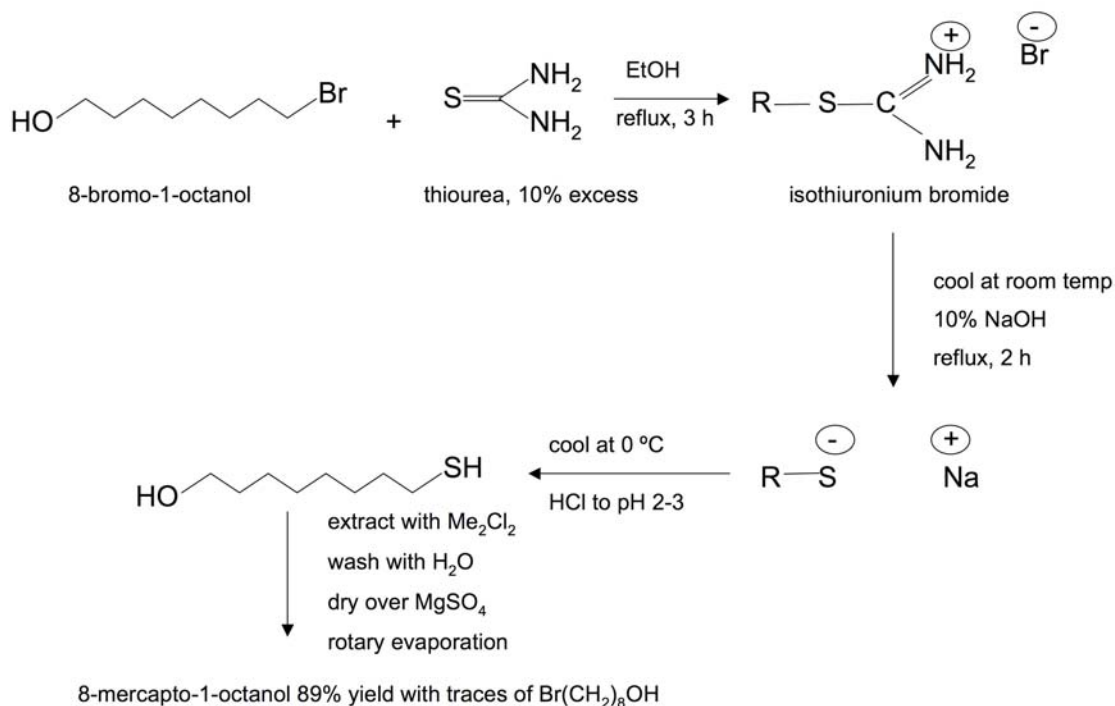
Figure 2.1. Synthesis scheme for 8-mercapto-1-octanol (HSC$_8$OH).

Synthesis of bis (6,6'-dithiohexyl) perfluoroheptanoate (SC₆O₂F₇)₂ adsorbate

Bis (6-hydroxyhexyl) disulfide (0.9958 g, 3.737 mMol) and perfluorooctanoyl chloride (2.568 g, 5.93 mMol) were added to dichloromethane (100 mL) in a round bottom flask. The solution was stirred for 1 h at room temperature. Solvent was removed via rotary evaporation to yield a brownish liquid. Approximately 60 mL of ether at room temperature was added, the solution was washed with 30 mL of water

twice, and the ether was removed via rotary evaporation. Hexane was added to the solution at 40°C, filtered, and then chilled to -10°C. The remaining hexane was decanted from the solid product crystals, and the final liquid product was placed back into the freezer. 1H NMR (400 MHz, CDCl$_3$): δ = 1.4 (8H), 2.67 (4H), 4.38 (4H), 1.75 (4H), 1.65 (4H).

Photosystem I Extraction and Characterization

Commercial spinach leaves were used for the isolation of thylakoid membranes according to Reeves and Hall.[6] Further separation and isolation of native PSI involved a hydroxylapatite column previously described by Shiozawa et al.[7] and Lee et al.[8] The PSI suspension in 200 mM phosphate buffer pH 7, containing 1 mM Triton X-100, was stored at -80°C.[9] The extract contained PSI 40 (40 chlorophyll molecules per P700 center) and was characterized for chlorophyll concentration using 80% acetone[10] while the P700 concentration was determined by monitoring the chemically induced absorbance change (recording oxidized minus reduced spectra) as described by Baba *et al.*[11, 12] The absorbance change procedure was modified by using 50 mM ferrocyanide[9] and dithiothreitol as the electron donor[13] instead of 2, 6-dichlorophenol indophenol. A detailed explanation for the extraction and quantification of PSI is listed in Appendix A.

Preparation of Gold Substrates (Chapters III, IV and V)

Silicon (100) wafers were rinsed with ethanol, deionized water, and dried with N$_2$. Gold (Au) substrates were prepared by evaporating chromium (100 Å) and Au (1250 Å) in sequence onto the wafers at rates of 1-2 s^{-1} in a diffusion-pumped chamber with a base

pressure of 4 x 10^{-6} Torr. After removal from the evaporation chamber, the Au-coated

wafers were cut into ~1.4 cm x 4 cm pieces. Gold substrates in Chapters III and IV were

cleaned with piranha solution (3:1 concentrated H_2SO_4 to 30% H_2O_2) for 20 s prior to use

(CAUTION!!! Piranha solution is to be handled only in the hood with adequate

protective equipment.), thoroughly rinsed with deionized water and ethanol, and dried in

nitrogen (N_2). Other substrates were simply placed into the desired solution without

piranha cleaning the substrate. It was found that piranha cleaning did not affect the

quality of the SAM formed onto Au, therefore, later experiments (Chapter V) did not

include piranha pre-treatment.

For Chapter III, Au-coated wafers were cut into 2 cm x 2 cm pieces and

connected to a copper contact wire using conductive silver epoxy. The connection was

further insulated with epoxy sealant. A fresh piece of Au was used in each experiment to

eliminate errors that could be introduced by possible surface damage.

Preparation of SAM and PSI Modified Gold Substrates (Chapter III)

Stamps were fabricated in a clean room using lithographic masters (photoresist

pattern on silicon) donated by Professor Ki-Bum Kim (Seoul National University). By

volume, one part of elastomer curing agent to ten parts of elastomer base were mixed

thoroughly and then placed under vacuum in order to purge any entrapped air. The

mixture was then poured onto the masters and cured in a 60°C oven for 2 h. The PDMS

stamps were cut into their respective sizes (~ 10 mm x 10 mm) using a scalpel.

PDMS stamps were thoroughly rinsed with ethanol and dried in N_2, prior to using

a cotton swab (Hardwood Products Company LLC) to apply a 4 mM ethanolic solution of

the thiol across the patterned surface of the stamp. The stamp was dried with N_2 and then placed onto the flat Au surface for 30 s. If backfilling was required, the patterned Au surface was dried 30 min in open air and then immersed in a 1 mM ethanolic solution of a different ω-terminated alkanethiol for 10 min. The patterned Au was rinsed and then sonicated for 5 s in ethanol and dried in N_2.

In order to confirm successful pattern transfer from PDMS to the Au surface, stamped surfaces (not backfilled) were exposed to an etching solution of 1 mM $K_3Fe(CN)_6$ and 100 mM KCN[14] in DW (60 mL soln./cm^2 of Au) and stirred.[15] Substrates were then thoroughly rinsed with DW, dried in N_2, and observed with an Olympus BX41 optical microscope to verify that etching was limited to the exposed Au regions as shown in Figure 2.2.
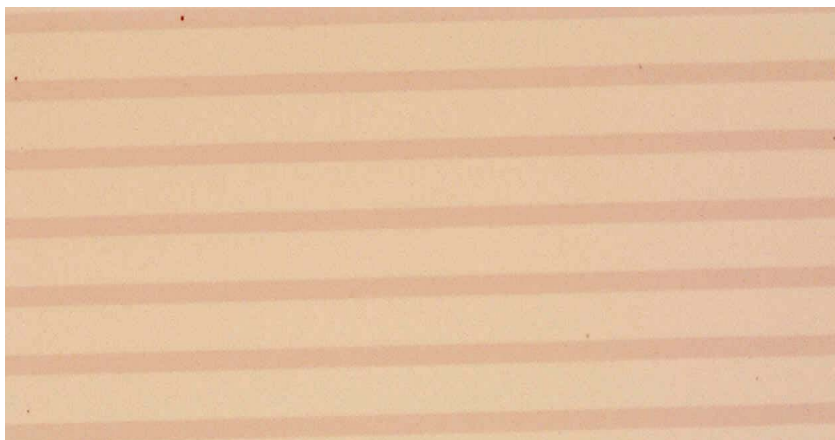
Figure 2.2. 10X bright field image of a $HSC_{11}OH$ stamped Au substrate after etching.

For PSI adsorption, the patterned Au substrate or the Au IDA (already modified by overnight exposure to 1 mM $HSC_{11}OH$ in ethanol) was placed overnight (~ 20 h) in the dark at 4 ^{o}C in a PSI solution containing ~ 50 μg chlorophyll/mL and 1 mM Triton X-100. Before use, the substrates were briefly rinsed with DW and dried in a gentle stream of N_2.

Preparation of SAM and PSI Modified Gold Substrates (Chapter IV)

If the gold substrate was piranha cleaned, it was thoroughly rinsed with water and ethanol with the final rinsing step being that of the solvent used in the alkanethiol solution and directly immersed without a drying step to eliminate the possibility of surface contamination. If the gold substrate was not piranha cleaned, it was rinsed with water and ethanol, and then dried with nitrogen before immersion into the alkanethiol solution.

Self-assembled monolayers (SAMs) were prepared by immersing the gold films into a 1 mM alkanethiol solution in ethanol overnight at room temperature for the self-assembly process to occur. SAM-modified substrates were rinsed with ethanol and deionized water, and dried in nitrogen before being placed into PSI solutions kept at 4° C.

For the majority of all experiments, PSI solutions were diluted with elution buffer since extractions only provide ~ 25 mL of PSI at a time. Typically, for dilutions used in backfilling experiments in Chapters IV and V, the concentration of P700 was ~ 1.5×10^{-7} mol L^{-1} (0.16 mL of PSI to 4 mL of elution buffer), and the solution was prepared in borosilicate glass vials wrapped with aluminum foil to prevent light from degrading the protein. Later, high density polyethylene vials wrapped in aluminum foil were used for

PSI solutions since it was suspected that the protein would adsorb to glass thereby reducing the overall concentration of PSI and leading to reproducibility issues. For each sample a fresh vial of PSI solution was used. Upon removal of substrates from PSI solutions, the substrates were rinsed with water and gently dried under nitrogen.

Backfilled PSI films were prepared by immersing the PSI-SAM-modified Au substrates in a 1 mM alkanethiol solution. We examined the backfilling of both $C_{22}SH$ and $C_{18}OC_{19}SH$ alkanethiols. $C_{22}SH$ studies included the use of ethanol, isooctane, 2-butanol, and 20 mM $C_{12}E_5$(aq). The aqueous micellar solutions of $C_{12}E_5$(aq) were first heated to 55-60° C for ~20 min to 1 h (including time required to get to 55-60° C) to melt the thiol and facilitate solubilization before cooling to room temperature for the assembly. Solutions were heated right before use since the thiol will tend to fall out of solution in time probably due to the phase transitions of the micellar structures formed upon heating and cooling.[16] Upon removal, the samples immersed in $C_{12}E_5$(aq) were rinsed thoroughly with water and dried under a stream of N_2. Samples backfilled in organic solvents were rinsed with ethanol and water, and dried in N_2.

Preparation of SAM and PSI Modified Gold Substrates (Chapter V)

Self-assembled monolayers (SAMs) formed from regular hydroxyl-terminated ω-alkanethiols were prepared by immersing the gold films into a 1 mM alkanethiol solution in ethanol overnight at room temperature for the self-assembly process to occur. $F_7O_2C_6S$/Au films were prepared from a 1 mM bis (6,6'-dithiohexyl) perfluoroheptanoate solution in N,N-dimethyl formamide (DMF) overnight at room temperature for the self-assembly process to occur. $F_7O_2C_{11}S$/Au films were prepared from a 0.5 mM bis(11,11'-

dithioundecyl) perfluoroheptanoate solution in tetrahydrofuran (THF) overnight at room temperature as noted in earlier work.[3]

Cleaved films were made by cleaving the $F_7O_2C_6S$/Au and $F_7O_2C_{11}S$/Au monolayers in a 0.1 M KOH solution in ethanol for 1 min. Samples were then rinsed thoroughly in water and ethanol, and dried in N_2.

PSI films were prepared as mentioned earlier for Chapter IV.

Backfilled SAMs were prepared by immersing the assembled PSI-SAM-Au films into a 1 mM alkanethiol solution of the alkanethiol of interest. We have examined the backfilling of $C_{22}SH$ in 20 mM $C_{12}E_5$ (aq) for 10 min. The aqueous micellar solutions of $C_{12}E_5$ were first heated to 55-60° C for ~20 min to 1 h (including time required to get to 55-60° C) to melt the thiol and facilitate solubilization before cooling to room temperature for the assembly. Solutions were heated right before use since the thiol will tend to fall out of solution in time probably due to the phase transitions of the micellar structures formed upon heating and cooling.[16] Upon removal, the samples were rinsed thoroughly with water and dried under a stream of N_2.

Preparation of Modified Gold Electrodes (Chapter VI)

Au disk working electrodes (WEs) were polished with 0.05 μm alumina from Buehler, sonicated in ethanol and water, dried in N_2, and electrochemically cleaned for 5 min in 0.5 M H_2SO_4. The exposed Au area for all experiments was 0.03 cm^2.

Electrode Modification and Conditions for Dark Experiments

The SAMs were formed by immersion of Au disk electrodes for 7 days into a 1 mM solution of the thiol in ethanol (other immersion times, and/or combination of SAM formation methods such as thermal annealing or repeated immersions failed to give good PSI peaks). The SAM-modified electrodes were then rinsed and sonicated for 5 s in ethanol and dried in N_2. Cyclic voltammetry (CV) and square wave voltammetry (SWV) experiments (dark, room temperature) were taken for each of the SAM-coated electrodes and the resulting voltammograms were used as backgrounds for the experiments where background subtraction was performed. Thus, each electrode had its own background voltammograms that would account for any capacitive background characteristics for the individual electrodes. The measurements were performed in buffer (200 mM phosphate buffer, pH 7.0, 1 mM Triton X-100). The electrodes were then rinsed briefly with DW, ethanol, dried in N_2, and re-immersed in their corresponding ethanolic thiol solutions for 45 min. Afterwards, the electrodes were rinsed and sonicated for 5 s in ethanol and dried in N_2. The SAM-modified electrodes were then immersed overnight (~ 20 h) in the PSI solution (200 mM phosphate buffer, pH 7.0, 1 mM Triton X-100) in the dark at 4 $^{\circ}$C; the same PSI solution (total chlorophyll concentration 0.2 mg/mL) was used for performing the CV and the SWV experiments (dark, room temperature). The potential window was not scanned above + 0.6 V *vs*. Ag/AgCl, 3 M KCl, due to the complex Au oxide peaks present at higher potentials. Also, higher potentials were undesirable because they can deteriorate the SAM.[17] Control experiments were also performed where, after recording the background voltammograms for each individual electrode, the SAM-modified electrodes were immersed overnight at 4 $^{\circ}$C in buffer solution (200 mM phosphate buffer,

40

pH 7.0, 1 mM Triton X-100) without PSI. This same buffer was used the next day for performing the CV and the SWV experiments (dark, room temperature) for the control electrodes.

Electrode Modification and Conditions for Light Experiments

The SAMs were formed by immersion of Au disk electrodes for 7 days in a 1 mM thiol ethanolic solution. The SAM-modified electrodes were then rinsed and sonicated for 5 s in ethanol and dried in N_2. No background measurements were performed for this type of experiment. For PSI adsorption, the modified electrodes were further placed overnight (~ 20 h) in the dark at 4 ^{o}C in a PSI solution containing ~ 0.2 mg/mL chlorophyll and 1 mM Triton X-100. Before use, the electrodes were briefly rinsed with DW. The light experiments (chronoamperometry) were conducted in 50 mM phosphate buffer pH 7.0 with a 250 W cold light source (Leica, model KL2500 LCD) equipped with a red filter. The solution also contained methyl viologen (MV^{2+}, 250 µM). No detergent was present in the solution. Control experiments were also performed, where the SAM-coated electrodes were immersed overnight at 4 ^{o}C in buffer solutions (200 mM phosphate buffer, pH 7.0, 1 mM Triton X-100) without PSI. The control electrodes were briefly rinsed with DW the next day and employed in chronoamperometry in a similar manner to the PSI electrodes.

Characterization Methods

Reflectance Absorption Infrared Spectroscopy (RAIRS)

Fourier Transform Infrared Spectroscopy (FTIR) is widely used to determine chemical composition because of its numerous advantages such as high resolution and rapid data collection.[18] Fourier transform instruments have few optical elements and no slits to attenuate radiation so power and signal-to-noise ratios are high. All elements of the source reach the detector at the same time so an entire spectrum can theoretically be recorded in one second or less.[19] Fourier transform instruments collect data in the time domain and mathematically convert data to the frequency domain using triangular apodization and a fast Fourier transform. Various types of infrared spectroscopy exist such as diffuse reflectance infrared spectrometry (DRIFTS) for analysis of powders, attenuated total reflectance spectrometry (ATRS) for analysis of aqueous solutions,[20] and reflectance absorption infrared spectroscopy (RAIRS) for analysis of thin films on reflective metal surfaces.

Reflectance absorption infrared spectroscopy (RAIRS) is a non-destructive technique used to determine organic thin film composition and structure on a surface. In RAIRS, the polarized light is incident at a grazing angle (10°) from the surface parallel and reflected at the metal surface. The reflected light creates an electric field normal to the surface, which can excite transition dipole moments within the film on the surface. Absorbance of radiation in the IR region of the electromagnetic spectrum (400 to 4000 cm^{-1}) causes molecules in the film to vibrate in various modes such as bending, stretching, scissoring, twisting, wagging, and rocking. Because of surface selection we

can obtain structural information in an organic thin film. Peak positions and intensities for a particular type of vibrational mode provide information about the chemical functionality as well as degree of packing and orientation of functional groups on the surface. Table 2.1 lists the peak positions and chemical group assignments for IR peaks of particular chemical functionalities encountered in this study.

Table 2.1. Absorption regions of interest in infrared spectra.

Absorption Range (cm⁻¹)	Assignment	Information
1000-3000	C-O (stretching)	
1100-1400	C-F (stretching)	
1400-1500	C-H (bending)	
1300-1400	Amide III	40% C-N stretch and 30% N-H bend
1500-1600	Amide II	60% N-H bend and 40% C-N stretch
1600-1700	Amide I	80% C=O stretch
1700-1800	C=O (stretching)	
2800-2950	C-H (stretching)	
2918-2930	CH_2 a	asymmetric methylene stretching
2850-2930	CH_2 s	symmetric methylene stretching
2963-2967	CH_3 a	asymmetric methyl stretching
2878-2881	CH_3 s	symmetric methyl stretching
3000-3700	O-H (stretching)	

Peak intensities for a stretching or bending mode from RAIRS can be used to calculate the average angle, θ_{mz}, between the surface normal, z, and the transition dipole moment, m, from the following equation:[21]

$$I \propto cos^2 \theta_{mz} \tag{2-1}$$

where I represents the spectral intensity. This equation implies that the intensity of the band will be highest when the transition dipole moment is normal to the surface.

For a SAM, the average cant (α) and twist (β) of the alkanethiol chain can be determined from peak intensities assuming an all-trans chain arrangement. The structure of the SAM can be determined from the wavenumber positions of each C-H stretching peak that infer the extent to which the monolayer exhibits liquid-like or crystalline-like structure depending on the degree of packing.[22-24] For example, asymmetric methylene positions located from 2918-2920 cm^{-1} indicate a crystalline monolayer whereas positions located from 2922-2926 cm^{-1} indicate liquid-like packing.[21]

RAIRS has also been used to determine the secondary structure of proteins as well as the structure of SAMs. Proteins show strong absorption bands in the 1500 to 1700 cm^{-1} region[25] due to the presence of amide bonds (R-(C=O)-NH$_2$). When a hydrogen bond is formed between the carbonyl group and the amide nitrogen of the same polypeptide, the protein coils into a rod-like structure referred to as the α helix. When these bonds form between different polypeptides, a sheet structure is formed and referred to as the β sheet. By monitoring changes in the amide bonds we can directly correlate this information into changes in the α helix and β sheet structure of the protein. When proteins denature, the percentage of secondary structure will change indicating that the bonds between various polypeptides have been altered. Conformational changes in Photosystem I and II, when exposed to denaturing and nondenaturing conditions, have been studied by monitoring changes in secondary structure through FTIR.[26]

There are nine bands that correspond to the peptide groups within proteins: Amide A, B, I, II, III, IV, V, VI, VII. The major bands of interest in protein adsorption correspond to the Amide I and II bands. The Amide A (3500 cm^{-1}) and B (3100 cm^{-1}) bands arise from a Fermi resonance between the first overtone of the Amide II band and

the N-H stretching vibration.[27] The Amide I band at 1600-1700 cm^{-1} arises primarily

from the C=O stretching mode of the amide functional group with the remainder due to

C-N stretching.[27] The Amide II band at 1500-1600 cm^{-1} arises from N-H bending (40-

60%) and C-N stretching vibrations (18-40%).[28] The Amide III band (1300-1400 cm^{-1})

arises from 40% C-N stretching and 30% N-H bending.[28]

Spectral deconvolution of the Amide I band (1600-1790 cm^{-1}) was performed

using Merlin-Pro software. The software uses a Lorentzian curve-fitting technique and

allows for K-values and peak half-width values to be varied such that individual peaks

with the second derivative curve-fit program, also in the software, matched peaks within

2 cm^{-1} of the deconvoluted spectrum. Peak half-width and K-values were varied from 6-

8 cm^{-1} and 2-4, respectively. Secondary structure peak assignments were made according

to Table 2.2, and the areas under the individual peaks from the deconvoluted curve were

used to determine the percentage of each component.

Table 2.2. Secondary structure peak assignments.

	β Turn	β Sheet	Unordered Helix	α Helix
Wavenumber (cm^{-1})	1616-1620 [25, 29, 30] 1680-1690 [26, 30-32]	1624-1636 [26, 29-37] 1692-1697 [26, 33, 34]	1638-1645 [31-34]	1648-1660 [25, 26, 29, 31-39] 1663-1667 [29, 30, 38]

RAIRS was performed using a Bio-Rad Excalibur FTS-3000 infrared

spectrometer. The p-polarized light was incident at 80° from the surface normal. The

instrument was run in single reflection mode and equipped with a universal sampling

accessory. A liquid-nitrogen cooled, narrow band mercury cadmium telluride detector

was used to detect reflected light. Spectral resolution was 2 cm^{-1} after triangular

apodization. Each spectrum was collected over 2000 scans with a SAM prepared from deuterated octadecanethiol-d_{37} on gold as the background. The presence of water was minimized by flowing nitrogen gas through the sample compartment at a flow rate of roughly 4.5 standard liters per minute for at least 1-2 h before scanning and during scanning. A water spectrum was created by rescanning the background sample in the presence of water vapor, and subtracted from the spectrum of each sample. Water subtraction was performed to better resolve the peaks of interest in the 1200-1900 cm^{-1} region.

Contact Angle Goniometry

Surface properties, such as wetting, are governed by the composition at the outermost 3-5 Å of a surface.[40] The most common method of evaluating wetting is to measure the contact angle of a drop of water or other liquid on the surface. The contact angle, θ, is defined as shown in Figure 2.3. Wetting has been proven to be an invaluable method for probing the character of solid-liquid interfaces.[41] Wetting can infer surface properties such as hydrophobicity and hydrophilicity.[42-46]

The apparent contact angle is measured using a microscope of low power or a piece of equipment known as the goniometer. The equilibrium contact angle is related to the interfacial tensions of the solid-vapor, solid-liquid, and liquid-vapor interfaces through Young's equation:[47]

$$\gamma_{SV} - \gamma_{SL} = \gamma_{LV} \cos \theta \qquad\qquad (2\text{--}2)$$

where γ_{SV} represents the interfacial force or tension at the solid-vapor interface, γ_{SL} represents the interfacial force or tension at the solid-liquid interface, γ_{LV} represents the interfacial force or tension at the liquid-vapor, and the static, equilibrium contact angle, θ, is the angle between the line drawn tangent to the edge of the liquid drop and the surface underneath the drop. The contact angle is low when the solid has a high surface energy or the liquid surface tension is low.[48]

Tail Group (X)	n	$\theta(H_2O)$
High Energy		
CO_2H	10	<15,0
	15	<15,0
	11	15,0
OH	11	<15,0
	16	<15,0
	19	<15,0
Low Energy		
CH_3	17	115,105
	21	117,100

Contact angle measurements are listed as advancing, receding contact angles respectively
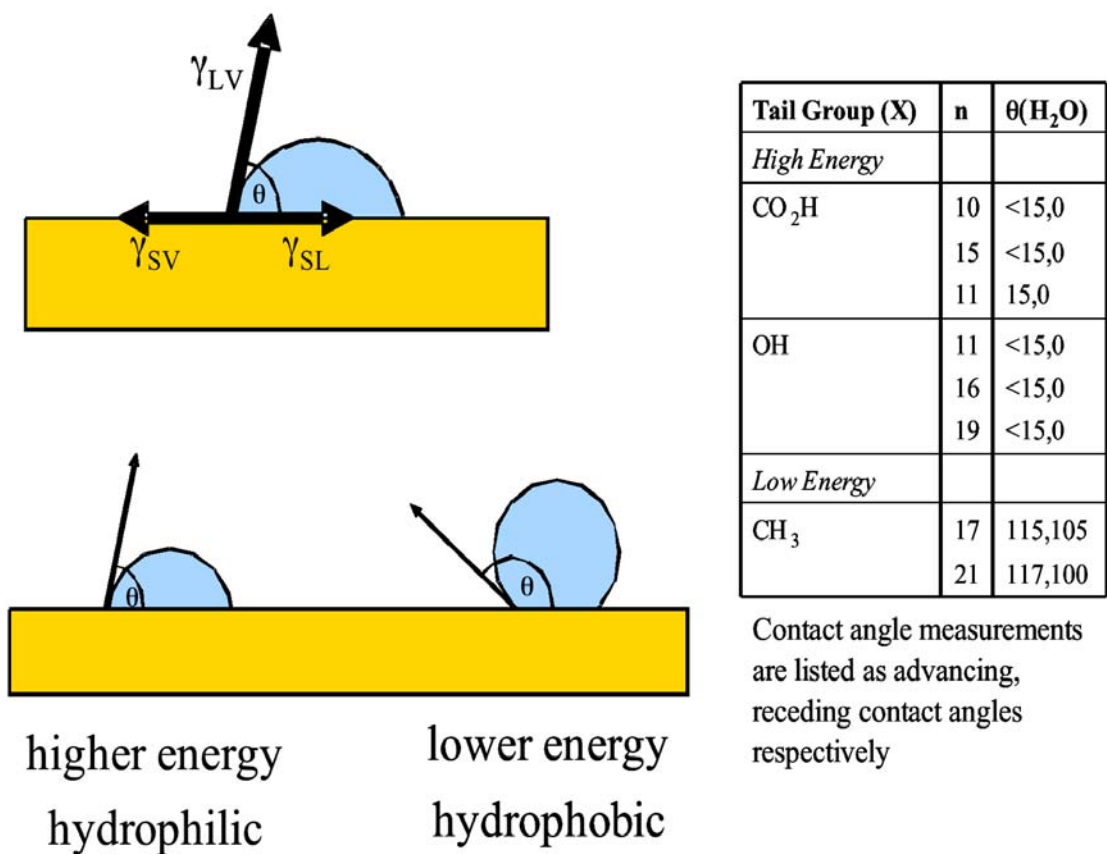
Figure 2.3. Contact angle designation.

Generally, the contact angle that is most reported in the literature is the advancing contact angle, θ_A, which is measured with the syringe tip in the droplet after liquid is

added to the droplet so that the edge of the droplet advances. The receding contact angle, θ_R, is measured after the liquid is removed from the droplet until the edge of the droplet recedes inward. By measuring both the receding and advancing contact angles, the amount of contact angle hysteresis (H)[49] can be used to determine the amount of roughness or chemical heterogeneity[50] on a surface:

$$H = \theta_A - \theta_R \qquad\qquad\qquad (2\text{-}3)$$

where θ_A is the advancing contact angle and θ_R is the receding contact angle. If the difference between the advancing and receding contact angles is small $(< \sim10°)$, then the surface can be thought of as smooth, while higher hysteresis values signify a rough surface. The receding angle will always be smaller than the advancing angle on a real surface.

A Rame-Hart goniometer with a microliter syringe was used to measure advancing contact angles on static drops of water on the modified substrates. The needle tip of the syringe remained inside the liquid drop while measurements were taken on both sides of ~5 μL drops. Reported values and ranges represent the average and standard deviations of three drops per sample with both edges measured per drop.

Electrochemistry

In order to understand the photoelectrochemical nature of PSI, we can use bulk electrochemical techniques to examine the oxidative and reductive behavior of PSI immobilized on a gold surface and also in solution. In order to reduce and oxidize

components in PSI, electrons must tunnel from the underlying gold through the SAM (if present) to the protein. The probability of electron tunneling is proportional to the exponential decay of the distance between the electrode and the cofactor.[51, 52] Varying the chain length of the alkanethiol regulates the rate of electron transfer

$$k = k_0 \, exp(-(\beta_1 d_{SAM} + \beta_2 d_{PSI})) \tag{2-4}$$

where d_{SAM} is the thickness of the SAM, d_{PSI} is the length of the protein complex between the SAM and the specific cofactor, β_1 is a decay factor for the SAM (1.09 per methylene group),[53] β_2 is a decay factor for the protein, and k_0 is the electron transfer rate extrapolated to zero thickness for the protein and SAM. (Figure 2.4)
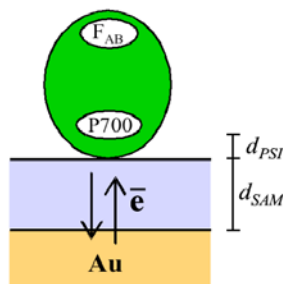
Figure 2.4. Electron transfer distances involved in the direct electrochemistry of PSI on a SAM-modified Au substrate.

Cyclic Voltammetry (CV)

Cyclic voltammetry is a potential sweep method in which current is measured as a function of potential. The reduction and oxidation of an analyte in an ionic solution at

49

the surface of a metal electrode occurs when the potential reaches the switching potential, which is well past that of the midpoint potential for the analyte. The potential is gradually ramped until a complete cycle of more positive and more negative potential values, as compared to the midpoint potential, are achieved.

Typically, both the cathodic and anodic peaks are observed in a cyclic voltammogram. At the cathodic peak, the oxidized species is depleted whereas the reduced species is depleted at the anodic peak. As the potential is ramped past the anodic or cathodic peak, the shape of the cyclic voltammogram follows diffusion-limited current given by the Cottrell equation:

$$i(t) = \frac{nFAD_O^{1/2}C_O}{\pi^{1/2}t^{1/2}}$$

(2-5)

where $i(t)$ is the current at time t, n is the number of electrons involved in the oxidation-reduction reaction, A is the area of the electrode, D_O is the diffusion coefficient, and C_O is the concentration of the analyte.

The relationship between the voltage and the concentration of the analyte species can be described by the Nernst equation:

$$E = E^0 + \frac{RT}{nF}\ln\frac{C_O}{C_R}$$

(2-6)

where E is the applied potential difference between the working and the reference electrodes, E^0 is the standard electrode potential, R is the ideal gas constant, T is the

temperature, n is the number of electrons involved in the oxidation-reduction reaction, F is the Faraday constant, C_O is the concentration of the oxidized species, and C_R is the concentration of the reduced species.

Square Wave Voltammetry (SWV)

Square wave voltammetry is a pulse voltammetry method, which also measures current as a function of potential; however, the graph of potential versus time resembles a staircase where current samples are taken twice per cycle. The forward current is taken from the first pulse, and the reverse current is taken at the end of the second pulse in the opposite direction. Square wave voltammetry is more sensitive to lower concentrations of analyte since the background current is suppressed by cancellation of interfacial capacitance and Faradaic current after subtraction of the forward and reverse currents since these processes do not change significantly from the first current sample to the next.[51]

Chronoamperometry

Chronoamperometry is an electrochemical method where the potential is held at a constant value while monitoring the current. Interpretation of chronoamperometry data is based upon the Cottrell equation (see Eq 2-5), which defines the dependence of the current on the diffusion of the analyte to the surface.

CV, SWV, and chronoamperometry measurements were conducted with a CHI660a electrochemical workstation from CH Instruments equipped with a Faraday cage. The electrochemical cell was in a typical three-electrode configuration: working

electrode (WE), which was a 2 mm Au disk (CHI101), Pt wire counter electrode, and Ag/AgCl/ 3 M KCl reference electrode (CHI111). Au disk WEs were polished with 0.05 µm alumina from Buehler, sonicated in ethanol and water, dried in N_2, and electrochemically cleaned for 5 min in 0.5 M H_2SO_4. The exposed Au area for all experiments was 0.03 cm^2.

Electrochemical Impedance Spectroscopy (EIS)

Electrochemical impedance spectroscopy (EIS) has been used in a variety of systems such as corrosion,[54] polymer films,[55] porous membranes,[56] and semiconductors[57] to examine the electron transfer reactions of solution components in relation to each system. The history of EIS can be found in a recent review by MacDonald.[58]

EIS involves the application of an alternating current (AC) potential with a sinusoidal component of frequency to an electrode while measuring the current obtained as a function of frequency and phase as shown in the following equation:

$$Z = \frac{E(t)}{I(t)} = \frac{E_0 \cos(\omega t)}{I_0 \cos(\omega t - \phi)} \tag{2-7}$$

where Z is the impedance of the system, $E(t)$ is the applied potential at time t, $I(t)$ is the resulting current at time t, E_0 is the amplitude of the potential, ω is the radial frequency, I_0 is the amplitude of the current, and ϕ is the phase shift of the output signal.

EIS data is typically presented in the form of a Bode plot or a Nyquist plot. The Nyquist plot displays the imaginary and real components of the impedance for different values of frequency, which means that a simple examination of the Nyquist plot will not

give any direct information about the frequency used during the experiment. In a Bode plot, the absolute value of the impedance and the phase shift is plotted versus the log of frequency.

In order to extract qualitative information from EIS measurements, the results are modeled with equivalent electrical circuits. The most frequently used circuit is the Randles equivalent circuit, which consists of a solution resistance, a double layer capacitance, and a charge transfer resistance as shown in Figure 2.5.
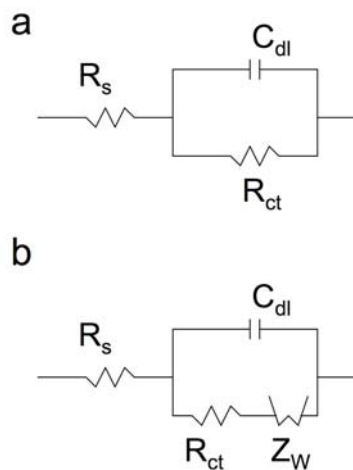
Figure 2.5. (a) Randles equivalent circuit model and an (b) equivalent circuit model with a Warburg impedance, Z_W, to account for diffusion-limited transport of ions.

EIS was performed with a Gamry Instruments CMS300 impedance system interfaced to a personal computer. The electrochemical cell consisted of an aqueous solution of 0.1 M Na_2SO_4, 1 mM $K_3Fe(CN)_6$ and 1 mM $K_4Fe(CN)_6$ with an Ag/AgCl/3M KCl reference electrode, a gold substrate counter electrode, and a gold substrate containing the film to be studied as the working electrode. All data were collected in the

range from 10^{-1} to 10^4 Hz using 10 points per decade and were fit using an appropriate equivalent circuit model to determine resistance and capacitance values. Reported values and ranges represent the average and standard deviations of 4 independent sample measurements.

Spectroscopic Ellipsometry (SE)

Spectroscopic ellipsometry allows non-destructive optical measurements of film thicknesses by monitoring the change in the polarization state of light upon reflection from a surface containing a thin film. Some of the advantages of spectroscopic ellipsometry include its high accuracy and reproducibility, insusceptibility to scatter and lamp fluctuations, and the lack of need for a reference sample.

Measured values, Ψ and Δ, can be related to the ratio of Fresnel reflection coefficients, R_p and R_s, for p- and s-polarized light (Figure 2.6) as shown in the following equation:

$$R_s \, tan(\Psi) \, exp(i\Delta) = R_p \qquad\qquad (2\text{-}8)$$

In order to obtain accurate thickness measurements, several steps are necessary aside from acquiring Ψ and Δ values. The first step is to construct an optical model that describes the layers of the sample structure. Once an optical model is developed, the theoretical result from the model is compared to the experimental result and a thickness fit is obtained. The optical constants, n and k, are characteristic parameters that are

functions of the interaction of light with a material and can either be set as specific values

used to obtain the thickness fit or varied and fit point by point.

Ellipsometry is sensitive to thin films due in part to the change in Δ which carries

the phase information. The intensity of the reflected light is not greatly affected by a thin

dielectric layer. Since Ψ carries the reflected intensity information there is no significant

change in Ψ for thin films. However, the phase difference between the s-wave and p-

wave is significantly noticeable and will produce a change in Δ.[59] Typically, optical

constants and thicknesses cannot be easily obtained simultaneously for very thin films.
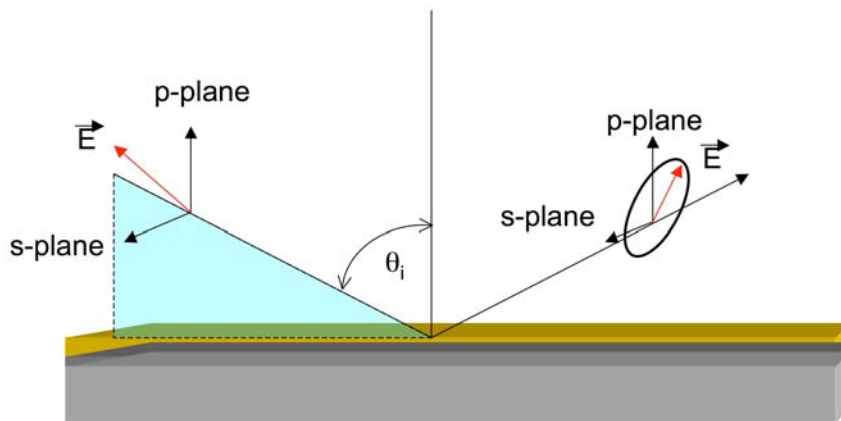
Figure 2.6.   Schematic of s- and p-polarized light involved in the principle of measurements obtained by spectroscopic ellipsometry.

SE measurements were taken on a J. A. Woollam Co. M-2000D variable angle

spectroscopic ellipsometer with WVASE32 software for modeling. Measurements at

three spots per sample were taken with light incident at angles of 82°, 83°, and 84°

(except for Chapter V where only 83° was used) from the surface normal in accordance

with the Brewster angle for gold of $83°$[59, 60] using wavelengths of 400 nm to 700 nm and 600 revolutions of the analyzer per measurement to reduce noise. Optical constants for the SAM substrates were determined by a point by point fit at all wavelengths under a steady stream of nitrogen to reduce contamination of the high-energy surface from exposure to air. These optical constants were saved and used a baseline for all other measurements. Film thickness of the PSI layer on top of the SAM/Au substrate were measured under a steady stream of nitrogen and fit using a one-term Cauchy layer model with a refractive index of 1.33[61-65] and an absorption coefficient of 0. The data were also fit by selecting wavelengths in the region where PSI would not absorb strongly (500 nm to 600 nm) supporting the use of 0 for the absorption coefficient, and the thickness values did not differ by a statistical significance. Thickness measurements were based upon an average of at least 4 independent samples.

Scanning Electrochemical Microscopy (SECM)

Scanning electrochemical microscopy (SECM) uses a four-electrode cell to image the electrochemical properties of surfaces. The four electrodes consist of a reference, counter, substrate, and tip. SECM is a variation of scanning probe microscopy developed by Bard in 1989.[66] The SECM rasters a tip over the surface in an electrolyte solution. The tip is always an ultramicroelectrode (UME) (≤ 25 μm) that measures Faradaic current from redox reactions of solution species (electrochemical mediator).

The most important aspect of SECM is the UME. When the tip is positioned far from the substrate electrode, the diffusion-layer thickness is large compared to the

dimension of the UME, the measured current at the UME approaches a steady state, [51] which is defined as:

$$i_{T, \infty} = 4nFDCa \tag{2-9}$$

where the steady-state limiting current at infinite tip-substrate separation is a function of the number of electrons, n, the Faraday constant, F, the diffusion coefficient of the redox species, D, the concentration of the redox species, C, and the radius of the tip electrode, a.

In order to image the surface topography and reactivity, the tip must first be placed close to the surface without touching the surface. This can be done by the use of approach curves. Current of the tip versus distance between the tip and the substrate data are referred to as approach curves. Approach curves are used to position the tip within a few microns of the substrate without crashing the tip into the surface.

There are two types of modes of operation in SECM, collection mode and feedback mode. Feedback mode utilizes the Faradaic current from the mediator species in solution that cycles charge between the UME tip and the surface of the substrate to determine properties of the surface. In positive feedback, the oxidation and reduction of the mediator becomes more efficient as the distance between the tip and substrate decreases. This decrease in distance causes the current to increase compared to the initial steady-state value, indicating a conductive surface. In negative feedback, the reverse is observed, indicating that the surface is insulating.

In feedback, the reaction on the tip is studied, while in collection mode, the tip can act as the generator or collector of the reactive species. In tip generation/substrate collection mode (TG/SC), the tip generates the product of interest, for example the reductant, and the substrate electrode converts that product back to the oxidant. The reverse is true of substrate generation/tip collection (SG/TC) mode.

The study presented in Chapter III uses substrate generation/tip collection (SG/TC) imaging mode, which arises from the detection of a species being generated at the substrate while the electroactive species is collected at the UME tip. SG/TC mode has previously been used to make concentration maps of corroding metal surfaces, biological materials, and polymeric materials.

SECM measurements were conducted with a CHI900 instrument from CH Instruments equipped with an adjustable stage for tilt correction. The electrochemical cell was in a typical four-electrode configuration: UME tip electrode, Pt wire counter electrode, Ag/AgCl, 3 M KCl reference electrode (CHI111), and substrate electrode, which was either a 2 mm Pt disk (CHI303) for UME testing, or evaporated Au for imaging. All UMEs were manufactured with 5 μm Pt wire from Goodfellow according to Bard et al.,[67] polished with 0.05 μm alumina from Buehler, and sonicated in ethanol and water. The actual measured radius for the UMEs was $a = 3.5$ μm. UMEs were electrochemically cleaned for 5 min in 0.5 M H_2SO_4 using a CHI660a potentiostat, and were tested with 1 mM FcTMA in 100 mM KCl for performance. The Pt SE was polished and cleaned in an identical manner to the UMEs.

References

1. Jennings, G. K.; Laibinis, P. E., Self-Assembled n-Alkanethiolate Monolayers on Underpotentially Deposited Adlayers of Silver and Copper on Gold. *Journal of the American Chemical Society* **1997,** 119, (22), 5208-5214.

2. Jennings, G. K.; Yong, T. H.; Munro, J. C.; Laibinis, P. E., Structural Effects on the Barrier Properties of Self-Assembled Monolayers Formed from Long-Chain ω-Alkoxy-*n*-Alkanethiols on Copper. *Journal of the American Chemical Society* **2003,** 125, (10), 2950-2957.

3. Berron, B.; Jennings, G. K., Loosely Packed, Hydroxyl Terminated SAMs on Gold. *Langmuir* **2006,** submitted.

4. Forouzan, F.; Bard, A. J.; Mirkin, M. V., Voltammetric and Scanning Electrochemical Microscopic Studies of the Adsorption Kinetics and Self-Assembly of *n*-Alkanethiol Monolayers on Gold. *Israel Journal of Chemistry* **1997,** 37, (2-3), 155-163.

5. Iglesias, L. E.; Baldesari, A.; Gros, E. G., Simple Procedures for the Preparation of α-ω-Hydroxylalkanethiols. *Organic Preparations and Procedures Int.* **1996,** 28, (3), 319-324.

6. Reeves, S. G.; Hall, D. O., Higher Plant Chloroplasts and Grana: General Preparative Procedures (Excluding High Carbon Dioxide Fixation Ability Chloroplasts). In *Methods in Enzymology*, Colowick, S. P.; Kaplan, N. O., Eds. Academic Press: New York, 1980; Vol. 69, pp 85-94.

7. Shiozawa, J. A.; Alberte, R. S.; Thornber, J. P., The P700-Chlorophyll a -Protein: Isolation and Some Characteristics of the Complex in Higher Plants. In *Archives of Biochemistry and Biophysics*, Academic Press: 1974; Vol. 165, pp 388-397.

8. Lee, I.; Lee, J.; Stubna, A.; Greenbaum, E., Measurement of Electrostatic Potentials above Oriented Single Photosynthetic Reaction Centers. *Journal of Physical Chemistry B* **2000,** 104, 2439-2443.

9. Hui, Y.; Jie, W.; Carpentier, R., Degradation of the Photosystem I Complex During Photoinhibition. *Photochemistry and Photobiology* **2000,** 72, (4), 508-512.

10.	Arnon, D. I., Copper Enzymes in Isolated Chloroplasts, Polyphenoloxidase in *Beta Vulgaris*. *Plant Physiology* **1949,** 24, (1), 1-15.

11.	Baba, K.; Itoh, S.; Hastings, G.; Hoshina, S., Photoinhibition of Photosystem I Electron Transfer Activity in Isolated Photosystem I Preparations with Different Chlorophyll Contents. *Photosynthesis Research* **1996,** 47, 121-130.

12.	Ciobanu, M.; Kincaid, H. A.; Jennings, G. K.; Cliffel, D. E., Photosystem I Patterning Imaged by Scanning Electrochemical Microscopy. *Langmuir* **2005,** 21, 692-698.

13.	Krasnovsky, A. A.; Hastings, G.; Hoshina, S., Efficiency of Hydrogen Photoproduction by Chloroplast-Bacterial Hydrogenase Systems. *Plant Physiology* **1980,** 66, (5), 925-930.

14.	Kumar, A.; Biebuyck, H. A.; Whitesides, G. M., Patterning Self-Assembled Monolayers: Applications in Materials Science. *Langmuir* **1994,** 10(5), 1498-1511.

15.	Zhao, X.-M.; Wilbur, J. L.; Whitesides, G. M., Using Two-Stage Chemical Amplification to Determine the Density of Defects in Self-Assembled Monolayers of Alkanethiolates on Gold. *Langmuir* **1996,** 12, (13), 3257-3264.

16.	Mitchell, D. J.; Tiddy, G. J. T.; Waring, L.; Bostock, T.; McDonald, M. P., Phase Behavior of Polyoxyethylene Surfactants with Water. *Journal of Chemical Society. Faraday Transactions I* **1983,** 79, 975-1000.

17.	Gooding, J. J.; Mearns, F.; Yang, W.; Liu, J., Self-Assembled Monolayers into the 21st Century: Recent Advances and Applications. *Electroanalysis* **2003,** 15, (2), 81-96.

18.	Silverstein, R. M.; Webster, F. X., *Spectrometric Identification of Organic Compounds*. Sixth Edition ed.; John Wiley & Sons, Inc.: 1998; p 482.

19.	Skoog, D. A.; Holler, F. J.; Nieman, T. A., *Principles of Instrumental Analysis*. Fifth Edition ed.; Saunders College Publishing: Orlando, 1998; p 849.

20. Gebel, M. E.; Kaleuati, M. A.; Finlayson-Pitts, B. J., Measurement of Organics Using Three FTIR Techniques: Absorption, Attenuated Total Reflectance, and Diffuse Reflectance. *Journal of Chemical Education* **2003,** 80, (6), 672-675.

21. Nuzzo, R. G.; Dubois, L. H.; Allara, D. L., Fundamental-Studies of Microscopic Wetting on Organic-Surfaces .1. Formation and Structural Characterization of a Self-Consistent Series of Polyfunctional Organic Monolayers. *Journal of the American Chemical Society* **1990,** 112, (2), 558-569.

22. Duwez, A.-S., Exploiting Electron Spectroscopies to Probe the Structure and Organization of Self-Assembled Monolayers: A Review. *Journal of Electron Spectroscopy and Related Phenomena* **2004,** 134, 97-138.

23. Porter, M. D.; Bright, T. B.; Allara, D. L.; Chidsey, C. E. D., Spontaneously Organized Molecular Assemblies. 4. Structural Characterization of n-Alkyl Thiol Monolayers on Gold by Optical Ellipsometry, Infrared Spectroscopy, and Electrochemistry. *Journal of the American Chemical Society* **1987,** 109, (12), 3559-3568.

24. Strong, L.; Whitesides, G. M., Structures of Self-Assembled Monolayer Films of Organosulfur Compounds Adsorbed on Gold Single-Crystals - Electron-Diffraction Studies. *Langmuir* **1988,** 4, (3), 546-558.

25. Seshadri, S.; Khurana, R.; Fink, A. L., Fourier Transform Infrared Spectroscopy in Analysis of Protein Deposits. *Mehods in Enzymology* **1999,** 309, (36), 559-576.

26. Ruan, X.; Wei, J.; Xu, Q.; Wang, J.-s.; Gong, Y.-d.; Zhang, X.-f.; Kuang, T.-y.; Zhao, N.-m., Comparison of the Effects of Triton X-100 on the Protein Secondary Structure of Photosystem I and Photosystem II studied by FTIR Spectroscopy. *Journal of Molecular Structure* **2000,** 525, 97-106.

27. Bellamy, L. J., Amides, Proteins and Polypeptides. In *The Infrared Spectra of Complex Molecules*, 3rd ed.; Chapman and Hall: London, 1975; pp 232-259.

28. Pelton, J. T.; McLean, L. R., Spectroscopic Methods for Analysis of Protein Secondary Structure. *Analytical Biochemistry* **2000,** 277, 167-176.

29. Arrondo, J. L.; Goni, F. M., Structure and Dynamics of Membrane Proteins as Studied by Infrared Spectroscopy. *Progress in Biophysics and Molecular Biology* **1999,** 72, 367-405.

30. Khurana, R.; Fink, A. L., Do Parallel Beta-Helix Proteins Have a Unique Fourier Transform Infrared Spectrum? *Biophysical Journal* **2000,** 78, 994-1000.

31. Giacomelli, C. E.; Bremer, M.; Norde, W., ATR-FTIR Study of IgG Adsorbed on Different Silica Surfaces. *Journal of Colloid and Interface Science* **1999,** 220, 13-23.

32. Guiomar, A. J.; Guthrie, J. T.; Evans, S. D., Use of Mixed Self-Assembled Monolayers in a Study of the Effect of the Microenvironment on Immobilized Glucose Oxidase. *Langmuir* **1999,** 15, 1198-1207.

33. Fu, K.; Griebenow, K.; Hsieh, L.; Klibanov, A. M.; Langer, R., FTIR Characterization of the Secondary Structure of Proteins Encapsulated within PLGA Microspheres. *Journal of Controlled Release* **1999,** 58, 357-366.

34. Gilbert, S. M.; Wellner, N.; Belton, P. S.; Greenfield, J. A.; Siligardi, G.; Shewry, P. R.; Tatham, A. S., Expression and Characterization of a Highly Repetitive Peptide Derived from a Wheat Seed Storage Protein. *Biochimica et Biophysica Acta* **2000,** 1479, 135-146.

35. Kota, Z.; Szalontai, B.; Droppa, M.; Horvath, G.; Pali, T., Fourier Transform Infrared and Electron Paramagnetic Resonance Spectroscopic Studies of Thylakoid Membranes. *Journal of Molecular Structure* **1999,** 480-481, 395-400.

36. Krueger, J. K.; Gallagher, S. C.; Wang, C. L.; Trewhalla, J., Calmodulin Remains Extended Upon Binding to Smooth Muscle Caldesmon: A Combined Small-Angle Scattering and Fourier Transform Infrared Spectroscopy Study. *Biochemistry* **2000,** 39, 3979-3987.

37. Zhang, H.; Yamamoto, Y.; Ishikawa, Y.; Carpentier, R., Characterization of the Secondary Structure and Thermostability of the Extrinsic 6 Kilodalton Protein of Spinach Photosystem II by Fourier Transform Infrared Spectroscopy. *Journal of Molecular Structure* **1999,** 513, 127-132.

38. Heimburg, T.; Schunemann, J.; Weber, K.; Geisler, N., FTIR-Spectroscopy of Multistranded Coiled Coil Proteins. *Biochemistry* **1999,** 38, 12727-12734.

39. Vandenbussche, G.; Clercx, A.; Curstedt, T.; Johansson, J.; Jornvall, H., Structure and Orientation of the Surfactant-Associated Protein C in a Lipid Bilayer. *European Journal of Biochemistry* **1992,** 203, (1-2), 201-209.

40. Laibinis, P. E.; Bain, C. D.; Nuzzo, R. G.; Whitesides, G. M., Structure and Wetting Properties of ω-Alkoxy-n-Alkanethiolate Monolayers on Gold and Silver. *Journal of Physical Chemistry* **1995,** 99, 7663-7676.

41. Whitesides, G. M.; Laibinis, P. E., Wet Chemical Approaches to the Characterization of Organic-Surfaces - Self-Assembled Monolayers, Wetting, and the Physical Organic-Chemistry of the Solid Liquid Interface. *Langmuir* **1990,** 6, (1), 87-96.

42. Bain, C. D.; Troughton, E. B.; Tao, Y. T.; Evall, J.; Whitesides, G. M.; Nuzzo, R. G., Formation of Monolayer Films by the Spontaneous Assembly of Organic Thiols from Solution onto Gold. *Journal of the American Chemical Society* **1989,** 111, (1), 321-335.

43. Bain, C. D.; Whitesides, G. M., Correlations between Wettability and Structure in Monolayers of Alkanethiols Adsorbed on Gold. *Journal of the American Chemical Society* **1988,** 110, (11), 3665-3666.

44. Bain, C. D.; Whitesides, G. M., Depth Sensitivity of Wetting: Monolayers of Omega-Mercapto Ethers on Gold. *Journal of the American Chemical Society* **1988,** 110, (17), 5897-5898.

45. Bain, C. D.; Whitesides, G. M., Molecular-Level Control over Surface Order in Self-Assembled Monolayer Films of Thiols on Gold. *Science* **1988,** 240, (4848), 62-63.

46. Bain, C. D.; Whitesides, G. M., A Study by Contact-Angle of the Acid-Base Behavior of Monolayers Containing Omega-Mercaptocarboxylic Acids Adsorbed on Gold - an Example of Reactive Spreading. *Langmuir* **1989,** 5, (6), 1370-1378.

47. Young, T., An Essay on the Cohesion of Fluids. *Philosophical Transactions of the Royal Society of London* **1805,** 95, 65-87.

48. Schrader, M. E.; Loeb, G. I., *Modern Approaches to Wettability: Theory and Applications*. Plenum Press: New York.

49. Extrand, C. W., Contact Angles and Their Hysteresis as a Measure of Liquid-Solid Adhesion. *Langmuir* **2004,** 20, (10), 4017-4021.

50.   Israelachvili, J. N.; Gee, M. L., Contact Angles on Chemically Heterogeneous Surfaces. *Langmuir* **1989,** 5, 288-289.

51.   Bard, A. J.; Faulkner, L. R., *Electrochemical Methods: Fundamentals and Applications*. 2nd Edition ed.; John Wiley & Sons, Inc.: 2001; p 832.

52.   Wang, W.; Lee, T.; Reed, M. A., Mechanism of Electron Conduction in Self-Assembled Alkanethiol Monolayer Devices. *Physical Review B* **2003,** 68, (35416), 1-6.

53.   Avila, A.; Gregory, B. W.; Niki, K.; Cotton, T. M., An Electrochemical Approach to Investigate Gated Electron Transfer Using a Physiological Model System: Cytochrome c Immobilized on Carboxylic Acid-Terminated Alkanethiol Self-Assembled Monolayers on Gold Electrodes. *Journal of Physical Chemistry B* **2000,** 104, 2759-2766.

54.   Sathiyanarayanan, S.; Muthukrishnan, S.; Venkatachari, G.; Trivedi, D. C., Corrosion Protection of Steel by Polyaniline (PANI) Pigmented Paint Coating. *Progress in Organic Coatings* **2005,** 53, (4), 297-301.

55.   Selvaraj, M.; Palraj, S.; Jayakrishnan, P., Performance of Polymer Blends on Phosphated Steel Substrate. *Progress in Organic Coatings* **2005,** 54, (1), 1-4.

56.   Affoune, A. M.; Yamada, A.; Umeda, M., Conductivity and Surface Morphology of Nafion Membrane in Water and Alcohol Environments. *Journal of Power Sources* **2005,** 148, 9-17.

57.   Chemia, M.; Dufreche, J. F.; Darolles, I.; Rouelle, F.; Devilliers, D.; Petitdidier, S.; Levy, D., Bias Voltage Dependent Electrochemical Impedance Spectroscopy of p- and n-Type Silicon Substrates. *Electrochimica Acta* **2005,** 51, (4), 665-676.

58.   MacDonald, D. D., Reflections on the History of Electrochemical Impedance Spectroscopy. *Electrochimica Acta* **2006,** 51, (8-9), 1376-1388.

59.   Tompkins, H. G.; McGahan, W. A., *Spectroscopic Ellipsometry and Reflectometry: A User's Guide*. John Wiley & Sons, Inc.: 1999; p 224.

60.   Tompkins, H. G.; Tiwald, T.; Bungay, C., Use of Molecular Vibrations to Analyze Very Thin Films with Infrared Ellipsometry. *Journal of Physical Chemistry B* **2004,** 108, 3777-3780.

61.   Gobets, B.; Stokkum, I. H. M. v.; Mourik, F. v.; Dekker, J. P.; Grondelle, R. v., Excitation Wavelength Dependence of the Fluorescence Kinetics in Photosytem I Particles from *Synechocystis* PCC 6803 and *Synechococcus elongatus*. *Biophysical Journal* **2003,** 85, 3883-3893.

62.   Chamorovsky, C. S.; Chamorovsky, S. K.; Semenov, A. Y., Dielectric and Photoelectric Properties of Photosynthetic Reaction Centers. *Biochemistry (Moscow)* **2005,** 70, (2), 257-263.

63.   Vasil'ev, S.; Orth, P.; Zouni, A.; Owens, T. G.; Bruce, D., Excited-State Dynamics in Photosystem II: Insights from the X-Ray Crystal Structure. *Proceedings of the National Academy of Sciences* **2001,** 98, (15), 8602-8607.

64.   Vasil'ev, S.; Bruce, D., Picosecond Time-Resolved Fluorescence Studies on Excitation Energy Transfer in a Histidine 117 Mutant of the D2 Protein of Photosystem II in Synechocystis 6803. *Biochemistry* **2000,** 39, 14211-14218.

65.   Parson, W. W., Photosynthetic Bacterial Reaction Centers: Interactions Among the Bacteriochlorophylls and Bacteriopheophytins. *Annual Review of Biophysics and Bioenergetics* **1982,** 11, 57-80.

66.   Bard, A. J.; Fan, F. R. F.; Kwak, J.; Lev, O., Scanning Electrochemical Microscopy. Introduction and Principles. *Analytical Chemistry* **1989,** 61, (2), 132-138.

67.   Bard, A. J.; Fan, F. R. F.; Mirkin, M. V., *Scanning Electrochemical Microscopy*. Marcel Dekker, Inc.: New York, 1994.

CHAPTER III

PHOTOSYSTEM I PATTERNING IMAGED BY SCANNING ELECTROCHEMICAL
MICROSCOPY

<u>Introduction</u>

The ability to integrate biological structures with the molecular tools of materials and chemical science is a primary aim of nanobiotechnology. As systems in nature have been optimized through natural selection, a natural photodiode such as Photosystem I (PSI) can be a good candidate for studies towards nano- and molecular electronics. The PSI complex has the ability to generate photoinduced charge separation within picoseconds, a rate that is 100 times faster than that of a silicon diode.[1] Following a biomimetic approach to nanotechnology, PSI could be utilized as an integral component of molecular circuits and energy conversion systems.

Designing molecular or nano-circuits relies on the ability to direct the assembly of individual functional components into desired intricate geometries that permit activity. An important aspect of integrating biomolecules into circuits and sensors[2, 3] is that upon creating patterns, the protein should retain its desired properties (e.g., functionality)[4-6] to enable interfacing with other components. Many proteins will adsorb nonspecifically on a surface and lose biological functionality due to changes in their tertiary and secondary structure. However, photosynthetic proteins have been proven to maintain some functionality and stability after adsorption on a surface.[7] This paper presents the directed assembly of PSI on patterned self-assembled monolayers (SAMs) on gold.

In nature, PSI is found in cyanobacteria as a twelve-unit supramolecular protein complex, while in green plants and algae it has three to four additional subunits, yielding a molecular mass of ~ 300 kDa.[8] The three-dimensional structure of this protein complex was recently revealed providing structural information with atomic detail for the cyanobacterial PSI (12 protein subunits and over 100 cofactors)[9] and for the higher plant PSI (16 protein subunits and almost 200 cofactors).[10] PSI contains a specialized chlorophyll *a* dimer (P700 center) that enables the diode-like behavior upon excitation by photons of light.[11, 12] During photosynthesis a unidirectional transfer of electrons occurs across the thylakoid membrane; the electron transfer vector spans from the P700 center that accepts electrons from plastocyanin to the F_A/F_B centers that donate electrons to ferredoxin.[8] Although not a trivial process, PSI can be successfully isolated from thylakoid membranes of green plants or cyanobacteria while retaining the activity of its redox centers. PSI has been the subject of recent articles[13-15] that examine its electrochemical properties. Reduction-oxidation potentials were identified for P700,[13] iron-sulfur clusters F_A/F_B and phylloquinone A_1.[14] The photocatalytic activity of PSI was also examined in the presence of methyl viologen and cytochrome c_6.[15]

The ability to maintain the activity of PSI electron carriers upon isolation is inherently related to the preservation of its photodiode activity. Greenbaum and co-workers[1, 12, 16, 17] have studied PSI both as an isolated protein and as a part of the thylakoid membrane. They investigated the orientation of PSI on chemically modified surfaces (i.e., SAMs on gold)[12] and used Kelvin force probe microscopy (KFM) to measure exogenous photovoltages generated from single PSI reaction centers on modified gold substrates.[16] They have demonstrated the photocatalytic production of

hydrogen by means of platinized PSI.[1, 17] Their work proves that PSI retains some activity after integration with other materials. Greenbaum and co-workers[12] also found that on a OH-terminated surface, PSI preferentially adsorbs with its electron transfer vector oriented upward. This particular geometry where the P700 end of the protein is in direct contact with the SAM appears favorable for further incorporation in molecular circuits.

Our recent work[18] demonstrates that low-energy surfaces (e.g., CH_3-terminated ω-alkanethiols) greatly inhibit the adsorption of PSI (stabilized by Triton X-100 in phosphate buffer pH 7), whereas high-energy surfaces (e.g., OH-terminated ω-alkanethiols) enable PSI adsorption. We have reasoned that the non-adsorption of PSI at low-energy surfaces is due to an adsorbed layer of Triton X-100 that orients to produce a protein-resistant poly(ethylene glycol) surface. This selectivity in adsorption suggests that PSI patterning could be achieved through a combination of microcontact printing and alkanethiol assembly in order to obtain discrete regions of 'opposing' chemical functionality where PSI will exhibit differences in adsorption. Figure 3.1 displays a schematic of this idea: (a) a low-energy SAM that will not allow PSI adsorption is microcontact printed onto a Au surface; (b) this pattern is then backfilled with a high-energy SAM that will not only allow the PSI adsorption, but will also orient the protein into a favorable configuration for further incorporation in electronics; (c) the protein adsorbs selectively on the chemically modified Au surface, yielding a PSI pattern.

Recent methods for patterning proteins include lithography and stamping techniques, ranging from thermo-biolithography[19] to microcontact printing of proteins
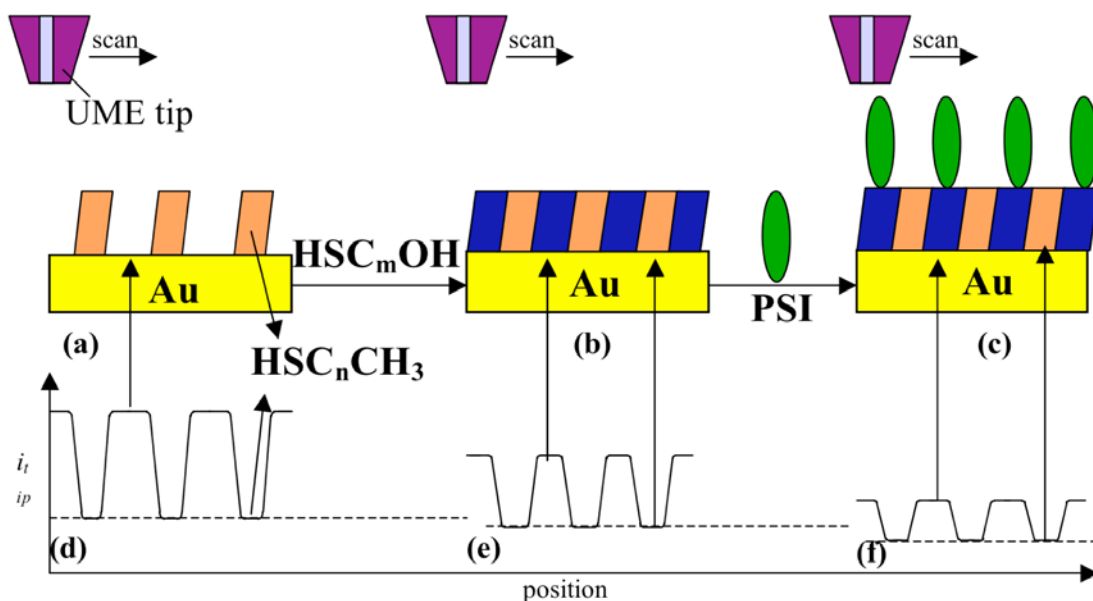
Figure 3.1. Schematic of PSI patterning: (a) microcontact printed SAM (*e.g.*, CH$_3$-terminated ω-alkanethiol) on evaporated Au; (b) patterned SAM backfilled with OH-terminated ω-alkanethiol; (c) patterned PSI on a chemically modified Au surface. Current-position profiles as the UME tip scans horizontally across the patterned surface (d) – (f).

onto surfaces by direct stamping.[20-24] Perhaps the most convenient approach is to pattern

a SAM that can direct the adsorption of proteins on the basis of chemical affinity.[25-27]

Bhatia et al.[25] have modified organosilane SAMs by deep ultraviolet irradiation to direct

IgG adsorption. Whitesides et al.[26, 27] have used various techniques (e.g.,

micromachining, optical lithography, microcontact printing) to create patterned surfaces

where proteins exhibit adsorption differences (micrometer-scale islands of alternating

hydrophobic and oligo(ethylene glycol)-terminated SAMs). The protein assembled on

the hydrophobic regions only, since the SAMs terminated in oligo(ethylene glycol)

groups resist the adsorption of proteins.[26] As shown in Figure 3.1, our approach also

utilizes microcontact printing[28-31] to prepare a patterned surface that directs the

adsorption of a protein complex (PSI) onto a surface. However, an important advantage of our approach is that commercially available methyl- and hydroxyl-terminated thiols are used to direct protein adsorption without the need for extensive synthesis of oligo(ethylene glycol) terminated thiols. Our approach relies on the presence of the PSI-stabilizing surfactant Triton X-100, which adsorbs from solution onto low-energy (CH$_3$-terminated) regions to create a poly(ethylene glycol)-rich surface[18] that locally prevents PSI adsorption.

Chemical modification of surfaces and protein adsorption represent processes that modify the conductivity of substrates, making scanning electrochemical microscopy (SECM) an appropriate method for the investigation of PSI patterning. SECM is an electrochemical technique involving a four-electrode system (Figure 3.2), as opposed to the more common three-electrode electrochemical cells. SECM involves a reference electrode (RE), a counter electrode (CE), and two working electrodes (WEs): (i) a conductive substrate electrode (SE) and (ii) a tip (probe) electrode which is in all cases an ultramicroelectrode (UME, diameter < 25 μm). SECM is an in situ scanning probe microscopy that rasters a UME tip across the surface, measuring electrochemical gradients.[32] Reversible electrochemical mediators, like ferrocenes, diffuse away from the substrate electrode and are collected electrochemically at the tip. Rastering the tip across the surface enables the mapping of conductivity and permeability of an electrode surface. Recording approach curves (ACs) to different points on a surface can also give information about conductivity differences. Usually the ACs are plotted as the normalized current (I_T = approach current i_{tip}/steady-state current i_{ss}) vs. the distance, d, between the UME and the substrate. The expression for i_{ss} is given by:

$$i_{ss} = 4nFDCa \qquad (3\text{-}1)$$

where n is the number of electrons, F is the Faraday constant, D and C are the diffusion coefficient and the concentration for the electrochemically active species respectively, and a is the radius of the UME.[32]   The UME can travel vertically, as in the case of recording ACs, or horizontally, as in the case of imaging. For the case of a conductive substrate and a perfectly reversible redox couple, the potentials (E_{tip} and E_{SE}) would be set such that the mediator would undergo oxidation at one of the electrodes and reduction at the other one (e.g., oxidation at the UME and reduction at the SE). When the UME is far from the substrate (> tens of microns) i_{ss} reaches a constant value that is limited by the diffusion of the redox species to the disk-shaped UME. When the distance between the two electrodes is within a few microns a positive feed-back loop is created, wherein the oxidized mediator (Ox) produced at the tip will quickly diffuse to the SE, where it will undergo the reduction reaction, and the reduced species (Red) will diffuse back to the UME (Figure 3.2). As the distance between electrodes decreases, this electrochemical cycling will increase, and the tip current will exhibit a sharp increase and hence provide a positive feed-back signal, with a few hundred percent increase for a final approach of the UME to within a few microns of the SE. For the case of an insulating substrate, as the two electrodes approach within microns, the tip current will decrease as the proximity of the two electrodes blocks diffusion to the tip, providing a negative feed-back signal. A positive feedback approach current is considered maximum (I_{Tmax}) right before the tip contacts the substrate. A more conductive surface will result in a larger maximum approach current, and this maximum can typically approach 800% of i_{ss} on purely

conductive surfaces (I_T = 8). ACs to a completely insulating surface will present only I_T values < 1 with the current decreasing continuously as the tip approaches the substrate surface. When the tip travels horizontally, as in the case of SECM imaging, the output of the instrument is a current-position profile for the surface scanned. Figure 3.1d-f depicts a schematic of how such profiles would appear for patterned surfaces. An SECM image is a collection of current-position profiles.
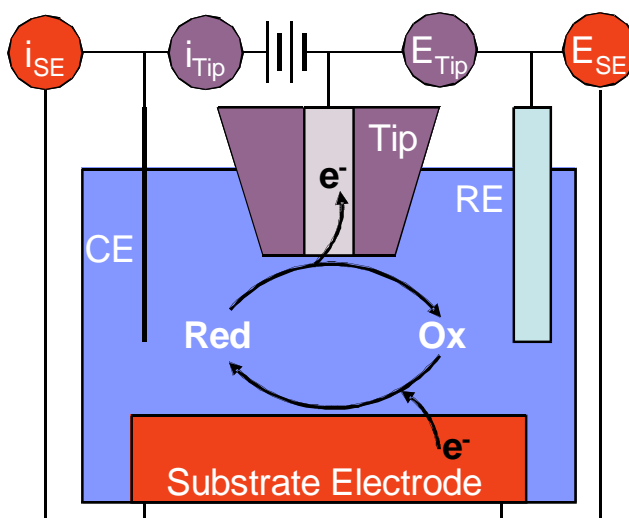
Figure 3.2. SECM working principle, for a conductive substrate electrode (SE): reduced species (Red) oxidized at the tip yield oxidized species (Ox); when the regeneration of Red occurs at the SE, positive feedback is observed in the form of current increase.

SECM has been previously used for the study of microcontact printed surfaces, providing important information regarding density and uniformity of adsorption, as well as images of patterns where differences in conductivity are highlighted. Wilhelm and Wittstock[33] have used the SECM for the study of enzyme patterns on microcontact printed SAMs. They obtained images with good resolution when using longer chained

thiols (C_{16}-C_{20}), but for chain lengths under C_{12}, the resolution was very poor and the patterns could not be distinguished. They have also used SECM for local electrochemical desorption of SAMs to pattern and study functional proteins.[34] Additionally, Matsue et al.[24] have used PDMS stamps to pattern fibronectin on glass substrates in order to promote cell growth, and they employed SECM to study the respiration of patterned HeLa cells.

This chapter will address patterning methods for PSI to enable future prototype microscale devices containing nanoscale components. By utilizing the unique adsorption characteristics of PSI on chemically modified substrates, we generate patterns through bottom-up assembly using the simplistic and inexpensive technique of microcontact printing. Since alternating regions on the patterned surfaces present different conductivities, we utilize SECM approach curves and imaging to assess the formation of PSI patterns on a substrate.

Scanning Electrochemical Microscopy

SECM measurements were conducted with a CHI900 instrument from CH Instruments equipped with an adjustable stage for tilt correction. The electrochemical cell was in a typical four-electrode configuration: UME tip electrode, Pt wire counter electrode, Ag/AgCl, 3 M KCl reference electrode (CHI111), and substrate electrode, which was either a 2 mm Pt disk (CHI303) for UME testing, or evaporated Au for imaging. All UMEs were manufactured with 5 μm Pt wire from Goodfellow according to Bard et al.,[32] polished with 0.05 μm alumina from Buehler, and sonicated in ethanol and water. The actual measured radius for the UMEs was a = 3.5 μm (see Equation 1).

UMEs were electrochemically cleaned for 5 min in 0.5 M H_2SO_4 using a CHI660a potentiostat, and were tested with 1 mM FcTMA in 100 mM KCl for performance. The Pt SE was polished and cleaned in an identical manner to the UMEs. The SECM images were considered valid if the UME approached before and after imaging a Pt SE at $I_T = 8$. This was done to ensure that no significant electrode fouling took place during the experiments. The UMEs were also characterized by cyclic voltammetry (CV), and consistently yielded the expected sigmoidal CV. For imaging on evaporated Au substrates the mediator was 1 mM FcTMA in 200 mM pH 7 phosphate buffer with 1 mM Triton X-100. For imaging on Au IDAs, the mediator was 1 mM FcTMA in 100 mM KCl. All PSI imaging was conducted in the dark at room temperature.

I_{Tmax} values were recorded in Table 3.1 for patterns to demonstrate backfilling. The I_{Tmax} values refer to the specific images presented in this chapter. On each studied surface we investigated at least three distinct points for each pattern component (e.g., for Figure 3.5a we have taken into account three approach curves to the Au regions, and three approach curves to the C_{12} regions); more commonly, four or five different values were averaged, and the data are presented with the corresponding standard deviation.

All SECM images were acquired in the constant height mode. The ACs served as means of positioning the tip close to the surface before acquiring an SECM image. For example, when approaching a 7.0 μm tip to a perfectly conductive surface in the presence of a reversible electrochemical mediator, for an approach current $I_T = 2.0$, the tip is at d = 2.2 μm from the SE. Distances within a few microns will yield good resolution images. For the cases when the I_{Tmax} values were determined, the tip to SE distance, d, could be estimated. Since each pattern has two types of surfaces, the specific region approached

must be identified before recoding each image. For example, in the case when we approached to Au before imaging at a current value $I_T = 2$, knowing that $I_{Tmax} = 4.2$, we used the approach curve for which I_{Tmax} was found to measure the distance between the 0 μm the point and the point corresponding to $I_T = 2$, and found d = 1.38 μm.

For all SECM images presented in this paper, we have the following common experimental parameters: a = 3.5 μm; RG = 5 ± 0.5; E_{tip} = + 0.65 V, E_{SE} = 0 V, vs. Ag/AgCl, 3 M KCl; imaging scan rate: 30 μm/s; the concentration of FcTMA was approximately 1 mM; for each image the i_{ss} value is provided in the figure caption, and the exact concentration of the mediator can be easily calculated using Equation 1, since all other parameters are known.

Results and Discussion

PSI adsorption on chemically modified Au surfaces was investigated with SECM. The first substrate studied was a Au IDA in which Au lines are interdigitated on an insulating glass substrate. Au IDAs allow for a good control between completely conductive and insulating regions to provide model substrates for SECM studies. Sets of ACs were recorded with each modification of the IDA. Figure 3.3a displays the SECM image and AC of a Au IDA after electrochemical cleaning, using a Pt tip and FcTMA as mediator. The image was recorded after approaching at I_T =2 to the Au; the shape of the AC is consistent with a conductive Au surface. After assembly of the $HOC_{11}S$-monolayer on Au, highly conductive feedback was no longer observed at any point on the IDA, as the AC indicates only partial conductivity (Figure 3.3b). Generally, any I_T value above unity indicates some positive feedback from a conductive substrate. The

corresponding image from Figure 3.3b presents a lower overall current with a smaller difference between the SAM (higher current values) and the glass (lower current values): 435 pA (3.3b) vs. 1.59 nA (3.3a). In comparison to Figure 3.3b, overnight PSI adsorption (Figure 3.3c) demonstrates a more dramatic loss in current and contrast (only 96 pA) relative to the previous image (Figure 3.3b), owing to the presence of the protein layer. At this point all ACs have the characteristic trend of an insulating surface (Figure 3.3c) due to the adsorbed PSI. Although the entire surface appears insulating, the glass still exhibits the lowest current since the incomplete coverage of PSI allows some mediator Faradaic current through the exposed SAM. We were not able to fit the recorded ACs to the existing theoretical ACs, since in our case the substrate is patterned, causing mixed positive and negative feedback interference from the adjacent pattern lines. The approach curve fitting theories have been developed only for uniform substrates (i.e., non-patterned).

We note that the images presented in Figure 3.3 are for the same Au IDA. Although we have not defined the zero point for the ACs in Figure 3.3, we were able to compare the images with respect to their current and contrast. The SECM mode that we use for imaging is the constant height mode. The 'constant height' is set approaching the substrate to a certain feedback current level. For Figures 3.3b and 3.3c, for example, we have used the same approach current level ($I_T = 0.94$) for positioning the tip before acquiring the images. In order to be able to compare the feedback levels, we have approached to same type of region on the IDA, i.e., the high-current region corresponding to the modified Au digits. Thus, if there is no difference in the patterns, the images should look identical; this is not the case for 3.3b and 3.3c. We observe that for the same

feedback level in positioning the tip near the substrate, Figure 3.3c corresponds to a substrate that is more insulating overall.
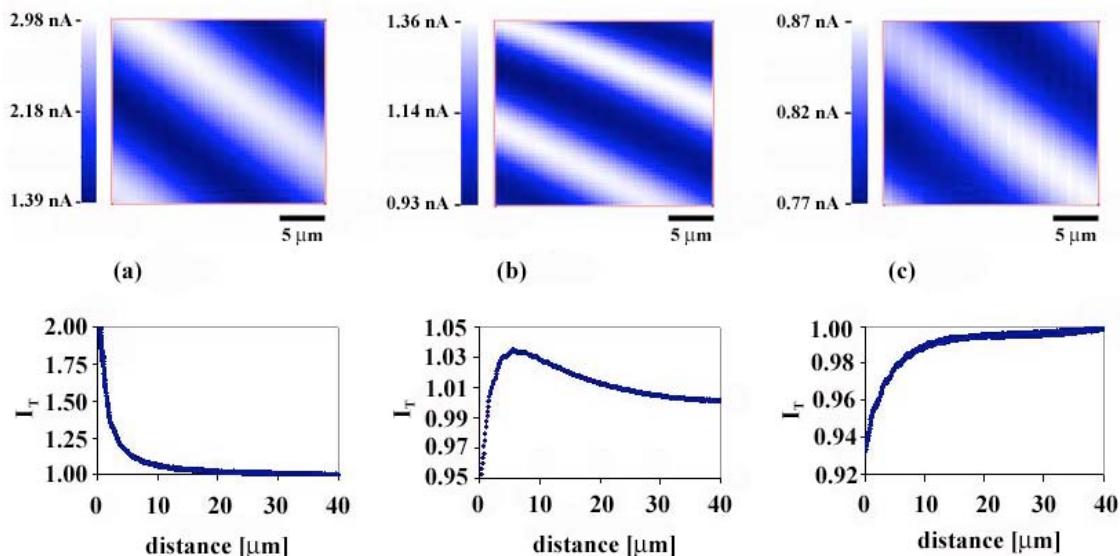
Figure 3.3. SECM images of Au IDAs using FcTMA and a 7 μm Pt tip: (a) Au IDA image with corresponding AC to the Au digit; i_{ss} = 0.94 nA; tip positioned by AC to Au, I_T = 2; (b) IDA with SAM on Au digits, and corresponding AC to the Au-SC$_{11}$OH region; i_{ss} = 1.07 nA; tip positioned by AC to C$_{11}$OH, I_T = 0.94; (c) image of adsorbed PSI on a high energy surface, HSC$_{11}$OH, and the corresponding AC to the PSI region; i_{ss} = 0.93 nA; tip positioned by AC to PSI, I_T = 0.94. On all images the lowest current corresponds to the glass part from the IDAs. Images were obtained by Dr. Ciobanu.

We obtained similar results to the ones presented in Figure 3.3 for a different redox mediator, hexaammineruthenium(III) chloride (E_{tip} = - 0.35 V, E_{SE} = 0 V, vs. Ag/AgCl, 3 M KCl), while degassing the solution. Since the SECM studies appeared independent of the type of redox mediator, we chose FcTMA for all the other experiments.

We have also used SECM to image the directed adsorption of PSI at surfaces containing discrete regions of CH_3- and HO-terminated SAMs on Au created by microcontact printing and subsequent backfilling. The patterned SAMs on Au were investigated by SECM immediately after each step of stamping, backfilling with a different SAM, and PSI adsorption. No ACs are shown for this study since they all have the indicative trend for a conductive substrate; I_{Tmax} values are given instead. SECM imaging of stamped short-chained ω-alkanethiolate SAMs (e.g., Au/SC_6OH) does not yield distinguishable differences between the Au and the SAM due to the insufficient insulating capacity of the thin SAM. Complimentary experiments indicate no preferential rate of etching between Au and this type of SAM. This is a consequence of inefficient packing of short-chained ω-alkanethiols that results from their decreased van der Waals interactions between adjacent hydrocarbon chains (disorganized SAMs appear less insulating). Longer-chained SAMs prepared from $HSC_{11}OH$ or $HSC_{11}CH_3$ result in SECM images indicative of successful patterning (in accordance with results from etching experiments). The CH_3-terminated SAMs are more insulating than the OH-terminated SAMs because the alkyl-terminated thiols form more organized SAM blocking layers. Figure 3.4a displays the SECM image of a 10 μm line pattern from $HSC_{11}OH$ with 20 μm spacings of Au, where a lower current is observed for the insulating SAM. Upon backfilling this particular pattern with $HSC_{11}CH_3$, the 20 μm lines now become more insulating than the 10 μm lines ($HSC_{11}OH$), indicating that the hydrophobic monolayer impedes the flow of electrochemical mediator current at the substrate to a greater extent than a hydrophilic monolayer of the same overall chain length (Figure 3.4b). Exposing this backfilled pattern to a PSI solution results in the

selective adsorption of the protein onto the hydroxyl regions, which causes reduced

currents and loss of image contrast in Figure 3.4c. The thickness of the insulating protein

layer blocks the electron transfer, thereby reducing the electrochemical current

significantly.
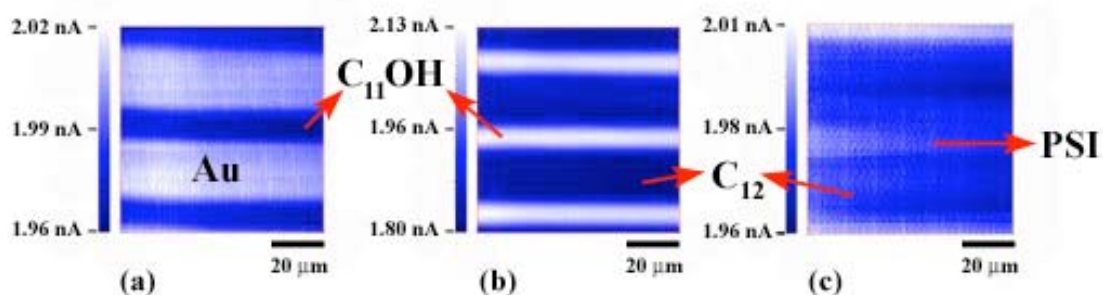
Figure 3.4. SECM images of microcontact patterned gold using FcTMA as mediator with a 7 μm Pt tip: (a) 10 μm $HSC_{11}OH$ with 20 μm Au lines; i_{ss} = 1.02 nA; tip positioned by AC to $C_{11}OH$, I_T = 2; (b) 10 μm $HSC_{11}OH$ backfilled with 20 μm $HSC_{11}CH_3$ lines i_{ss} = 0.98 nA; tip positioned by AC to C_{12}, I_T = 1.75; (c) 10 μm PSI lines (adsorbed onto $HSC_{11}OH$) spaced by 20 μm $HSC_{11}CH_3$ lines; i_{ss} = 0.99 nA; tip positioned by AC to PSI, I_T = 2. Substrates were patterned by Helen Kincaid and imaged by Dr. Ciobanu.

When comparing two images taken in similar conditions, we must know the

relative position of the tip with respect to the substrate. For the case presented in Figure

3.4, regardless of the tip to substrate distance, d, we can easily assess that the backfilling

occurred, since the Au-$SC_{11}OH$ regions went from low-current (Figure 3.4a) to high

current (Figure 3.4b). The tip positioning in the proximity of the substrate was done by

ACs: for Figure 3.4a we approached on the Au-$SC_{11}OH$ region to a current value I_T = 2,

while for Figure 3.4b we approached on the Au-$SC_{11}CH_3$ region to a current value I_T =

1.75. For the same value for I_T, if we compare a perfectly conductive substrate with a

SAM-modified substrate, the tip will be closer to the substrate in the case of the modified SE. A comparison between the images in Figures 3.4b and 3.4c is relevant only if the tip was at least as close to the SE in 3.4c as it was in 3.4b. Since in 3.4b the approach current before imaging was at $I_T = 1.75$, the tip was at least as close to the SE in 3.4c since it was positioned through an $I_T = 2$ (we estimate that the tip was actually closer to the SE in 3.4c than in 3.4b).

Since the monolayers assembled from solutions have different electrochemical properties than the SAMs obtained through microcontact printing,[35] we investigated the effect of the stamping/backfilling order on the properties of the pattern and on the protein adsorption. Initial patterning with $HSC_{11}CH_3$ yields 20 μm lines of insulating SAM and 10 μm lines of Au (Figure 3.5a), while the backfilling of this surface with $HSC_{11}OH$ is displayed in Figure 3.5b. In both Figure 3.5a and 3.5b, the lower current corresponds to the low-energy surface. Approaching to points at various locations on the patterned surface demonstrates successful backfilling. On the initial pattern (Figure 3.5a), the tip was able to approach at a maximum current $I_{Tmax} = 4.2$ on the 10 μm Au lines. Table 3.1 presents I_{Tmax} values for the patterns presented in Figures 3.5 and 3.6, and it specifies for which pattern region the AC was recorded. Although Au is a conductive surface, the current cannot reach higher values due to diffusional hindrance of the electrochemical mediator caused by the tip size (the 7 μm Pt wire is insulated in glass, and the entire diameter of the tip is ~ 35 μm) and the adjacent SAM lines; the shape of the normal diffusional plume at the UME is altered by the presence of the SAM lines that border the Au region on two sides. On the backfilled pattern (Figure 3.5b), the low-energy surface decreases the I_{Tmax} value from 3.2 to 2.2, due to the fact that the 10 μm gaps are now

filled with a SAM that is inherently less conductive than Au. The ACs to these 10 μm HOC$_{11}$S- lines give a much lower overall current (I_{Tmax} = 3.1) than that reported in Figure 3.5a. The values of the approach currents for each type of surface in each individual pattern prove that the backfilling of an ω-alkanethiol with a different terminal group was successfully achieved.
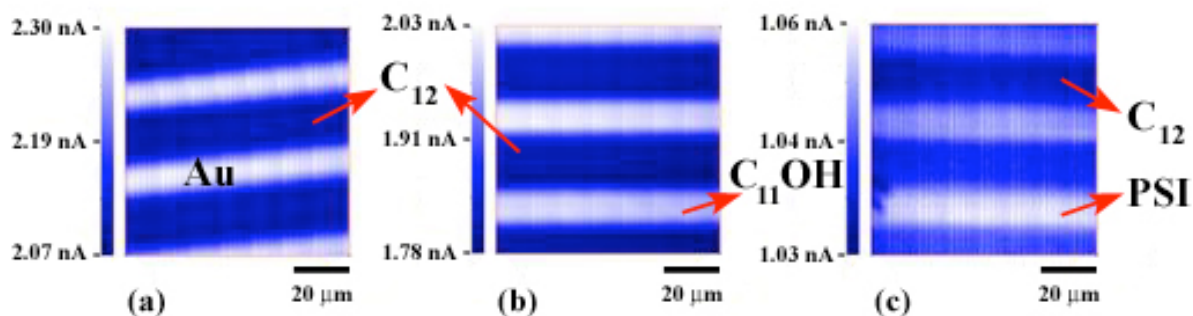
Figure 3.5. SECM images of microcontact patterned gold using FcTMA as mediator with a 7 μm Pt tip: (a) 20 μm HSC$_{11}$CH$_3$ was patterned initially, with 10 μm Au line gaps; i_{ss} = 1.07 nA; d = 1.38 μm; tip positioned by AC to Au, I_T = 2; (b) 20 μm HSC$_{11}$CH$_3$ backfilled with 10 μm HSC$_{11}$OH lines; i_{ss} = 1.11 nA; d = 0.92 μm; tip positioned by AC to C$_{11}$OH, I_T = 2. The current is lower in both cases for the CH$_3$-terminated SAM, but the maximum approach current (lower in (b)) indicates that backfilling was successful; (c) 10 μm PSI lines (adsorbed onto HSC$_{11}$OH) spaced by 20 μm HSC$_{11}$CH$_3$ lines; i_{ss} = 0.85 nA; d = 0.41 μm; tip positioned by AC to Au, I_T = 1.4. The overall lower current indicates successful PSI adsorption. Substrates were patterned by Helen Kincaid and imaged by Dr. Ciobanu.

The backfilled pattern of Figure 3.5b was used to study the PSI adsorption and the resulting image is presented in Figure 3.5c. ACs are recorded in different locations, and the maximum value reached anywhere on the surface was I_{Tmax} = 1.5, demonstrating that the surface becomes more insulating in its entirety upon PSI adsorption. Since PSI does not cover the OH-terminated surface completely,[12] some electrochemical mediator

current is still observed, rendering the OH-terminated surface slightly more electrochemically-active than the CH$_3$-terminated surface. Once the PSI is adsorbed, the image contrast decreases from 250 pA for the backfilled pattern to 30 pA for the patterned PSI. The image in Figure 3.5c, although it still displays the lowest current for HSC$_{11}$CH$_3$, does have PSI adsorbed on the surface. It is important to notice that with each image presented in Figure 3.5 we had to bring the tip closer to the substrate, in order to be able to distinguish the pattern: d is 1.38 μm for 3.5a, 1.11 μm for 3.5b, and 0.41 μm for 3.5c. After imaging, each piece of patterned Au was subjected to RAIRS analysis, and in every case the characteristic amide bands[18] (not shown) were detected, indicating definite PSI adsorption on the patterned surface. Our previous work has shown that PSI adsorbs only on high energy surfaces (e.g., hydroxyl-terminated), but not on low energy surfaces (e.g., methyl-terminated) in the presence of Triton X-100.[18]

Table 3.1. I_T maximum values for different patterned surfaces.

Au surface stamped with C$_{12}$	I_{Tmax} for approach curves to:					
& backfilled with C$_{11}$OH (Fig. 5)	(a) - Au	(a) - C$_{12}$	(b) - C$_{11}$OH	(b) - C$_{12}$	(c) - PSI	(c) - C$_{12}$
	4.2 ± 0.1	3.2 ± 0.4	3.1 ± 0.2	2.2 ± 0.4	1.45 ± 0.03	1.47 ± 0.04
& backfilled with C$_6$OH (Fig. 6)	(a) - C$_6$OH	(a) - C$_{12}$	(b) - PSI	(b) - C$_{12}$	N/A	
	2.0 ± 0.1	1.6 ± 0.1	2.4 ± 0.1	2.0 ± 0.2		

PSI adsorption on a HOC$_{11}$S- pattern backfilled with HSC$_{11}$CH$_3$ (Figure 3.4c) contrasts that on a CH$_3$C$_{11}$S- pattern backfilled with HSC$_{11}$OH (Figure 3.4c). As the patterning and the backfilling order influences the conductivity of the pattern, the adsorption of PSI is expected to be influenced as well. Losic et al.[35] have shown that a

stamped SAM and a solution-formed SAM differ in their electrochemical behavior; a stamped monolayer is less organized, resulting in a more conductive surface. The hydroxyl-terminated SAM is more insulating when it is assembled (Figure 3.5) than when it is stamped (Figure 3.4). This difference is consistent with more PSI adsorption onto the stamped, inferior SAM (Figure 3.4c). Figure 3.5c displays improved resolution (as compared with Figure 3.4c), suggesting a reduced coverage of PSI that allows more current.

Since the ultimate goal of this research is the implementation of PSI in nano-circuits, we also investigated whether PSI adsorption can be directed on short-chained SAMs, where the protein would be closer to the conductive Au, providing less resistance to electron transfer. Figure 3.6a shows an SECM image of a surface after stamping with $HSC_{11}CH_3$ and backfilling with HSC_6OH, which is similar to that observed when backfilling with $HSC_{11}OH$. Although the ACs recorded for the backfilled pattern (Figure 3.6a) and for the patterned protein (Figure 3.6b) do not exhibit notable differences, the reduced contrast (110 pA (6a) to 40 pA (6b)) indicates that the PSI adsorption lowers the overall current. Since PSI adsorption reduces mediator currents, to achieve the reduced contrast in Figure 3.6b we had to bring the tip half a micron closer to the SE than for the image displayed in Figure 3.6a.

When SECM is used to characterize the directed adsorption of PSI at patterned surfaces, the electrochemical surface image provides information about the uniformity of adsorption. Since the PSI regions in most of the presented images appear uniform and the current is significantly reduced, we infer that the protein layers are uniformly adsorbed (across the scale of microns) and densely packed (on the scale of nanometers)

on the hydroxyl surfaces. In Figure 3.6a, the bottom Au/SC$_6$OH line is not uniform, indicating that the SAM is probably not packed to the same extent across the imaged region. However, Figure 3.6b displays uniform current bands for PSI, which along with the dramatic loss in conductivity, suggest a densely packed protein layer. These densely packed layers are confirmed in all images by large changes in current and contrast.
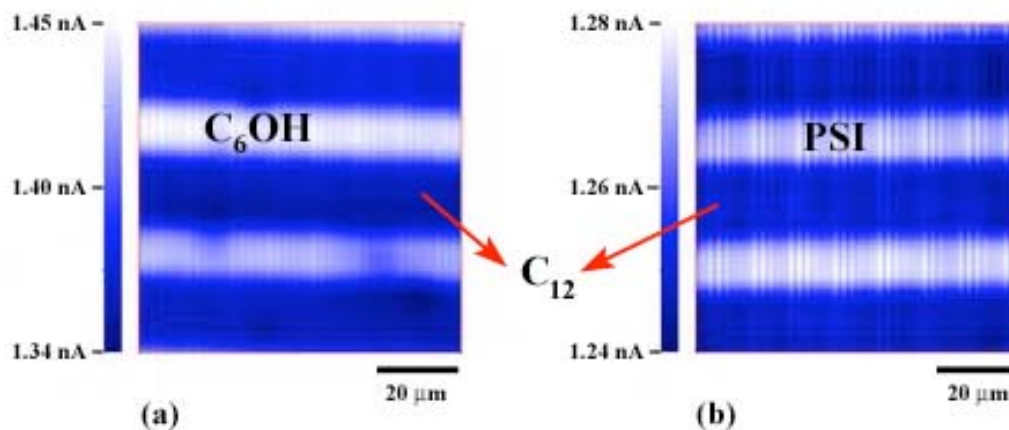
Figure 3.6. SECM images of SAM-modified Au and patterned PSI using FcTMA and a 7 μm Pt tip: (a) 20 μm HSC$_{11}$CH$_3$ backfilled with 10 μm HSC$_6$OH lines; i_{ss} = 0.89 nA; d = 1.05 μm; tip positioned by AC to C$_{12}$, I_T = 1.5; (b) 10 μm PSI lines (adsorbed onto HSC$_6$OH) spaced by 20 μm HSC$_{11}$CH$_3$ lines; i_{ss} = 0.82 nA; d = 0.51 μm; tip positioned by AC to C$_{12}$, I_T = 1.5. The maximum approach current I_{Tmax} is similar in both cases, but the lower current in (b) indicates the presence of PSI. Substrates were patterned by Helen Kincaid and imaged by Dr. Ciobanu.

Conclusions

We report the first directed assembly of PSI on model surfaces prepared through microcontact printing and its characterization by SECM. Patterning of SAMs enables the creation of discrete regions of chemical functionality on Au surfaces for selective adsorption of PSI. SECM is employed for electrochemical imaging of patterned surfaces because it can detect changes in the conductivity of a surface upon the formation of

SAMs on evaporated Au, as well as the changes in the conductivity upon backfilling of the initial pattern and adsorption of PSI.

References

1.   Lee, J. W.; Collins, R. T.; Greenbaum, E., Molecular Ionic Probes: A New Class of Hill Reagents and Their Potential for Nanofabrication and Biometallocatalysis. *J. Phys. Chem. B* **1998,** 102(11), 2095-2100.

2.   Nakamura, H.; Karube, I., Current Research Activity in Biosensors. *Anal. Bioanal. Chem.* **2003,** 377, 446-468.

3.   Scouten, W. H.; Luong, J. H. T.; Brown, R. S., Enzyme or Protein Immobilization Techniques for Applications in Biosensor Design. *Trends in Biotechnology* **1995,** 13, 178-185.

4.   Wadu-Mesthrige, K.; Amro, N. A.; Garno, J. C.; Xu, S.; Liu, G. Y., Fabrication of Nanometer-Sized Protein Patterns Using Atomic Force Microscopy and Selective Immobilization. *Biophys. J.* **2001,** 80, 1891-1899.

5.   Sortino, S.; Petralia, S.; Condorelli, G. G.; Conoci, S.; Condorelli, G., Novel Photoactive Self-Assembled Monolayer for Immobilization and Cleavage of DNA. *Langmuir* **2003,** 19, 536-539.

6.   Nicolini, C., Protein-Monolayer Engineering: Principles and Application to Biocatalysis. *Trends in Biotechnology* **1997,** 15, 395-401.

7.   Wilson, M.; Kannangara, K.; Smith, G.; Simmons, M.; Raguse, B., *Nanotechnology: Basic Science and Emerging Technologies*. CRC Press LLC: 2002.

8.   Chitnis, P. R., Photosystem I: Function and Physiology. *Ann. Rev. Plant Physiol. Plant Mol. Biol.* **2001,** 52, 593-626.

9.   Jordan, P.; Fromme, P.; Witt, H. T.; Klukas, O.; Seanger, W.; Krauss, N., Three-Dimensional Structure of Cyanobacterial Photosystem I at 2.5 Å Resolution. *Nature* **2001,** 411(6840), 909-917.

10.   Ben-Shem, A.; Frolow, F.; Nelson, N., Crystal Structure of Plant Photosystem I. *Nature* **2003,** 426, 630-635.

11.   He, W. Z.; Malkin, R., Photosystems I and II. In *Photosynthesis*, 1998; pp 29-43.

12. Lee, I.; Lee, J. W.; Greenbaum, E., Biomolecular Electronics: Vectorial Arrays of Photosynthetic Reaction Centers. *Phys. Rev. Lett.* **1997,** 79(17), 3294-3297.

13. Kievit, O.; Brudvig, G. W., Direct Electrochemistry of Photosystem I. *J. Electroanal. Chem.* **2001,** 497(1-2), 139-149.

14. Munge, B.; Das, S. K.; Ilagan, R.; Pendon, Z.; Yang, J.; Frank, H. A.; Rusling, J. F., Electron Transfer Reactions of Redox Cofactors in Spinach Photosystem I Reaction Center Protein in Lipid Films on Electrodes. *J. Am. Chem. Soc.* **2003,** 125(41), 12457-12463.

15. Proux-Delrouyre, V.; Demaille, C.; Leibl, W.; Setif, P.; Bottin, H.; Bourdillon, C., Electrocatalytic Investigation of Light-Induced Electron Transfer between Cytochrome c6 and Photosystem I. *J. Am. Chem. Soc.* **2003,** 125(45), 13686-13692.

16. Lee, I.; Lee, J. W.; Stubna, A.; Greenbaum, E., Measurement of Electrostatic Potentials above Oriented Single Photosynthetic Reaction Centers. *J. Phys. Chem. B* **2000,** 104(11), 2439-2443.

17. Millsaps, J. F.; Bruce, B. D.; Lee, J. W.; Greenbaum, E., Nanoscale Photosynthesis: Photocatalytic Production of Hydrogen by Platinized Photosystem I Reaction Centers. *Photochem. Photobiol.* **2001,** 73(6), 630-635.

18. Ko, B. S.; Babcock, B.; Jennings, G. K.; Tilden, S. G.; Peterson, R. R.; Cliffel, D. E.; Greenbaum, E., Effect of Surface Composition on the Adsorption of Photosystem I onto Alkanethiolate Self-Assembled Monolayers on Gold. *Langmuir* **2004,** 20(10), 4033-4038.

19. Fernandes, R.; Yi, H.; Wu, L.-Q.; Rubloff, G. W.; Ghodssi, R.; Bentley, W. E.; Payne, G. F., Thermo-biolithography: A Technique for Patterning Nucleic Acids and Proteins. *Langmuir* **2004,** 20(3), 906-913.

20. Specht, C. G.; Williams, O. A.; Jackman, R. B.; Schoepfer, R., Ordered Growth of Neurons on Diamond. *Biomaterials* **2004,** 25(18), 4073-4078.

21. Bernard, A.; Delamarche, E.; Schmid, H.; Michel, B.; Bosshard, H. R.; Biebuyck, H., Printing Patterns of Proteins. *Langmuir* **1998,** 14, 2225-2229.

22. Bernard, A.; Renault, J. P.; Michel, B.; Bosshard, H. R.; Delamarche, E., Microcontact Printing of Proteins. *Advanced Materials* **2000,** 12, 1067-1070.

23. Tan, J. L.; Tien, J.; Chen, C. S., Microcontact Printing of Proteins on Mixed Self-Assembled Monolayers. *Langmuir* **2002,** 18, 519-523.

24. Nishizawa, M.; Takoh, K.; Matsue, T., Micropatterning of HeLa Cells on Glass Substrates and Evaluation of Respiratory Activity Using Microelectrodes. *Langmuir* **2002,** 18(9), 3645-3649.

25. Bhatia, S. K.; Teixeira, J. L.; Anderson, M.; Shriver-Lake, L. C.; Calvert, J. M.; Georger, J. H.; Hickman, J. J.; Dulcey, C. S.; Schoen, P. E.; Ligler, F. S., Fabrication of Surfaces Resistant to Protein Adsorption and Application to Two-Dimensional Protein Patterning. *Analytical Biochemistry* **1993,** 208(1), 197-205.

26. Lopez, G. P.; Biebuyck, H. A.; Harter, R.; Kumar, A.; Whitesides, G. M., Fabrication and Imaging of Two-Dimensional Patterns of Proteins Adsorbed on Self-Assembled Monolayers by Scanning Electron Microscopy. *J. Am. Chem. Soc.* **1993,** 115(23), 10774-10781.

27. Mrksich, M.; Chen, C. S.; Xia, Y.; Dike, L. E.; Ingber, D. E.; Whitesides, G. M., Controlling Cell Attachment on Contoured Surfaces with Self-Assembled Monolayers of Alkanethiolates on Gold. *PNAS* **1996,** 93(20), 10775-10778.

28. Tien, J.; Xia, Y.; Whitesides, G. M., *Microcontact Printing of SAMs*. Academic: Boston, 1998; Vol. 24.

29. Kumar, A.; Biebuyck, H. A.; Whitesides, G. M., Patterning Self-Assembled Monolayers: Applications in Materials Science. *Langmuir* **1994,** 10(5), 1498-1511.

30. Odom, T. W.; Love, J. C.; Wolfe, D. B.; Paul, K. E.; Whitesides, G. M., Improved Pattern Transfer in Soft Lithography Using Composite Stamps. *Langmuir* **2002,** 18, 5314-5320.

31. Xia, Y.; Rogers, J. A.; Paul, K. E.; Whitesides, G. M., Unconventional Methods for Fabricating and Patterning Nanostructures. *Chem. Rev.* **1999,** 99, 1823-1848.

32. Bard, A. J.; Fan, F. R. F.; Mirkin, M. V., *Scanning Electrochemical Microscopy*. Marcel Dekker, Inc.: New York, 1994; Vol. 18, p 243-373.

33. Wilhelm, T.; Wittstock, G., Generation of Periodic Enzyme Patterns by Soft Lithography and Activity Imaging by Scanning Electrochemical Microscopy. *Langmuir* **2002,** 18(24), 9485-9493.

34. Wilhelm, T.; Wittstock, G., Patterns of Functional Proteins Formed by Local Electrochemical Desorption of Self-Assembled Monolayers. *Electrochim. Acta* **2001,** 47(1-2), 275-281.

35. Losic, D.; Shapter, J. G.; Gooding, J. J., Influence of Surface Topography on Alkanethiol SAMs Assembled from Solution and by Microcontact Printing. *Langmuir* **2001,** 17(11), 3307-3316.

CHAPTER IV

ENTRAPMENT OF PHOTOSYSTEM I (PSI) WITHIN SELF-ASSEMBLED FILMS

Introduction

Photosystem I (PSI) is one of two key integral membrane protein complexes (along with Photosystem II) responsible for the conversion of sunlight into chemical energy through photosynthesis.[1, 2] In nature, the PSI complex functions as a photodiode, generating a potential difference of 1.0 V from the primary electron donor, P700, to the final electron acceptor, F_B.[3] Due to its unique photovoltaic properties, PSI has become the subject of huge interest for the conversion of solar energy on the nanoscale level to ultimately produce a biomimetic photoelectrochemical device.[3-5] This promising work, combined with our own studies of PSI adsorption and direct electrochemistry at monolayer surfaces, has motivated our efforts to develop a more biomimetic stabilization of PSI at a surface.

The thylakoid membrane that houses PSI consists of amphiphilic molecules that confine the hydrophobic protein complex inside the membrane. We have developed a series of steps to mimic the natural environment of the thylakoid membrane on a substrate. As shown in Figure 4.1, we first modify a gold substrate with $HSCH_6OH$ to produce a hydroxyl surface in which PSI adsorbs with approximately 70% of the electron pathways oriented parallel to the surface normal.[6] We have recently shown that PSI preferentially adsorbs onto hydroxyl-terminated self-assembled monolayers (SAMs) over methyl-terminated SAMs[7] and that this surface selectivity can be used to direct the

adsorption of PSI onto micropatterned surfaces.[8] We have also achieved direct electron

transfer from the underlying gold electrode through a HOC_6S/Au SAM to the P700

reaction center of PSI (Chapter VI), an important step toward the fabrication of PSI-based

devices.[9] In the second step, we expose the hydroxyl surface to a dilute solution of PSI

for 1 min at 4°C; the short time and low concentration are selected to prevent the protein

from forming a dense layer, leaving inter-protein spaces that can be backfilled with a

longer-chained alkanethiol. Due to a lack of stability of the HOC_6S/Au monolayer, a

longer-chained alkanethiol can easily displace the shorter more disorganized monolayer

at exposed regions of the surface. This exchange and backfilling creates a protein layer

confined on the surface by the hydrocarbon chains of the longer adsorbate, mimicking

that in the natural thylakoid environment. While the use of this backfilling strategy to

create mimics of the thylakoid membrane is new, others have used backfilling at

biological interfaces.   Tarlov et al.[10] demonstrated that backfilling of an adsorbed

oligomeric single-stranded DNA with $-SC_6OH$ resulted in a transition from a compact to

an extended configuration which allowed for nearly 100% hybridization of the DNA

strands since they were now preferentially oriented toward the substrate normal.
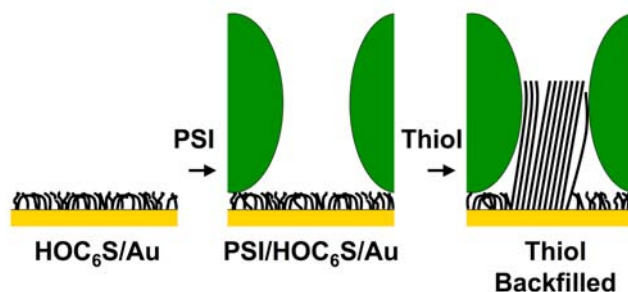
Figure 4.1. Schematic of the adsorption and backfilling of $PSI/HOC_6S/Au$ substrates.

The preparation of backfilled PSI layers (Figure 4.1) requires rapid and effective place exchange of the HOC_6S/Au SAM by the longer-chained alkanethiol without significant loss or destruction of the adsorbed PSI complexes. Place exchange processes are affected by the chain lengths of the adsorbed thiolate and competing thiol,[11] the structure or defect density[12-14] of the adsorbed monolayer, the terminal groups[15] of the adsorbed thiolates and competing adsorbate, and the solvent.[16] Poirier et al.[17] found that packing arrangement of a HOC_6S/Au monolayer is altered by the end-groups forming an oblique lattice as opposed to the hexagonal lattice[18-20] formed by its methyl counterpart. Recently, Tsukamoto et al.[21] provided supporting information on the structure of SAMs prepared from mercaptoalcohols. In their study, they report that the short-chained hydroxyl-terminated moieties lie almost parallel to the gold surface to maximize hydrogen bonding, preventing the structure from forming the typical ($\sqrt{3}$ x $\sqrt{3}$) R30° structure. Therefore, polar solvents that destabilize the hydrogen bonding of the hydroxyl termini could greatly promote exchange. Such polar solvents are also poor solvents for long-chain thiols and would thereby energetically promote the exchange to minimize unfavorable interactions between the solvent and the competing thiol. Therefore, to test this hypothesis, we have selected isooctane, a good solvent for long-chain thiols with no ability to disrupt hydrogen bonding, as well as 2-butanol, ethanol, and an aqueous micellar solution of pentaethylene glycol monododecyl ether ($C_{12}E_5$), which are increasingly poor solvents for long-chained thiols with capabilities to interfere with hydrogen bonding between surface hydroxyls. The aqueous micellar solution is particularly attractive for maintaining PSI secondary structure, as PSI is commonly stabilized in water by a similar nonionic surfactant, Triton X-100. In addition, aqueous

micellar solutions enable the preparation of SAMs that are extremely high quality. Our group has previously shown that C_nS/Au SAMs (n = 8 – 18) prepared from aqueous micellar solutions exhibit greater packing densities[22] and are more stable to solvent exposure[23] as compared with SAMs prepared from ethanol or isooctane.

For the potential application of a wet electrochemical cell based on PSI, the backfilling approach described here could be useful in minimizing background current. To adsorb PSI, we use very thin (< 1 nm) SAMs on gold to reduce the distance for electron tunneling from the gold surface and aid the incorporation of PSI into a biological circuit. However, such a thin SAM allows a high capacitive current. In order to detect an electrical response of PSI on a surface, the amount of background signal or charging current must be reduced to improve the speed of measurement. Alkanethiolate SAMs on gold, particularly those with chain length greater than 12, have been shown to effectively reduce the interfacial capacitance because of their dielectric properties.[24] By backfilling the PSI layer with a long-chain thiol, the interfacial capacitance and charging current is reduced, which in turn decreases the background interference in an electrochemical measurement, and speeds up the instrument response.[25] Creager and Olsen[26] have demonstrated the use of self-assembled monolayers in background current suppression relative to uncoated electrodes in order to detect the presence of glucose after adsorption of a glucose oxidase layer on top of a hydroxyl-terminated self-assembled monolayer.

Here, we describe a new method using SAMs to suppress the background current as well as reduce the likelihood of charge recombination between adjacent PSI reaction centers on the modified $PSI/HOC_6S/Au$ substrate. By backfilling the space between PSI complexes, with a longer-chain alkanethiol, we can effectively insulate the reaction

centers and possibly suppress the quenching of electron-hole pairs. Kong et al.[5] also expressed the effect of charge recombination on the photoelectric performance of bacteria reaction centers entrapped on mesoporous WO_3-TiO_2. However, in their design, pores of a specific dimension must be created to entrap and immobilize the proteins without the ability to control orientation. O'Neill and Greenbaum[27] have also entrapped PSI in a hybrid organosilicate glass; however, they observed a decrease in photocatalytic activity due to the removal of solvent from the gel, possibly due to a conformational restriction and difficulty obtaining a large pore size necessary for entrapment of PSI. Our method of entrapment of PSI on the surface does not require the tedious synthesis of pores of the appropriate size of a large transmembrane protein, ~150 Å in diameter,[28] but rather surrounds the protein from a bottom-up assembly process.

Also, because PSI is an integral membrane protein, we have found it to be resistant to exposure to organic solvents and long-chained alkanethiols. Other integral membrane proteins have also been shown to resist denaturation. Huang et al.[29] demonstrated that delipidated bacteriorhodopsin did not denature even after exposure to treatments that would denature most proteins. Gennis et al.[30] observed that the integral membrane enzyme, C_{55}-isoprenoid alcohol phosphokinase from *Staphylococcus aureus*, maintained stability in 1-butanol such that the circular dichroism spectrum was similar to that of the active form in lipid dispersion. Saborowski et al.[31] found that trypsin activity was increased 2.5-fold in the presence of ethanol and acetone with a 30-fold increase of activity in the presence of 2-propanol. Huang et al.[32] also renatured delipidated bacteriorhodopsin by the addition of ethanol such that the α-helical content was close to

that of the native protein in Triton X-100. We show here that PSI maintains its secondary structure on the surface even after exposure to alkanethiols in ethanol and $C_{12}E_5$ (aq).

We expect that this backfilling process may be useful in a broader sense to stabilize various biological interfaces, in particular those of integral membrane proteins. The development of biological circuits and biomolecular electronic devices[33-35] requires the adsorption of proteins onto surfaces and integration with non-biological materials. Denaturation of proteins upon immobilization on a surface is one of the largest hurdles to overcome when incorporating proteins into these devices. Upon adsorption on the surface, the protein should be prevented from spreading and piling,[36] which usually results in a loss of protein function.[37-40] Stabilization of the protein on a surface may be able to prevent or impede the spreading of the protein.

Results and Discussion

Surface Coverage of Photosystem I (PSI) on HSC_6OH Modified Au Substrates

Control over the coverage of the PSI layer on the surface is essential in the design of tailored interfaces through the backfilling approach described in Figure 4.1. Here, we control the coverage of PSI on HOC_6S/Au by altering the adsorption time and solution composition. Upon a ~24 h exposure of HOC_6S/Au to an undiluted PSI solution (6.5 x 10^{-6} mol L^{-1} of P700 and 0.31 mg mL^{-1} chlorophyll), the thickness of the PSI layer is 65 ± 1 Å. This thickness is consistent with a dense monolayer of PSI atop the HO-terminated SAM, considering that the size of PSI particles has been reported as 6 nm in length and 5 nm in width.[41] By diluting the amount of PSI in aqueous buffer by a factor of ~25 down

96

to a P700 concentration of 1.5×10^{-7} mol L^{-1}, and maintaining the concentration of the nonionic surfactant Triton X-100, responsible for the solubilization of PSI in water, we can limit the amount of PSI adsorbed onto the surface. Figure 4.2 demonstrates that PSI, at low concentrations and at 4°C, does not achieve complete monolayer coverage even after 22 h of adsorption. A thickness of approximately 30 Å after 1 h of adsorption correlates with an estimated half coverage of PSI on the surface since SE incorporates an ensemble averaging technique to attain thickness values. By diluting the concentration of PSI while maintaining the concentration of the nonionic surfactant used in the extraction process, we are affecting the equilibrium process of adsorption of PSI on the surface while still maintaining a concentration sufficient to theoretically cover the entire surface with PSI.
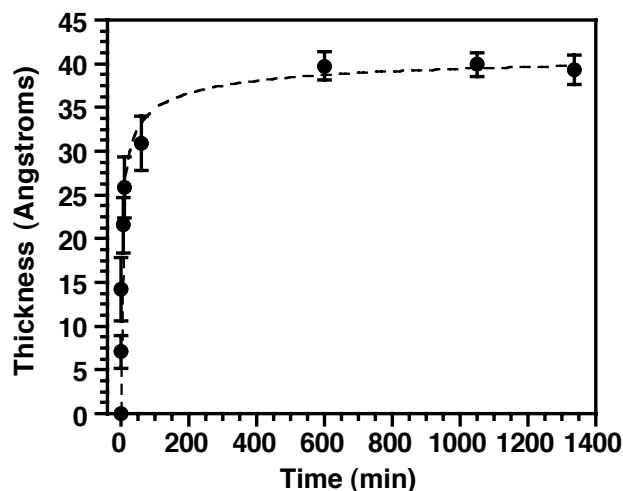
Figure 4.2. The increase in thickness (•) of PSI on a HSC$_6$OH monolayer on Au, determined by SE, as a function of time with a P700 concentration of 1.5×10^{-7} mol L^{-1}. The dashed curve (-) is a fit of the data using a second order diffusion-limited Langmuir model where k is estimated from the fit as 1.56×10^6 L mol^{-1} min$^{-1/2}$. The χ^2 value for the fit is 6.82 and the correlation coefficient (R^2) for the fit is 0.998.

As shown in Figure 4.2, the kinetics of adsorption of PSI are well represented by a second-order diffusion-limited Langmuir model defined as:[42]

$$\frac{d\theta}{dt} = kc(1-\theta)^2 t^{-1/2}$$ (4-1)

and

$$\theta(t) = \frac{2kct^{1/2}}{1 + 2kct^{1/2}}$$ (4-2)

where t [min] is time, k [L mol^{-1} min$^{-1/2}$] is the adsorption rate constant, and c [mol L^{-1}] is the concentration of PSI. From the fit shown in Figure 4.2, the adsorption rate constant for PSI at a concentration of 1.5 x 10^{-7} mol L^{-1} is 1.56 x 10^6 L mol^{-1} min$^{-1/2}$. A second-order diffusion-limited Langmuir model (R^2=0.998) accounts for the role of diffusion on the transport of a large protein complex to a surface in a stagnant solution. Other common Langmuir models such as first-order (R^2= 0.946), first-order diffusion-limited (R^2=0.988), and second-order (R^2=0.971) did not produce as good of a fit to the data. Others have shown first-order adsorption processes for various proteins,[43-47] but needed to modify the model in order to obtain better fits. Our integral membrane protein is solubilized by a nonionic surfactant, Triton X-100, which creates a Triton shell surrounding the protein and an adsorbed Triton layer on the surface of the SAM.[7, 48] We believe that this Triton shell surrounding the membrane protein may be important in

dictating inter-protein spacing and contributing to the second-order $(1-\theta)^2$ dependence of adsorption that we observe.

The thicknesses obtained by spectroscopic ellipsometry can be correlated with the absorbance of the Amide I band obtained in RAIRS, which is a function of the concentration of the protein layer on the surface and the orientation of the C=O and C-N transition dipole moments relative to the surface normal (Figure 4.3). As the measured thickness increases, the absorbance of the Amide I region increases linearly with a correlation coefficient (R^2) of 0.94. Our results are similar to those of Fink et al.,[49] who demonstrated that Amide II peak intensities were linearly proportional to the concentration of protein on a surface. The Amide I region is of particular interest here since secondary structure can be determined after deconvolution and/or second-derivative spectroscopy.[50] The peak positions used to assign the secondary structure of PSI from deconvolution are listed in Table 2.2 Chapter II. After deconvolution of the Amide I bands of diluted PSI adsorbed onto a HOC_6S/Au substrate at 4°C over a period of 1 min to 22 h, the α helical, β turn, β sheet, and unordered helical content is approximately 47 ± 3 %, 25 ± 7 %, 20 ± 5%, and 8 ± 5 %, respectively. This content correlates well with the secondary structure of PSI reported by Ruan et al.[51] Because there is no significant change in the secondary structure as a function of time of adsorption, PSI appears to maintain its structure on the surface without using protein-protein interactions to do so. In agreement with the idea that PSI maintains function on the surface without being densely packed, Lee et al.[52] observed that PSI occupied ~70% of a 2-mercaptoethanol modified gold surface after 12 h of incubation in PSI solution, and also demonstrated that

PSI maintains its photocatalytic properties[53] on this surface without being in a densely packed state.
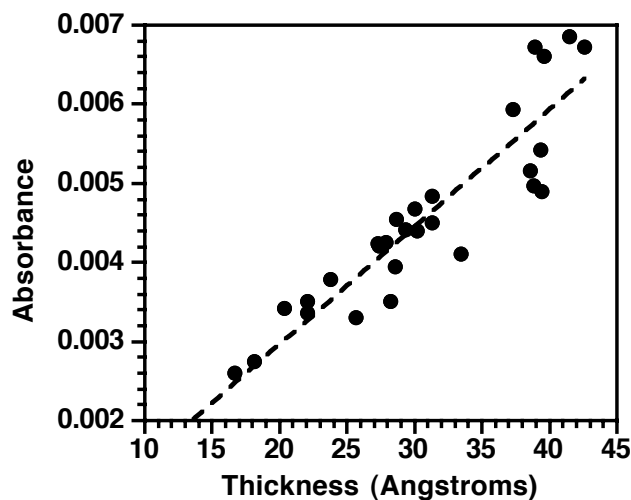
Figure 4.3. Correlation between the thickness of an adsorbed PSI layer onto a HOC$_6$S/Au substrate measured by SE and the height of the absorbance of the Amide I band detected by RAIRS. The dashed line is a linear fit of the data with a zero y-intercept where the slope of the line is 1.48×10^{-4} (Å^{-1}), the correlation coefficient (R^2) is 0.94, and the χ^2 value for the fit is 6.4×10^{-6}.

Backfilling of PSI/HOC$_6$S/Au Modified Substrates with C$_{22}$SH: PSI Exposure to Solvents

Controlling the surface coverage of PSI allows room for a longer-chained alkanethiol to backfill the regions where PSI did not adsorb, effectively insulating and confining the protein. The rate of backfilling by an alkanethiol is not only controlled by the surface coverage of PSI, but also by the nature of the solvent of the alkanethiol. The selection of backfilling solvent is important to ensure minimal or no effect on the adsorbed PSI complexes while providing effective solvation of the long-chain thiols and aiding their assembly in the inter-protein domains. The selected solvent must also be able

to deliver long-chain alkanethiols to the surface. Alkanethiolate SAMs have been prepared from a wide variety of solvents, including isooctane,[54-56] ethanol,[57] carbon dioxide,[58] and aqueous micellar solutions,[22, 23, 42, 59, 60] and the choice of solvent can affect the quality of the SAM produced. As the hydrocarbon chain length of the alkanethiol increases, the solubility in polar solvents decreases. The solvation energy of the solvent will moderate the dispersive forces in the in monolayer such that a poorer solvent should present more of a driving force for self-assembly onto a substrate. We have previously shown that C_nS/Au SAMs (n = 8-18) prepared from aqueous micellar solutions exhibit greater packing densities[22] and are more stable to solvent exposure[23] as compared with similar SAMs prepared from ethanol or isooctane. Here, we compare the backfilling effectiveness of isooctane, 2-butanol, ethanol, and an aqueous solution of pentaethylene glycol monododecyl ether ($C_{12}E_5$ (aq)).

As shown above, the concentration of PSI in solution and the time of adsorption on the surface controls the coverage of PSI on a HOC_6S/Au substrate. The coverage of protein on the surface affects the amount of available inter-protein, SAM-exposed surface area that can be place exchanged with a longer-chained alkanethiol. Figure 4.4 shows RAIR spectra of $PSI/HOC_6S/Au$ at different PSI coverages upon exposure to 1 mM $C_{22}SH$ in ethanol for 2 h. At higher coverages of PSI, backfilling of $PSI/HOC_6S/Au$ substrates with $C_{22}SH$ is greatly impeded, as indicated by only slight increases in the C-H stretching region of the RAIR spectra in Figure 4.4. As measured by SE, the thickness of the ~60% coverage $PSI/HOC_6S/Au$ substrate before (37 Å ± 3 Å) and after (39 Å ± 1 Å) ethanolic $C_{22}SH$ exposure is nearly unchanged. Another important aspect of Figure 4.4 is the lack of change in the Amide region of the RAIR spectra. After 2 h of exposure to an

ethanolic solution of $C_{22}SH$, PSI maintains its secondary structure (shown more quantitatively in Table 4.1) indicating that the ethanol solvent does not denature the membrane protein and the long-chained alkanethiol does not penetrate the protein and induce conformational changes.
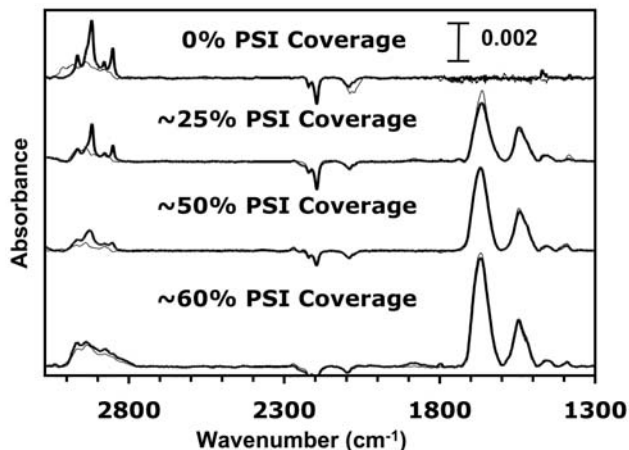
Figure 4.4. RAIR spectra of 0% to 60% monolayer coverage of PSI on HOC_6S/Au substrates before (faint line) and after (dark line) backfilling with $C_{22}SH$ from ethanol for 2 h. The Amide I and II bands are observed at 1666-1669 and 1545-1547 cm^{-1}, respectively, and the C-H stretching bands are observed in the regions of 2800-2900 cm^{-1}. The spectra are offset for clarity.

When the amount of PSI on the HOC_6S/Au substrate is limited, in this case to 25% of a full monolayer, the density of the protein on the surface is reduced and $C_{22}SH$ can successfully backfill the inter-protein domains on the substrate as shown in Figure 4.4 by the increased intensities of the asymmetric and symmetrical methyl and methylene stretching vibrations. After 2 h of backfilling with $C_{22}SH$, the asymmetric and symmetric methylene peak positions are located at 2919 cm^{-1} and 2851 cm^{-1}, respectively, indicating the formation of a trans-extended monolayer with few gauche defects in the inter-protein

domains. Minimal loss of PSI is suggested by the slight decrease in Amide I band

intensities after backfilling with $C_{22}SH$. Also, after exposure of the PSI modified

substrate at low protein coverage to an ethanolic alkanethiol solution for up to 3 h, there

is no significant change in the secondary structure of the protein (Table 4.1). After

observing that $C_{22}SH$ does not successfully backfill the $PSI/HOC_6S/Au$ substrate at high

surface coverages, but does backfill the $PSI/HOC_6S/Au$ substrate at low surface coverage

and rapidly exchanges with the HOC_6S/Au monolayer in the absence of PSI, we conclude

that $C_{22}SH$ is primarily place exchanging with the exposed surface sites of the HOC_6S/Au

monolayer and generally not displacing protein to do so.

Table 4.1. Average secondary structure (%) of PSI on HOC_6S/Au modified substrates before and after backfilling with $C_{22}SH$ from ethanol and $C_{12}E_5(aq)$.

PSI Coverage	Backfilling Solvent		β Turn	β Sheet	Unordered Helix	α Helix
60%		Before	28 ± 6	16 ± 8	8 ± 5	48 ± 7
	Ethanol (2 h)	After	22 ± 4	22 ± 2	8 ± 1	47 ± 1
25%		Before	26 ± 6	13 ± 7	6 ± 6	55 ± 9
	Ethanol (10 s to 3 h)	After	26 ± 2	16 ± 3	8 ± 1	49 ± 4
25%		Before	26 ± 5	10 ± 6	5 ± 4	59 ± 8
	$C_{12}E_5$ (aq) (1 h to 3 h)	After	27 ± 5	12 ± 5	8 ± 6	53 ± 4

To gain additional insight on the backfilling process, we have measured the

thickness and interfacial capacitance as a function of exposure time to ethanolic $C_{22}SH$

(Figure 4.5). As the time of backfilling increases, the average film thickness increases

due to exchange of exposed -SC_6OH adsorbates by $C_{22}SH$. The total change in film

thickness (~17 Å), after 3 h is consistent with the exposed –SC_6OH surface being

exchanged by $C_{22}SH$.[61] Along with an increase in overall thickness of the film, the

capacitance of the film decreases from 4 μF cm^{-2} for the PSI/HOC$_6$S/Au surface to 1.2 μF cm^{-2}, consistent with the backfilling of the inter-protein domains by C$_{22}$SH to produce a film with a lower dielectric constant that prevents electrolyte from penetrating the film and reaching the electrode surface. The progression in the increase of the advancing water contact angle of the substrate before and after backfilling with C$_{22}$SH also indicates that the surface has become increasingly hydrophobic from the original HOC$_6$S/Au advancing water contact angle of 43º ± 2º to 68º ± 2º after the addition of PSI to 98º ± 2º after backfilling with C$_{22}$SH. The rate of backfilling PSI/HOC$_6$S/Au substrates with C$_{22}$SH can be approximated by a second-order diffusion-limited Langmuir adsorption model as shown in Figure 4.5. The rate of place exchange of C$_{22}$SH with the exposed inter-protein regions of -SC$_6$OH, is roughly 3.9 x 10^{-4} L mol^{-1} min$^{-1/2}$. This rate is ~ 3 times slower than the rate of exchange in the absence of PSI, indicating that the PSI provides a measurable inhibition of the exchange rate that is a strong function of its coverage.
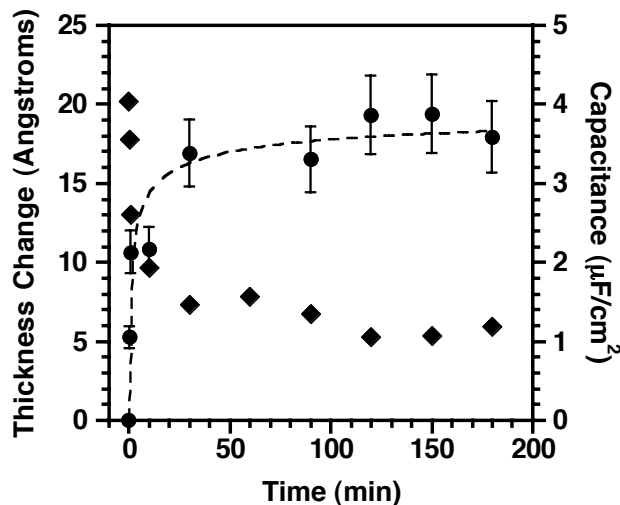
Figure 4.5. Change in thickness (●), as determined by SE, and capacitance (◆), as determined by EIS, for 25% PSI coverage on HOC_6S/Au substrates upon timed exposure to $C_{22}SH$ from ethanol. The dashed curve (-) represents the fit of a second-order diffusion-limited Langmuir model to the change in thickness of backfilled substrates with a correlation coefficient (R^2) of 0.97 and a value for k of 3.9×10^{-4} L mol^{-1} $min^{-1/2}$.

Since different solvents can affect the formation[62] and structure of alkanethiolate SAMs[23] and may have effects on the stability of adsorbed proteins such as PSI, we have also examined the backfilling of PSI/HOC_6S/Au substrates with $C_{22}SH$ from solvents besides ethanol. Figure 4.6 shows the C-H stretching region of RAIR spectra for PSI/HOC_6S/Au after exposure to 1 mM $C_{22}SH$ in ethanol, 2-butanol, isooctane, and a 20 mM aqueous solution of $C_{12}E_5$ for 2 h. Based on the appearance of absorbance peaks due to methylene and methyl stretching, $C_{22}SH$ was able to backfill the PSI/HOC_6S/Au film in ethanol, 2-butanol, and 20 mM $C_{12}E_5$ (aq) but not in isooctane, which is the strongest solvent for $C_{22}SH$. As the solubility of $C_{22}SH$ increases in a particular solvent, the driving forces for the thiol to assemble onto the surface as opposed to remaining in solution decrease. Figure 4.6 demonstrates the extent to which $C_{22}SH$ from iso-octane

place exchanges with the $-SC_6OH$ adsorbate on gold. After 2 h of exposure of the PSI/HOC$_6$S/Au substrate to C$_{22}$SH from isooctane, the asymmetric and symmetric methylene peak positions are at 2930 cm^{-1} and 2859 cm^{-1}, respectively, indicating the absence of crystalline or even liquid-like order, and the lack of methyl stretching peaks suggests the coverage of the C$_{22}$S- adsorbate is very low. Even in the absence of PSI, the exchange of HOC$_6$S/Au by C$_{22}$SH in isooctane was very slow in comparison to the more polar solvents studied. Not only will C$_{22}$SH prefer the isooctane solvent, but hydrogen bonding between the hydroxyl groups on the HOC$_6$S/Au surface may hinder the penetration of the nonpolar solvent and adsorbates through the monolayer to the gold substrate. In isooctane, more favorable interactions between the solvent and the long-chained thiol may shift the equilibrium toward solution phase versus surface-bound species, and also induce a relaxed conformation of the adsorbate that prevents it from diffusing into tight inter-protein spaces.

Because of the increased hydrocarbon content of C$_{22}$SH as compared to a shorter-chained alkanethiol, the solubility of C$_{22}$SH in polar solvents decreases. When 20 mM C$_{12}$E$_5$ (aq), 2-butanol, and ethanol are used as solvents, C$_{22}$SH is driven onto the surface in the inter-protein domains replacing the HOC$_6$S/Au monolayer with the longer-chained methyl-terminated monolayer, which exhibits a crystalline structure as noted by the asymmetric and symmetric methylene stretching vibrations at 2919 cm^{-1} and 2851 cm^{-1}, respectively. The use of C$_{12}$E$_5$ (aq) is particularly attractive for this process since the protein layer is merely exposed to an aqueous solution, and our group has shown that SAMs with extremely low defect densities can be prepared from aqueous micellar solutions.[22, 23] Not only should backfilling from C$_{12}$E$_5$ provide a more densely packed

backfill, but the aqueous micellar solution should also provide a more favorable environment for adsorbed PSI. In fact, Odahara[63] has shown that nonionic surfactants such as $C_{12}E_5$ were more gentle on PSI than Triton X-100, the surfactant we use for stabilization of PSI in aqueous solution. We observed that the secondary structure of PSI does not exhibit any notable change after exposure to $C_{22}SH$ in $C_{12}E_5$ (aq) for 3 h, as noted in Table 4.1. As shown in Figure 4.6, backfilling $C_{22}SH$ from $C_{12}E_5$ (aq) after 2 h demonstrated the same asymmetric and symmetric methylene stretching mode positions as those for SAMs prepared formed from 2-butanol and ethanol. On average the amount of loss of PSI upon exposure to only $C_{12}E_5$(aq) for 2 h is approximately 27 ± 11 % as estimated from the loss in intensity of the Amide I band. This loss from the surface is not a result of interactions of $C_{22}SH$ with PSI, but rather, the result of exposure to the nonionic surfactant $C_{12}E_5$ that presents a more favorable environment for PSI.
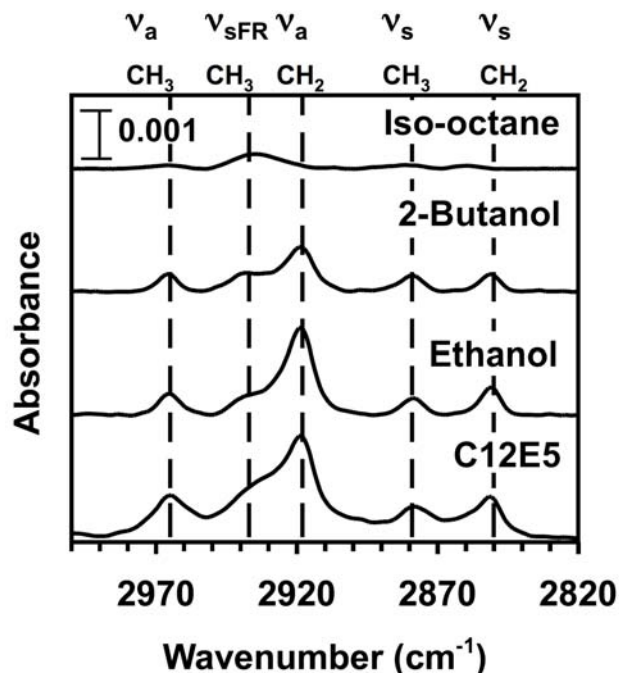
Figure 4.6. RAIR spectral comparison of 25% PSI coverage on HOC_6S/Au substrates after backfilling with $C_{22}SH$ from isooctane, 2-butanol, ethanol, and 20 mM $C_{12}E_5$ (aq) for 2 h. The methyl and methylene positions for a SAM without gauche defects have been delineated by the dashed lines with the appropriate designations above the lines. The spectra have been offset for clarity.

Backfilling of PSI/HOC_6S/Au Modified Substrates with $C_{18}OC_{19}SH$

In order to more extensively surround the integral membrane protein on the surface, we have examined backfilling of the PSI/HOC_6S/Au substrates with an ω-alkoxy-n-alkanethiol that would approximately match the height of PSI on the surface and would more closely mimic the role of the thylakoid membrane. ω-Alkoxy-n-alkanethiols can be synthesized as long chains (up to 44 carbons have been reported)[64] that result in monolayers with greater thicknesses while the ethereal oxygen in the chain increases solubility over that for an unsubstituted alkanethiol in many solvents.[64] Here, we examine the backfilling of PSI/HOC_6S/Au with $CH_3(CH_2)_{17}O(CH_2)_{19}SH$ (or

108

$C_{18}OC_{19}SH$), which, by itself, produces a SAM on gold with a thickness of 52 Å. An additional feature of the ether substitution resides in the transition dipole moment for the C-O-C stretching vibration, which lies along the chain backbone and is perpendicular to the dipole moments for the methylene stretching vibrations. Therefore, the relative intensities of the C-O-C versus CH_2 absorbances can be used to deduce information on chain orientation, such as average molecular cant and twist.[64, 65] We utilize this feature of ω-alkoxy-n-alkanethiolate monolayers to aid in determination of the orientation of the backfilled monolayer formed in the inter-protein domains on the surface.

Upon exposure of $PSI/HOC_6S/Au$ to a 0.5 mM solution of $C_{18}OC_{19}SH$ in 20 mM $C_{12}E_5$ (aq) for 1 to 3 h, the long chained thiol gradually adsorbs and backfills around the PSI as indicated by changes in RAIR spectra (Figure 4.7) and thickness, wettability, and cant/twist angles (Table 4.2). After 1 h of backfilling, the thickness change of only 14 Å, the relatively weak absorbance in C-H and R-O-R stretching of the IR spectra, and the small change in advancing contact angle are consistent with only partial backfilling. As time is increased from 2 to 3 h, a large increase in thickness marks the evolution of the backfilled SAM into a more extended and densely packed state. Consistent with this observation, the contact angle increases to > 90°, suggesting the long chains of the adsorbate have extended to present a low energy CH_3-rich surface in the inter-protein domains. From RAIRS, the wavenumber positions of the various C-H and C-O-C stretching modes do not shift over the course of 1 to 3 h backfilling; however, the intensities of the peaks do increase as additional chains adsorb to the surface. In particular, the peak intensities of the CH_3 scissor deformation at 1378 cm^{-1}, the asymmetric and symmetric CH_2 stretching vibration at 2920 cm^{-1} and 2851-2852 cm^{-1},

and the C-O-C mode at 1129 cm^{-1} increase over the course of 3 h. Importantly, the average molecular cant calculated by the method of Sinniah et al.[65] decreases from 48º at 2 h to 40º at 3 h and is consistent with the notion of chain extension and increased packing as surmised from ellipsometry and wetting data. The predominant aqueous medium may promote hydrophobic interactions between the long chains of the thiol adsorbates and facilitate the formation of the trans-extended film. From earlier work in our lab, the kinetics of thiol formation onto a gold surface from an aqueous micellar solution is dependent upon the micellar size, concentration of the solubilized thiol, and the alkanethiol chain length.[42] The longer chain length of the $C_{18}OC_{19}SH$ adsorbate as compared to $C_{22}SH$ likely reduces the rate of transfer from the micelles and thereby contributes to the slower kinetics of backfilling.

Table 4.2. Properties of PSI/HOC$_6$S/Au before and after backfilling as a function of time with $C_{18}OC_{19}SH$ from $C_{12}E_5$ (aq).

Time (h)	Thickness Before Backfilling (Angstroms) n 1.33	Thickness After Backfilling (Angstroms) n 1.46	Advancing Contact Angle (°) After Backfilling	Cant, α (°) After Backfilling	Twist, β (°) After Backfilling
1	16	30	70	47	44
2	16	34	75	48	47
3	17	58	91	40	48

Figure 4.7. RAIR spectra of 25% PSI coverage on HSC_6OH/Au substrates backfilled with $C_{18}OC_{19}SH$ from $C_{12}E_5$ (aq) over a period of 3 h. The dashed lines starting from the most left hand plot represent the υ_a (R-O-R) = 1132 cm^{-1}, υ_s (CH_2) = 2851 cm^{-1}, and υ_a (CH_2) = 2918 cm^{-1} respectively for a trans-extended monolayer with no gauche defects. The spectra have been offset for clarity.

Conclusions

We have presented a method for integration of PSI into a surface-tethered membrane mimic on a gold substrate through controlled protein adsorption and place exchange of short-chained, hydroxyl-terminated alkanethiols with longer chained methyl terminated alkanethiols. We have shown that the integral membrane protein, PSI, can be exposed to organic or aqueous solvents containing alkanethiols for a period of hours with essentially no change in secondary structure and minimal loss of protein on the surface. Our results demonstrate that the coverage of PSI can be controlled by a combination of solution conditions as well as adsorption time frames. Because the protein is not allowed to dominate the surface coverage, we can backfill the regions where PSI did not adsorb

111

through simple place exchange of the orienting short-chained hydroxyl-terminated SAM with a longer methyl-terminated SAM.

The choice of solvent dictates the quality of the backfilled SAM formed. As the polarity of the solvent increases the solubility of the alkanethiol decreases, which drives the adsorption of thiolates onto a protein modified gold surface to a greater extent than a more nonpolar solvent. Aqueous micellar solutions have been shown to preferentially backfill the $PSI/HOC_6S/Au$ substrates with a longer-chained alkoxy alkanethiol in a more densely packed fashion without exposing the integral membrane protein to organic solvents. We have shown that both $C_{22}SH$ and $C_{18}OC_{19}SH$ can be delivered to the substrate through micellar-assisted delivery with the rate of backfilling being affected by the size of the thiol. We expect that this methodology could be extended to backfill other membrane protein monolayers in a lipid-like environment.

References

1.   Pessarakli, M., *Handbook of Photosynthesis*. Marcel Dekker: New York, 1996.

2.   Raghavendra, A. S., *Photosynthesis: A Comprehensive Treatise*. Cambridge University Press: 1998.

3.   Frolov, L.; Rosenwaks, Y.; Carmeli, C.; Carmeli, I., Fabrication of a Photoelectronic Device by Direct Chemical Binding of the Photosynthetic Reaction Center Protein to Metal Surfaces. *Advanced Materials* **2005,** 17, (20), 2434-2437.

4.   Das, R.; Kiley, P. J.; Segal, M.; Norville, J.; Yu, A. A.; Wang, L.; Trammell, S. A.; Reddick, L. E.; Kumar, R.; Stellacci, F.; Lebedev, N.; Schnur, J.; Bruce, B. D.; Zhang, S.; Baldo, M., Integration of Photosynthetic Protein Molecular Complexes in Solid-State Electronic Devices. *Nano Letters* **2004,** 4, (6), 1079-1083.

5.   Lu, Y.; Yuan, M.; Liu, Y.; Tu, B.; Xu, C.; Liu, B.; Zhao, D.; Kong, J., Photoelectric Performance of Bacteria Photosynthetic Proteins Entrapped on Tailored Mesoporous WO_3-TiO_2 Films. *Langmuir* **2005,** 21, 4071-4076.

6.   Lee, I.; Lee, J.; Greenbaum, E., Biomolecular Electronics: Vectorial Arrays of Photosynthetic Reaction Centers. In *Physical Review Letters*, 1997; Vol. 79, pp 3294-3297.

7.   Ko, B. S.; Babcock, B.; Jennings, G. K.; Tilden, S. G.; Peterson, R. R.; Cliffel, D.; Greenbaum, E., Effect of Surface Composition on the Adsorption of Photosystem I onto Alkanethiolate Self-Assembled Monolayers on Gold. *Langmuir* **2004,** 20, (10), 4033-4038.

8.   Ciobanu, M.; Kincaid, H. A.; Jennings, G. K.; Cliffel, D. E., Photosystem I Patterning Imaged by Scanning Electrochemical Microscopy. *Langmuir* **2005,** 21, 692-698.

9.   Ciobanu, M.; Kincaid, H.; Lo, V.; Dukes, A. D.; Jennings, G. K.; Cliffel, D. E., Voltammetric Studies of Photosystem I Direct Electrochemistry. *Journal of American Chemical Society* **2006,** submitted.

10.   Levicky, R.; Herne, T. M.; Tarlov, M. J.; Satija, S. K., Using Self-Assembly to Control the Structure of DNA Monolayers on Gold: A Neutron Reflectivity Study. *Journal of the American Chemical Society* **1998,** 120, 9787-9792.

11.   Laibinis, P. E.; Nuzzo, R. G.; Whitesides, G. M., Structure of Monolayers Formed by Coadsorption of Two *n*-Alkanethiols of Different Chain Lengths on Gold and Its Relation to Wetting. *Journal of Physical Chemistry* **1992,** 96, (12), 5097-5105.

12.   Love, J. C.; Estroff, L. A.; Kriebel, J. K.; Nuzzo, R. G.; Whitesides, G. M., Self-Assembled Monolayers of Thiolates on Metals as a Form of Nanotechnology. *Chemical Reviews* **2005,** 105, 1103-1169.

13.   Yang, G.; Amro, N. A.; Starkewolfe, Z. B.; Liu, G.-y., Molecular-Level Approach to Inhibit Degradations of Alkanethiol Self-Assembled Monolayers in Aqueous Media. *Langmuir* **2004,** 20, 3995-4003.

14.   Baralia, G. G.; Duwez, A.-S.; Nysten, B.; Jonas, A. M., Kinetics of Exchange of Alkanethiol Monolayers Self-Assembled on Polycrystalline Gold. *Langmuir* **2005,** 21, 6825-6829.

15.   Laibinis, P. E.; Fox, M. A.; Folkers, J. P.; Whitesides, G. M., Comparisons of Self-Assembled Monolayers on Silver and Gold: Mixed Monolayers Derived from $HS(CH_2)_{21}X$ and $HS(CH_2)_{10}Y$ (X, Y = CH_3, CH_2OH) Have Similar Properties. *Langmuir* **1991,** 7, (12), 3167-3173.

16.   Schlenoff, J. B.; Li, M.; Ly, H., Stability and Self-Exchange in Alkanethiol Monolayers. *Journal of the American Chemical Society* **1995,** 117, 12528-12536.

17.   Poirier, G. E.; Pylant, E. D.; White, J. M., Crystalline Structures of Pristine and Hydrated Mercaptohexanol Self-Assembled Monolayers on Au (111). *Journal of Chemical Physics* **1996,** 104, (18), 7325-7328.

18.   Camillone, N.; Chidsey, C. E. D.; Liu, G.-y.; Scoles, G., Superlattice Structure at the Surface of a Monolayer of Octadecanethiol Self-Assembled on Au (111). *Journal of Chemical Physics* **1993,** 98, (4), 3503-3511.

19.   Fenter, P.; Eberhardt, A.; Eisenberger, P., Self-Assembly of n-Alkyl Thiols as Disulfides on Au (111). *Science* **1994,** 266, (5188), 1216-1218.

20.   Poirier, G. E.; Tarlov, M. J., The c(4x2) Superlattice of n-Alkanethiol Monolayers Self-Assembled on Au(111). *Langmuir* **1994,** 10, (9), 2853-2856.

21.   Tsukamoto, K.; Kubo, T.; Nozoye, H., Structure of Mercaptoalcohol Self-Assembled Monolayers on Au(111). *Applied Surface Science* **2005,** 244, 578-583.

22.   Yan, D.; Saunders, J. A.; Jennings, G. K., Enhanced Chain Densities of n-Alkanethiolate Self-Assembled Monolayers on Gold from Aqueous Micellar Solutions. *Langmuir* **2000,** 16, (20), 7562-7565.

23.   Yan, D.; Saunders, J. A.; Jennings, G. K., Formation and Stability of Hexadecanethiolate SAMs Prepared in Aqueous Micellar Solutions of C12E6. *Langmuir* **2003,** 19, (22), 9290-9296.

24.   Porter, M. D.; Bright, T. B.; Allara, D. L.; Chidsey, C. E. D., Spontaneously Organized Molecular Assemblies. 4. Structural Characterization of n-Alkyl Thiol Monolayers on Gold by Optical Ellipsometry, Infrared Spectroscopy, and Electrochemistry. *Journal of the American Chemical Society* **1987,** 109, (12), 3559-3568.

25.   Huang, J. Characterization of Electrochemical Interfaces by Infrared Spectroscopy. dissertation, Virginia Polytechnic Institute and State University, Blacksburg, 1996.

26.   Creager, S. E.; Olsen, K. G., Self-Assembled Monolayers and Enzyme Electrodes: Progress, Problems and Prospects. *Analytica Chimica Acta* **1995,** 307, 277-289.

27.   O'Neill, H.; Greenbaum, E., Spectroscopy and Photochemistry of Spinach Photosystem I Entrapped and Stabilized in a Hybrid Organosilicate Glass. *Chemistry of Materials* **2005,** 17, 2654-2661.

28.   Ben-Shem, A.; Frolow, F.; Nelson, N., Crystal Structure of Plant Photosystem I. *Nature* **2003,** 426, (December 11, 2003), 630-635.

29.   Huang, K.-S.; Bayley, H.; Khorana, H. G., Delipidation of Bacteriorhodopsin and Reconstitution with Exogenous Phospholipid. *Proceedings of the National Academy of Sciences of the United States of America* **1980,** 77, (1), 323-327.

30.   Gennis, R. B.; Sinensky, M.; Strominger, J. L., Activation of C_{55}-Isoprenoid Alcohol Phosphokinase from *Staphylococcus aureus*. *The Journal of Biological Chemistry* **1976,** 251, (5), 1270-1276.

31.   Saborowski, R.; Sahling, G.; Navarette del Toro, M. A.; Walter, I.; Garcia-Carreno, F. L., Stability and Effects of Organic Solvents on Endopeptidases from the Gastric Fluid of the Marine Crabe *Cancer pagurus*. *Journal of Molecular Catalysis B: Enzymatic* **2004,** 30, 109-118.

32.   Huang, K.-S.; Bayley, H.; Liao, M.-J.; London, E.; Khorana, H. G., Refolding of an Integral Membrane Protein. *The Journal of Biological Chemistry* **1981,** 256, (8), 3802-3809.

33.   Phadke, R. S., Biomolecular Electronics in the Twenty-First Century. *Applied Biochemistry and Biotechnology* **2001,** 96, (1-3), 269-276.

34.   Rinaldi, R.; Branca, E.; Cingolani, R.; Felice, R. D.; Calzolari, A.; Molinari, E.; Masiero, S.; Spada, G.; Gottarelli, G.; Garbesi, A., Biomolecular Electronic Devices Based on Self-Organized Deoxyguanosine Nanocrystals. *Annals of the New York Academy of Sciences* **2002,** 960, 184-192.

35.   Willner, I.; Willner, B., Molecular and Biomolecular Optoelectronics. *Pure and Applied Chemistry* **2001,** 73, (3), 535-542.

36.   Chang, C.-H.; Liao, J.-D.; Chen, J.-J. J.; Ju, M.-S.; Lin, C.-C. K., Alkanethiolate Self-Assembled Monolayers as Functional Spacers to Resist Protein Adsorption upon Au-Coated Nerve Microelectrode. *Langmuir* **2004,** 20, 11656-11663.

37.   Norde, W., Adsorption of Proteins from Solution at the Solid-Liquid Interface. *Advances in Colloid and Interface Science* **1986,** 25, 267-340.

38.   Norde, W.; MacRitchie, F.; Nowicka, G.; Lyklema, J., Protein Adsorption at Solid-Liquid Interfaces: Reversibility and Conformation Aspects. *Journal of Colloid and Interface Science* **1986,** 112, (2), 447-456.

39.   Sukhishvili, S. A.; Granick, S., Adsorption of Human Serum Albumin: Dependence on Molecular Architecture of the Oppositely Charged Surface. *Journal of Chemical Physics* **1999,** 110, (20), 10153-10161.

40.   Sethuraman, A.; Belfort, G., Protein Structural Perturbation and Aggregation on Homogeneous Surfaces. *Biophysical Journal* **2005,** 88, 1322-1333.

41.   Lee, J. W.; Lee, I.; Laible, P. D.; Owens, T. G.; Greenbaum, E., Chemical Platinization and its Effect on Excitation Transfer Dynamics and P700 Photooxidation Kinetics in Isolated Photosystem I. *Biophysical Journal* **1995,** 69, 652-659.

42.   Yan, D.; Saunders, J. A.; Jennings, G. K., Kinetics of Formation for n-Alkanethiolate Self-Assembled Monolayers onto Gold in Aqueous Micellar Solutions of C12E6 and C12E7. *Langmuir* **2002,** 18, (26), 10202-10212.

43.   May, S.; Harries, D.; Ben-Shaul, A., Lipid Demixing and Protein-Protein Interactions in the Adsorption of Charged Proteins on Mixed Membranes. *Biophysical Journal* **2000,** 79, 1747-1760.

44.   Burns, J., Ramon A.; El-Sayed, M. Y.; Roberts, M. F., Kinetics Model for Surface-Active Enzymes Based on the Langmuir Adsorption Isotherm: Phospholipase C (Bacillus cereus) Activity Toward Dimyristoyl Phosphatidylcholine/ Detergent Micelles. *Proceedings of the National Academy of Sciences of the United States of America* **1982,** 79, 4902-4906.

45.   Li, S.; Hu, J.; Liu, B., A Study on the Adsorption Behavior of Protein Onto Functional Microspheres. *Journal of Chemical Technology and Biotechnology* **2005,** 80, 531-536.

46.   Shentu, J.; Wu, J.; Song, W.; Jia, Z., Chitosan Microspheres as Immobilized Dye Affinity Support for Catalase Adsorption. *International Journal of Biological Macromolecules* **2005,** 37, 42-46.

47.   Shen, D.; Huang, M.; Wang, F.; Yan, M., Impedance Analysis of an Electrode-Separated Piezoelectric Sensor as a Surface-Monitoring Technique for Gelatin Adsorption on Quartz Surface. *Journal of Colloid and Interface Science* **2005,** 281, (2), 398-409.

48.   Grant, L. M.; Ederth, T.; Tiberg, F., Influence of Surface Hydrophobicity on the Layer Properties of Adsorbed Nonionic Surfactants. *Langmuir* **2000,** 16, 2285-2291.

49.   Fink, D. J.; T.B., H.; Chittur, K. K.; Gendreau, R. M., Quantitative Surface Studies of Protein Adsorption by Infrared-Spectroscopy. 2. Quantification of Adsorbed and Bulk Proteins. *Analytical Biochemistry* **1987,** 165, (1), 147-154.

50.   Arrondo, J. L.; Goni, F. M., Structure and Dynamics of Membrane Proteins as Studied by Infrared Spectroscopy. *Progress in Biophysics and Molecular Biology* **1999,** 72, 367-405.

51.   Ruan, X.; Wei, J.; Xu, Q.; Wang, J.-s.; Gong, Y.-d.; Zhang, X.-f.; Kuang, T.-y.; Zhao, N.-m., Comparison of the Effects of Triton X-100 on the Protein Secondary Structure of Photosystem I and Photosystem II studied by FTIR Spectroscopy. *Journal of Molecular Structure* **2000,** 525, 97-106.

52.   Lee, I.; Lee, J. W.; Greenbaum, E., Biomolecular Electronics: Vectorial Arrays of Photosynthetic Reaction Centers. *Physical Review Letters* **1997,** 79, (17), 3294-3297.

53.   Lee, I.; Lee, J.; Stubna, A.; Greenbaum, E., Measurement of Electrostatic Potentials above Oriented Single Photosynthetic Reaction Centers. *Journal of Physical Chemistry B* **2000,** 104, 2439-2443.

54.   Shon, Y.-S.; Lee, R. T., A Steady-State Kinetic Model Can Be Used to Describe the Growth of Self-Assembled Monolayers (SAMs) on Gold. *Journal of Physical Chemistry B* **2000,** 104, 8182-8191.

55.   Garg, N.; Lee, R. T., Self-Assembled Monolayers Based on Chelating Aromatic Dithiols on Gold. *Langmuir* **1998,** 14, 3815-3819.

56.   Laibinis, P. E.; Whitesides, G. M.; Allara, D. L.; Tao, Y. T.; Parikh, A. N.; Nuzzo, R. G., Comparison of the Structures and Wetting Properties of Self-Assembled Monolayers of *n*-Alkanethiols on the Coinage Metal-Surfaces, Cu, Ag, Au. *Journal of the American Chemical Society* **1991,** 113, (19), 7152-7167.

57.   Pan, W.; Durning, C. J.; Turro, N. J., Kinetics of Alkanethiol Adsorption on Gold. *Langmuir* **1996,** 12, 4469-4473.

58.   Yan, D.; Jennings, G. K.; Weinstein, R. D., Controlling the Properties of n-Alkanethiolate Self-Assembled Monolayers on Gold by Using Supercritical Carbon Dioxide-Ethanol Mixtures as Solvents. *Industrial & Engineering Chemistry Research* **2002,** 41, (18), 4528-4533.

59.   Patrone, L.; Palacin, S.; Bourgoin, J.-P.; Werts, M. H. V., Versatility of Aqueous Micellar Solutions for Self-Assembled Monolayers Engineering. *Langmuir* **2004,** 20, (26), 11577-11582.

60.   Yan, D.; Jordan, J. L.; Burapatana, V.; Jennings, G. K., Formation of n-Alkanethiolate Self-Assembled Monolayers onto Gold in Aqueous Micellar Solutions of n-Alkyltrimethylammonium Bromides. *Langmuir* **2003,** 19, (8), 3357-3364.

61.   If $C_{22}SH$ exchanged with HOC_6S/Au over the entire surface, the thickness change should be the difference in thickness of the two monolayers (30 Å – 6 Å = 24 Å). Since this exchange is occurring over only the exposed 75% of the surface, then the predicted thickness increase is ~ 18 Å, very close to the observed change of 17 Å.

62.   Peterlinz, K. A.; Georgiadis, R., In Situ Kinetics of Self-Assembly by Surface Plasmon Resonance Spectroscopy. *Langmuir* **1996,** 12, 4731-4740.

63.   Odahara, T., Stability and Solubility of Integral Membrane Proteins from Photosynthetic Bacteria Solubilized in Different Detergents. *Biochimica Et Biophysica Acta* **2004,** 1660, 80-92.

64.   Jennings, G. K.; Yong, T. H.; Munro, J. C.; Laibinis, P. E., Structural Effects on the Barrier Properties of Self-Assembled Monolayers Formed from Long-Chain ω-Alkoxy-*n*-Alkanethiols on Copper. *Journal of the American Chemical Society* **2003,** 125, (10), 2950-2957.

65.   Sinniah, K.; Cheng, J.; Terrettaz, S.; Reutt-Robey, J. E.; Miller, C. J., Self-Assembled ω-Hydroxyalkanethiol Monolayers with Internal Functionalities: Electrochemical and Infrared Structural Characterizations of Ether-Containing Monolayers. *Journal of Physical Chemistry* **1995,** 99, 14500-14505.

CHAPTER V

ADSORPTION AND ENCAPSULATION OF PHOTOSYSTEM I ON HYDROXYL-
TERMINATED FILMS WITH VARIOUS PACKING DENSITIES ON GOLD

Introduction

In Chapter IV we examined the backfilling of a short-chained hydroxyl-
terminated SAM, with and without PSI, with a longer methyl-terminated alkanethiol. We
observed that successful backfilling of PSI modified hydroxyl-terminated gold substrates
required 1 to 3 h. Although PSI did not denature upon exposure to organic solvents for 2
h, we would like to develop a method to speed up the process of backfilling with a more
protein-friendly solvent so that it can be extended to applications with other proteins.
Instead of using organic solvents, we have focused our efforts on the use of aqueous
micellar solutions as introduced in Chapter IV. In order to enhance the rate of backfilling
of protein modified SAMs, we have developed a hydroxyl-terminated monolayer that is
more amenable to place exchange with a longer-chained alkanethiol.

Our strategy for the formation of a hydroxyl-terminated monolayer that would
enhance the ability of place exchange is based upon recent research in our group on
loosely packed hydroxyl-terminated monolayers on gold.[1] These loosely packed
hydroxyl-terminated monolayers have naturally disrupted packing that facilitates
penetration of a longer-chained alkanethiol through the existing monolayer to the gold
substrate. In order to produce these loosely packed hydroxyl-terminated films, we were
inspired by the work of Lahann et al.[2] in which loosely packed carboxylate-terminated
monolayers were formed through a two-step process of adsorption of a SAM with a bulky

ester-linked triphenyl group and hydrolysis of the ester group leaving a loosely packed carboxylate-terminated film on the surface of the substrate. Instead of using a triphenyl terminal group, we have synthesized disulfides that contain a bulky fluorinated terminal group linked with an ester as shown in Figure 5.1. Upon self-assembly at a gold substrate,

$$S-(CH_2)_6-O-CO-(CF_2)_6-CF_3$$
$$|$$
$$S-(CH_2)_6-O-CO-(CF_2)_6-CF_3 \qquad \mathbf{1}$$

$$S-(CH_2)_{11}-O-CO-(CF_2)_6-CF_3$$
$$|$$
$$S-(CH_2)_{11}-O-CO-(CF_2)_6-CF_3 \qquad \mathbf{2}$$
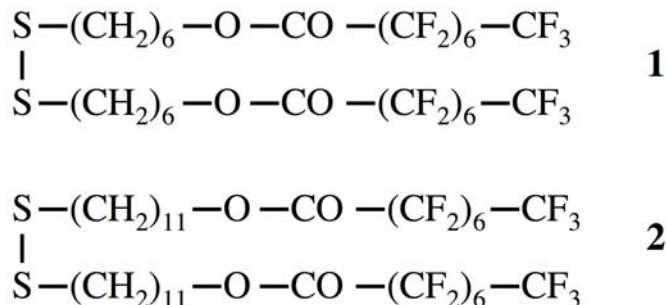
Figure 5.1. Fluorinated disulfide compounds investigated.

the fluorocarbon chain dictates chain packing to prevent the hydrocarbon chains from forming a crystalline structure. After exposure to base, the ester is rapidly cleaved to yield a loosely packed hydroxyl-terminated SAM.

Partially fluorinated alkanethiols have been shown to form ordered monolayers depending on the extent of fluorination and the length of the underlying hydrocarbon backbone. Because of the bulkiness of the fluorocarbon tailgroup, the interchain spacing of partially fluorinated alkanethiols has been shown to be larger than the interchain packing of regular alkanethiols.[3] The SAMs formed from **1** and **2** offer hydrolytic cleavability of the fluorocarbon group after assembly. Once the fluorocarbon groups are cleaved, the hydrocarbon chains are driven to restructure to maximize interchain hydrogen bonding and van der Waals interactions, producing films with intermediate

surface energy similar to that prepared by mixed SAMs without nanometer phase separation. These loosely packed films may offer distinct advantages over traditional SAMs by enabling proteins[4] such as PSI to intercalate into the film and gain greater adsorptive stabilization and by possessing a high density of intrinsic defects to enable rapid exchange/backfilling by other alkanethiols.[1]

Mixed self-assembled monolayers (SAMs)[5] have been used to design surfaces that have various functionalities and lateral steric effects combined to investigate biomolecule-surface interactions.[6, 7] Mixed SAMs that have hydrophobic and hydrophilic properties as well as variations in length allow for multiple interactions of a protein with a surface. Variations in the chemical homogeneity of mixed SAMs make it possible to create regions that would resist as well as attract the adsorption of proteins on a surface. The creation of "pockets," by variations in length of mixed SAMs, would allow for protein-substrate contacts to occur not only through binding interactions, but also through physical confinement and accessibility. Mixed monolayers often phase separate into regions or islands on the nanometer scale.[8-10] An assumption that has often been made in applying the study of mixed SAMs to biological-organic interfaces is that the phase separation of chemical functionalities is not significant enough to change the interactions of the protein with the substrate in general.

Photosystem I is a nanometer-sized integral membrane protein with both hydrophobic and hydrophilic regions that we have previously shown to preferentially adsorb to a surface with an intermediate surface energy.[11] Here, we have designed a hydroxyl-terminated SAM surface that has loosely packed hydrocarbon chains. We would expect to observe changes in the accessibility of the protein to the hydrocarbon

backbone of the alkanethiol as well as the terminal hydroxyl functionality. This accessibility to both functionalities would be particularly favorable for the adsorption of proteins with mixtures of polar and nonpolar residues. As opposed to mixed SAMs, these loosely packed hydroxyl-terminated SAMs should provide a means of producing a surface with a more homogeneous distribution of surface groups on the nanoscale. The loosely packed SAMs should also yield an intermediate surface energy as compared to that for a fully hydroxyl-functionalized surface and facilitate the intercalation of other molecules and or proteins into the void spaces of the surface as mentioned by Park et al.[12]

Another advantage of these loosely packed films lies in the formation process. In order to form reproducible mixed SAMs, one must maintain the exact ratio of two alkanethiols, the total solution concentration, the temperature, and the adsorption time. In a mixed hydroxyl/methyl system, the methyl-terminated alkanethiol will typically dominate adsorption on the surface over the hydroxyl-terminated alkanethiol, and once adsorbed, the methyl-terminated alkanethiol is not easily displaced. In order to produce a mixed SAM with a surface energy only slightly increased over that of the hydroxyl-terminated SAM, the concentration ratio of methyl:hydroxyl alkanethiols must be low, and the time frames of adsorption controlled, often with an extensive trial-and-error procedure before appropriate conditions can be identified. For the formation of loosely packed films, we are not concerned with errors introduced by the balancing of two moieties competing for adsorption because we adsorb one alkanethiol onto the surface and allow for the formation of a more uniform surface. Also, we are not under the constraints of equilibrium adsorption times necessary for that perfect balance of hydroxyl to methyl ratio on the surface since our surfaces can be left in solution indefinitely with

only a one-step cleaving process necessary the day of experimentation resulting in a film with a more uniform distribution of hydroxyl-moieties and an intermediate surface energy that is a function of the hydrocarbon chain length.

We expect that loosely packed hydroxyl-terminated SAMs would provide a surface more amenable to the enhancement of protein adsorption as observed by Choi et al.[4, 13] and aid in the confinement of the protein on the surface after backfilling of inter-protein spaces with a longer methyl-terminated alkanethiol. Recent research in our group has demonstrate that these loosely packed hydroxyl-terminated alkanethiols, where the structural order of the monolayer is disrupted, are easily place exchanged with longer alkanethiols.[1] This feature is particularly attractive for the backfilling of a protein and/or SAM modified substrate with minimal exposure times to the backfilling alkanethiol and solvent. Here, we demonstrate the place exchange characteristics of loosely packed monolayers, which we will now refer to as cleaved monolayers, as compared to their counterparts formed from regular ω-alkanethiol solutions with and without protein and compare the quality and rates of the two. Also, we examine the effect of chain length and surface energy on the adsorption of PSI over a series of hydroxyl-terminated ω-alkanethiols (C_nSH (n = 2, 4, 6, 8, and 11)).

Results and Discussion

Preparation of Cleaved HOC$_6$S/Au Monolayers

Figure 5.2a shows the hydrocarbon and fluorocarbon regions of RAIR spectra for SAMs prepared from **1**. The peaks due to perpendicular (ν_{pd}) and axial (ν_{ax}) C-F

stretching vibrations are observed at 1253 cm^{-1} and 1336 cm^{-1}, respectively, as shown in Table 5.1. These peak positions are very similar to those measured by Berron and Jennings[1] for SAMs prepared from **2** onto gold at 1255 cm^{-1} and 1335 cm^{-1}, respectively. These positions compare well with those of SAMs of partially fluorinated alkanethiols on gold.[14] We cannot draw much detail from the C-H stretching region in Figure 5.2a due to the poor signal for short hydrocarbons in RAIRS. SAMs prepared from **2**, which is five methylene units longer, displayed liquid-like packing on the basis of asymmetric and symmetric methylene stretching modes at 2927 cm^{-1} and 2856 cm^{-1}, respectively.[1] SAMs from **1** are likely to exhibit similar levels of non-crystalline packing. Schönherr and Vancso[15] observed that the molecular structures of the compositionally similar $F_9O_2C_6S$/Au and $F_9O_2C_{11}S$/Au transition from a p (2 x 2) to a c (7 x 7) structure formed by the tail groups as seen in Figure 5.3c and 5.3a, respectively. While the bulky fluorocarbon tail groups likely play a major role in dictating the molecular structure, the hydrocarbon chain length does influence the structure even though the diameter of the helical CF_2 segments (5.6 Å)[3] is larger than the interchain distance for crystalline hydrocarbon segments (4.6 Å).[16]

The ester linkage of bis(perfluoralkyl) disulfides allows for modification of a highly hydrophobic monolayer into a more hydrophilic monolayer in a matter of minutes. The rate of hydrolysis[17] of the perfluoroalkyl[18] ester[19] is determined by the basicity of the nucleophile and the leaving group such that the transition state is reactant-like when the nucleophile is more basic than the leaving group, and product-like when the nucleophile is less basic than the leaving group.[20, 21] However, these simple generalities do not take into account the blocking effect of oriented groups densely packed on a substrate. Dordi

et al.[22] observed that the rate of alkaline hydrolysis of NHS ester groups confined in SAMs on gold were slower than those reported in solution and were also dependent upon the alkane segment length linking the ester to the disulfide anchor group. Earlier work from our group[1] demonstrated the hydrolysis of $F_7O_2C_{11}S$/Au monolayers (prepared from **2**) with 0.l M KOH(aq) within 5 min forming a cleaved $HOC_{11}S$/Au monolayer that is loosely packed with an advancing water contact angle of $68° ± 3°$.
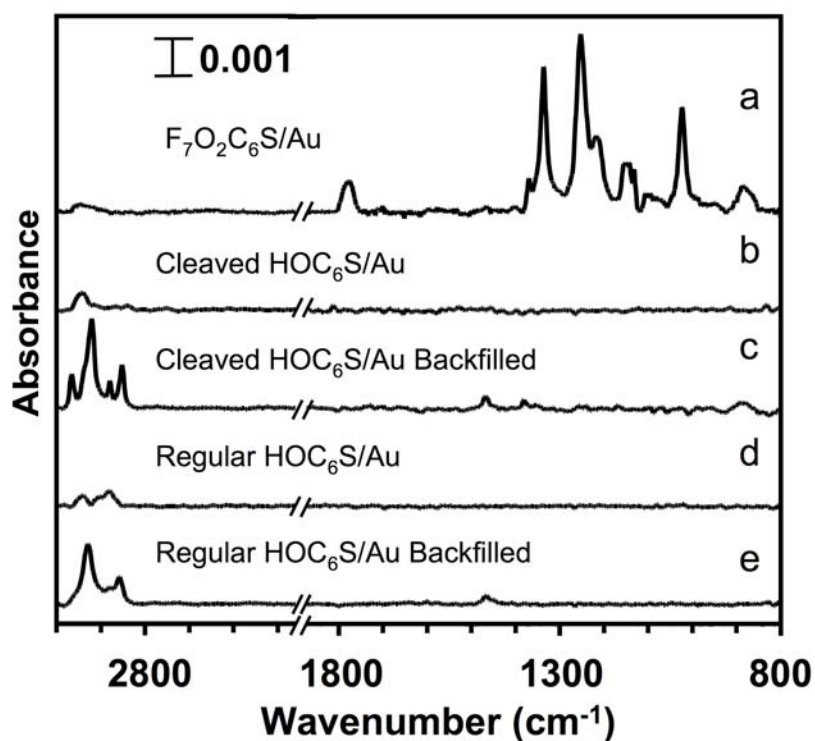

Figure 5.2. RAIR spectra of $F_7O_2C_6S$/Au (a), cleaved HOC_6S/Au before (b) and after (c) backfilling with $C_{22}SH$ from $C_{12}E_5$(aq) for 10 min, and a regular HOC_6S/Au film before (d) and after (e) 10 min backfilling with $C_{22}SH$ from $C_{12}E_5$(aq). The spectra are offset for clarity.

Table 5.1. Peak assignments of infrared vibrational modes of semifluorinated alkanethiols[23] compared to bis(6,6'-dithiohexyl) perfluoroheptanoate monolayers on gold.

Mode Assignment	$F_{10}H_{17}S/Au$ Wavenumber (cm^{-1})	$F_7O_2C_6S/Au$ Wavenumber (cm^{-1})
Carbonyl		1776
$\nu(CF_2)$ progression, axial CF_2 stretch	1375 s	1370
	1346 s	1336
Characteristic fingerprint region of fluorocarbons	1262 sh	
involving $\nu_{asym}(CF_2)$ perpendicular helical axis and	1252 w	1253
$r(CF_2)$		
$\delta(CCC), \nu(CC), \nu_{asym}(CF_2) + \nu_{asym}(CF_3)$	1219 vs	1217
$\nu_{sym}(CF_2), \delta(CF_2)$	1155 vs	1152
Unassigned	1140 sh	1143
$\nu(CC)$	1130 m	1132
	1113 w	1106
	1075 w	
	1053 w	1024
$\nu(CF_2)$ progression	900 m	
$\nu(CF_2)$ progression	882 s	886

Abbreviations: ν-stretch, δ-bend, r-rock, w-wag, asym-asymmetric, sym-symmetric, vs-very strong, s-strong, m-medium, w-weak, sh-shoulder

When we hydrolyze the same $F_7O_2C_{11}S/Au$ monolayers with an ethanolic 0.1 M KOH solution, the average advancing water contact angles decrease from $121° \pm 1°$ to $63° \pm 2°$ after only a 1 s exposure and further down to $56° \pm 2°$ after a 1 min exposure. For the present study, hydrolysis of $F_7O_2C_6S/Au$ monolayers occurs in 1 min when using an ethanolic 0.1 M KOH solution as shown in Figure 5.2b based upon the disappearance of C-F stretching peaks and evidence by the decrease in the advancing water contact angle from the original fluorinated monolayer of $121° \pm 1°$ down to $52° \pm 4°$ for the hydrolyzed (or cleaved) HOC_6S/Au. We hypothesize that ethanol enhances the successful penetration of the hydroxide ion through the bulky fluorocarbon groups by opening up the structure of the fluorinated SAM over that observed with water. Not only would ethanol help to open up the structure of the fluorinated SAM for penetration of the

hydroxide ion, but ethanol would also solvate the product of the hydrolysis (or cleavage) better than water would.
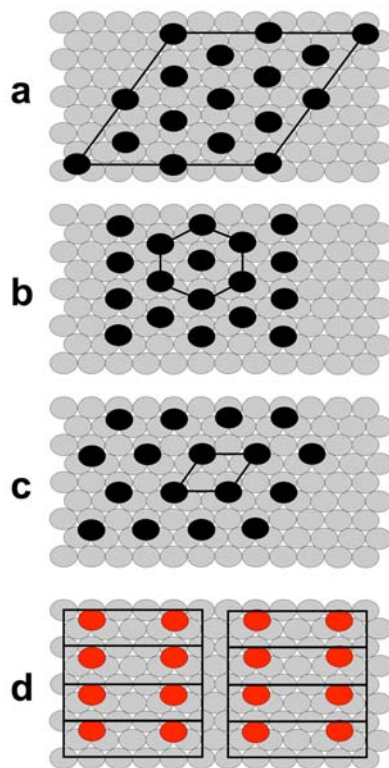
Figure 5.3. Representation of the tail group lattice structures of (a) $F_9O_2C_{11}S$/Au with c (7 x 7) lattice (b) estimated $HOC_{11}S$/Au with typical ($\sqrt{3}$ x $\sqrt{3}$) R 30° (c) $F_9O_2C_6S$/Au with p (2 x 2) lattice (d) HOC_6S/Au with p (4 x $\sqrt{3}$) lattice with the red circles representing the sulfur atom instead of the tail group as observed in (a) through (c).

In order to confirm that a hydroxyl monolayer is still left on the surface after exposure to the ethanolic KOH solution, we exposed the hydrolyzed (or cleaved) surface to a pentadecafluorooctanoyl chloride ($C_7F_{15}COCl$) solution, which in essence reverses the reaction and recaps the exposed hydroxyl groups with an ester linkage to a fluorocarbon chain through an acylation[24, 25] reaction. Figure 5.4 displays the RAIR

spectra of a bare gold substrate (left in ethanol 6 days after gold evaporation), a regular HOC$_6$S/Au substrate, and a cleaved HOC$_6$S/Au substrate after exposure to a 10 mM C$_7$F$_{15}$COCl solution with 12.5 mM pyridine in dichloromethane for 2 h. The bare gold substrate, which likely contained a small amount of hydroxyl groups from the ethanol exposure on the surface, exhibited a very small amount of fluorocarbon modification on the surface as evidenced by the small peaks at 1249 cm^{-1} and 1222 cm^{-1}; however, the advancing water contact angle of 74° ± 1° does not indicate any significant fluorocarbon modification of the gold substrate. After modification of the regular HOC$_6$S/Au substrates (where regular denotes as prepared from HS(CH$_2$)$_6$OH) with C$_7$F$_{15}$COCl, we observed a significant increase in the C-F stretching region, an increase in the advancing water contact angle to 102° ± 2°, and the appearance of carbonyl stretching at 1781 cm^{-1} which indicates a partial capping of the hydroxyl groups by reaction with the fluorinated acid chloride. When both the cleaved HOC$_6$S/Au and HOC$_{11}$S/Au substrates were modified with C$_7$F$_{15}$COCl, the C-F and carbonyl stretching peaks were evident indicating the formation of a fluorocarbon-modified monolayer after capping of the surface hydroxyl groups. This modification is also indicated by the increase in the advancing water contact angle to 120° ± 1° for the recapped cleaved HOC$_6$S/Au surface. The functionalizable hydroxyl density for the cleaved SAMs is comparable to that for a regular hydroxyl-terminated SAM, although chain flexibility and terminal group reorganization likely affects the extent of functionalization.
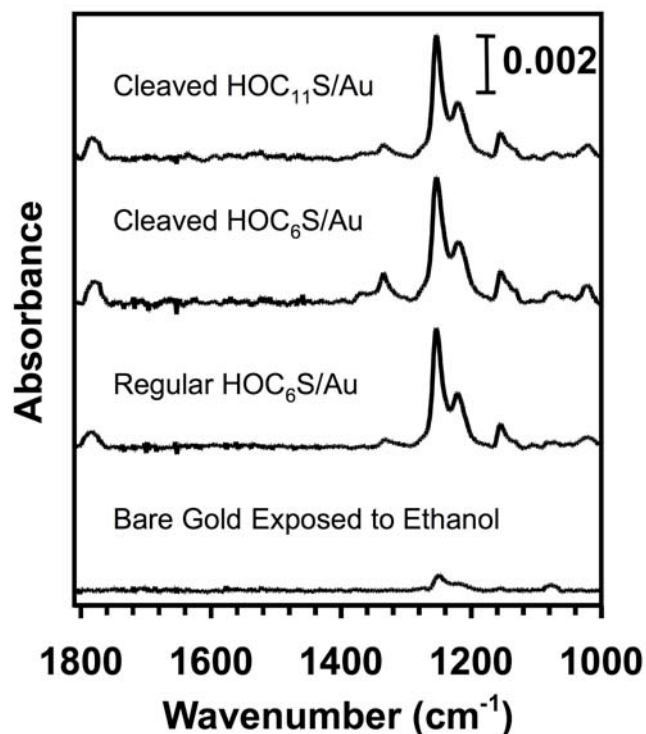
Figure 5.4. RAIR spectra of bare Au (after 6 days of exposure to ethanol), HOC_6S/Au, cleaved HOC_6S/Au, and cleaved $HOC_{11}S/Au$ substrates after exposure to 10 mM pentadecafluorooctanoyl chloride in dichloromethane with 12.5 mM pyridine for 2 h.

Structural Comparison of Cleaved Versus Regular HOC_6S/Au Monolayers

Cleaved and regular HOC_6S/Au monolayers are expected to have different structures. These different structures arise because the mechanisms involved in the process of adsorption differ substantially between a regular HOC_6S/Au monolayer and a cleaved monolayer. SAMs are formed upon the transition from a physisorbed, "lying down," phase to a chemisorbed, oriented phase. For normal long-chained alkanethiols, the thiolate is initially physisorbed onto the surface with the hydrocarbon chain parallel to the surface. Once the thiolate has physisorbed to the gold surface, the chemisorption process occurs and the energy for the formation of the gold-sulfur bond is approximately

130

44 to 45 kcal/mol[26, 27] (141 kJ/mol).[28] Once the sulfur atom has bonded to the metal, the chain-chain interactions of the thiolate only contribute $\sim$ 1.0 kcal/mol[26] ($\sim$ 6.2 kJ/mol per CH_2 unit)[28] of stabilization to the SAM for each methylene group. Some of the factors that influence the molecular structure of short-chained hydroxyl-terminated SAMs include the lack of stability of the monolayer itself due to weak van der Waals interactions between adjacent hydrocarbons, and the dramatic role of interchain hydrogen-bonding interactions on packing. In these SAMs, the formation of hydrogen bonding between adjacent hydroxyl moieties, at approximately 15 kJ/mol,[28] combined with some lateral van der Waals interactions, overrules the formation of densely packed domains at early times and results in a more tilted alkyl chain with a prevalent stripe structure on the surface, as proposed by Tsukamoto et al.[28] (Figure 5.3d). In contrast, the structure of the cleaved monolayers is controlled by the initial adsorption and packing of the fluorinated ester constituent, and hydrogen-bonding interactions only affect the structure of the cleaved film. Once the fluorocarbon groups are cleaved and assuming the resulting groups do not diffuse on the surface, the spacing of the tail groups of $F_9O_2C_6S/Au$ as shown in Figure 5.3c would approximate the spacing of the sulfur atoms in the cleaved HOC_6S/Au monolayer. Thus, the cleaved monolayer appears to have a higher surface density of adsorbates than regular HOC_6S/Au monolayers as shown by comparison of Figures 5.3c and 5.3d.

The higher surface density of cleaved HOC_6S/Au monolayers can be inferred by comparing the charge transfer resistances of the regular and cleaved HOC_6S/Au monolayers in a solution of 1 mM ferricyanide ($Fe(CN)_6^{3-}$), 1 mM ferrocyanide ($Fe(CN)_6^{4-}$), and 0.1 M Na_2SO_4 as shown in Table 5.2. The charge transfer resistance of

the regular HOC_6S/Au film to the oxidation/reduction of $Fe(CN)_6^{4-/3-}$ is nearly two orders

of magnitude lower than that for the cleaved HOC_6S/Au. Using the two charge transfer

resistances of the regular and cleaved HOC_6S/Au films, we can estimate the amount of

fractional area of uncovered metal surface $(1-\theta)$, introduced by surface defects within the

SAM, from a microelectrode array model described by Finklea[29] and written as:

$$1 - \theta = \frac{R_{Au}}{R_{SAM}} \qquad\qquad (5\text{-}1)$$

where R_{Au} is the resistance for uncoated gold (13.8 $\Omega \cdot cm^2$) and R_{SAM} is the charge

transfer resistance provided by the SAM. As seen in Table 5.2, the resistance to charge

transfer for the regular HOC_6S/Au film is 81.2 $\Omega \cdot cm^2$ while that of the cleaved

HOC_6S/Au film is 5.12 x 10^3 $\Omega \cdot cm^2$, which corresponds to a fractional area of uncovered

gold surface as 0.17 and 0.0027, respectively. This estimate is in good agreement with

the ease of penetration of $Fe(CN)_6^{4-/3-}$ through the striped structure of the regular

HOC_6S/Au film as opposed to the structure of the cleaved HOC_6S/Au film. The cleaved

HOC_6S/Au film provides a better barrier to the penetration of the redox probe due to its

collapsed structure and higher density of adsorbates.

However, the capacitance of the film, which is affected by water/ion uptake

within the monolayer, is almost 2 times lower for the regular HOC_6S/Au monolayer than

the cleaved HOC_6S/Au monolayer. The lower capacitance for the regular HOC_6S/Au

monolayer suggests that the stripe structure does not allow extensive penetration by water

and ions into the actual stripe region whereas the disordered structure of the cleaved

HOC_6S/Au film does.

The structural differences between the cleaved and regular HOC$_6$S/Au films have a pronounced effect on their rate of exchange upon exposure to C$_{22}$SH. As shown in Figure 5.2, a 10 min exposure of the cleaved HOC$_6$S/Au film to C$_{22}$SH in an aqueous C$_{12}$E$_5$ micellar solution results in a successful place exchange. The positions of the asymmetric and symmetric methylene stretching vibrations at 2920 cm^{-1} and 2852 cm^{-1}, respectively, as well as the asymmetric and symmetric methyl stretching vibrations at 2966 cm^{-1} and 2880 cm^{-1}, respectively, indicate that the C$_{22}$S/Au SAM, formed after displacing the cleaved HOC$_6$S/Au hydroxyl-terminated monolayer, has few gauche defects and is nearly trans-extended after only 10 min. This can also be observed by the 74% decrease in capacitance of the backfilled cleaved film over the cleaved film as shown in Table 5.2, which is a result of an increase in film thickness. In contrast, exposure of a regular HOC$_6$S/Au monolayer to C$_{22}$SH in C$_{12}$E$_5$(aq) for 10 min provides only a partial exchange, resulting in a poorly crystalline C$_{22}$S/Au film (Figure 5.2e), as evidenced by positions of the asymmetric and symmetric methylene stretching vibrations at 2930 cm^{-1} and 2859 cm^{-1}, respectively. The lack of clearly defined asymmetric (unobserved) and symmetric methyl stretching (barely observed at 2882 cm^{-1}) vibrations indicate that the terminal methyl groups are disordered and sparse and reflect an unsuccessful exchange of the regular HOC$_6$S/Au film by C$_{22}$SH. This can also be reflected in the minimal increase of the advancing water contact angle from 43° to 66°, which is in contrast to the increase (from 52° to 111°) observed upon backfilling cleaved HOC$_6$S/Au films with C$_{22}$SH as shown in Table 5.2. These conclusions are also confirmed by the lack of a dramatic increase in resistance or decrease in capacitance for

the regular HOC_6S/Au film after exchange with $C_{22}SH$ as shown in Figure 5.5 and Table 5.2. The differences in the exchange of regular and cleaved HOC_6S/Au substrates likely reflect the differences in structures of the two films. One explanation is that the loose, disordered structure of the cleaved HOC_6S/Au film may aid in the partitioning of the $C_{22}SH$ near the gold surface, effectively increasing its concentration well above that in solution. The incomplete nature of the regular HOC_6S/Au film does not offer such a partitioning effect although it does provide available electrode space for $C_{22}SH$ to assemble in between the stripes. Displacement of the ordered stripe structures must be rate-limiting here.

Because we have observed an increased rate of backfilling for cleaved monolayers over regular hydroxyl-terminated monolayers, we have utilized this feature to successfully backfill PSI-SAM modified substrates and limit the amount of exposure time of the protein to the competing thiol and corresponding solution.
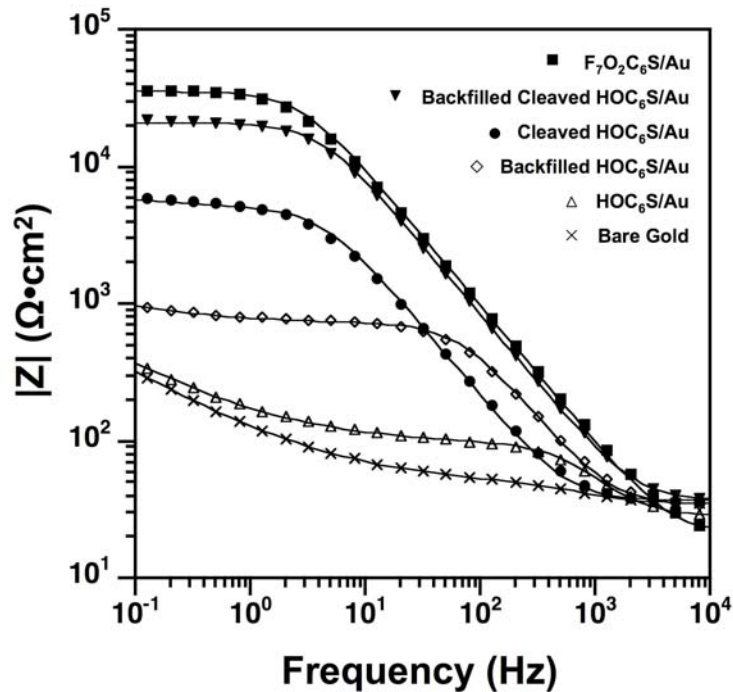
Figure 5.5. Electrochemical impedance spectra in the form of Bode plots for the indicated films upon exposure to 1 mM $K_3Fe(CN)_6$ and 1 mM $K_4Fe(CN)_6$ with 0.1 M $Na_2SO_4(aq)$. Solid curves represent fits of the experimental results by an equivalent circuit model.

Table 5.2. Film resistance, capacitance, Warburg, and contact angles of cleaved and regular HOC_6S/Au monolayers with various modifications.

Monolayer	Advancing Water Contact Angle (°)	Log [Rfilm (Ω/cm^2)]	Capacitance $(\mu F/cm^2)$	Log [Warburg $(\Omega\,sec^{-1/2})$]
$F_7O_2C_6S/Au$	121 ± 1	4.23 ± 0.18	2.26 ± 0.32	
Cleaved HOC_6S/Au	52 ± 4	3.71 ± 0.14	7.02 ± 1.20	
Backfilled 10 min $C_{22}SH$-Cleaved HOC_6S/Au	111 ± 2	4.32 ± 0.28	1.83 ± 0.20	
HOC_6S/Au	43 ± 2	1.91 ± 0.05	3.98 ± 0.10	2.40 ± 0.02
Backfilled 10 min $C_{22}SH$-HOC_6S/Au	66 ± 17	2.68 ± 0.29	3.48 ± 0.52	2.40 ± 0.02

PSI Adsorption onto SAMs: Effect of Chain Length and Density

To investigate the effect of interfacial density on the adsorption of PSI, we prepared regular and cleaved HOC_6S/Au and $HOC_{11}S/Au$ monolayers and exposed them to a solution of PSI for 24 h. As discussed in the preceding section, the interfacial density of the cleaved film is greater than that of the regular film for n = 6; however, the density of the cleaved film is less than that of the regular film for n = 11 because $HOC_{11}SH$ forms a densely packed SAM. Figure 5.6 shows RAIR spectra of the amide region, which indicates similar extents of PSI adsorption on the cleaved and regular SAMs of constant chain length but a 3-fold enhancement in PSI adsorption onto the thinner (n = 6) SAMs. These results suggest that PSI adsorption is insensitive to the structural differences within the regular versus cleaved SAMs but is strongly dependent on the chain length of the adsorbate comprising the SAM.

In order to more thoroughly probe the effects of hydrocarbon chain length on PSI adsorption, we have exposed a solution of PSI to SAMs formed from a series of regular hydroxyl-terminated ω-alkanethiols (HOC_nSH (n = 2, 4, 6, 8, 11)) as well as a hydrophilic piranha cleaned bare gold substrate. Figure 5.7 shows that the thickness of the PSI decreases sharply as the chain length (n) increases, from 40 Å for n = 2 to 10 Å for n = 11, in agreement with our findings for the cleaved SAMs.
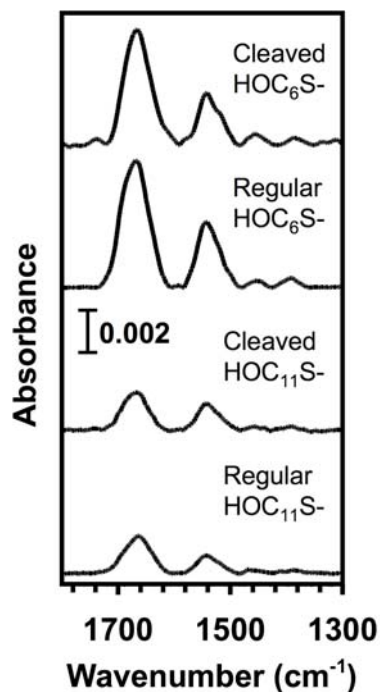
Figure 5.6. RAIR spectra of the Amide I and II bands of PSI after 24 h adsorption on cleaved and regular HOC_6S/Au and $HOC_{11}S/Au$ monolayers.

The additional PSI adsorption onto shorter-chained, hydroxyl-terminated SAMs can possibly be attributed to enhanced interactions with the underlying gold, changes in the film crystallinity, and/or changes in the surface energy as n is decreased. Based upon our earlier work in examining PSI adsorption onto mixed $HO-/CH_2-$ terminated SAMs, we observed that the adsorbed amount reaches a maximum at an intermediate surface energy corresponding to an advancing water contact angle of $\sim 50°$.[11] To assess the surface energies of the films in this study, we measured the advancing water contact angles (θ_a) for the series of hydroxyl-terminated ω-alkanethiols (HOC_nS/Au) on gold. The trend of adsorbed PSI thickness in Figure 5.7 does not correlate with the surface wettability as evidenced by C_{11} ($\theta_a = 22° \pm 3°$) $<< C_8$ ($56° \pm 2°$) $< C_4$ ($< 15°$) $\approx C_6$ ($43° \pm 2°$) $< C_2$ ($< 15°$). We hypothesize that van der Waals forces between the gold and the

137

protein (through the SAM) can also influence the adsorption of PSI onto the various surfaces.
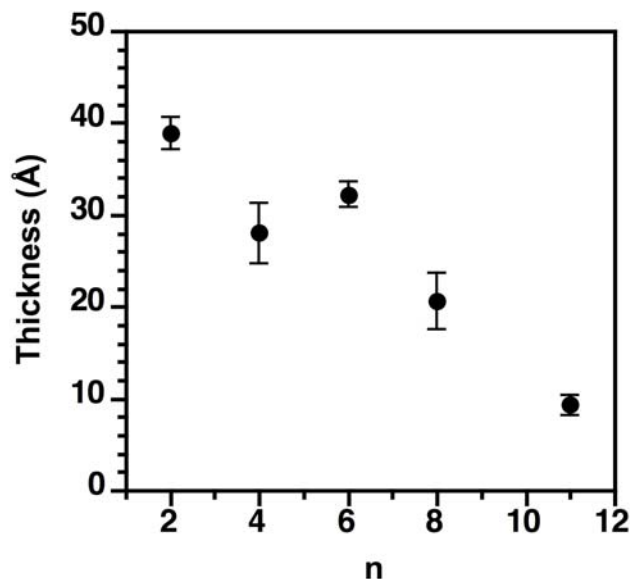
Figure 5.7. SE thicknesses of PSI upon 24 h adsorption on HOC_nS/Au at 4°C.

Van der Waals forces are known to influence interfacial properties such as wettability. Miller and Abbott[30] suggested that changes in contact angles of SAMs prepared from varying hydrocarbon chain lengths of n-alkanethiols ($CH_3(CH_2)_mSH$, $2 < m < 17$) on gold, copper, and silver were not due to changes in the crystallinity or packing density of the SAMs as the hydrocarbon chain length decreases, but rather, due to the van der Waals forces acting between the substrate and the fluid (through the SAM). To support this conclusion, Miller and Abbott[30] used Lifshitz theory to predict the effect of changes in contact angles as a function of chain length with an assumption that the chain length affected the thickness of the SAM but not its structure. For hydroxyl-terminated SAMs, however, Tsukamoto et al.[28] recently demonstrated that the typical ($\sqrt{3} \times \sqrt{3}$) R30°

structure was unobservable for HSC_6OH, HSC_4OH, and HSC_3OH on gold substrates as discussed in the preceding section. Instead, Tsukamoto et al.[28] observed that the structure of short-chained mercapto-alcohols is largely dictated by the formation of hydrogen bonding. For short-chained hydroxyl-terminated ω-alkanethiols on gold, the hydrocarbon chains are forced to lay almost parallel to the gold surface to accommodate the influence of strong hydrogen bonding. Tsukamoto et al.[28] observed that the hydrogen bonding of the hydroxyl moieties dictate the sulfur lattice spacing of these monolayers, such that the shorter the hydrocarbon backbone, the closer the sulfur atoms must be to allow for hydrogen bonding between adjacent adsorbates. Figure 5.3d demonstrates the sulfur lattice spacing of a HOC_6S/Au monolayer as determined by Tsukamoto et al.[28] However, we emphasize that the corrugated stripe structure is not the primary reason for enhanced protein adsorption as we observe similar PSI adsorption on the cleaved HOC_6S/Au SAM that displays a more disordered packing. As a comparison, we have also examined the adsorption of PSI onto a piranha cleaned bare gold surface, which displaces organic contaminants. The amount of PSI adsorbed onto a piranha cleaned gold surface is roughly 30 Å ± 4 Å, which is similar to that observed on the HOC_4S/Au substrate. Comparing the amount of PSI that adsorbs onto a clean gold surface with that obtained on a very short-chained hydroxyl-terminated gold surface, the attraction of the gold alone on the adsorption of PSI appears to play a significant role in the mechanism of adsorption.

<u>Backfilling Around Adsorbed PSI</u>

The rapid rates of exchange of cleaved HOC_6S/Au by $C_{22}SH$ could be extremely useful in the backfilling of PSI, as described in detail in Chapter IV. Based upon the results of Chapter IV, the coverage of PSI on a HOC_6S/Au substrate can be controlled as a function of adsorption time at a dilute concentration. A sparse monolayer coverage of PSI on HOC_6S/Au allowed for ease of backfilling of the inter-protein spaces with $C_{22}SH$ from an ethanolic solution. When backfilling PSI-modified cleaved HOC_6S/Au monolayers with $C_{22}SH$ from $C_{12}E_5(aq)$, the inter-protein spaces can be successfully backfilled within 10 min, based on RAIR and electrochemical impedance spectra. This is a significant reduction in the time for backfilling regular HOC_6S/Au substrates as seen in Chapter IV. Figure 5.8 illustrates good crystallinty in the backfilled $C_{22}S/Au$ SAM based on the positions of the methylene asymmetric (2920 cm^{-1}) and symmetric (2852 cm^{-1}) stretching vibrations and suggests an oriented monolayer based on the appearance of strong asymmetric (2966 cm^{-1}) and symmetric (2879 cm^{-1}) methyl stretching peaks. The electrochemical impedance spectra (Figure 5.9) indicate significant changes in the middle-to-high frequency region upon backfilling PSI-modified cleaved HOC_6S/Au. These changes translate into a reduction in film capacitance by 42% due to the effective increase in film thickness and accompanying reduction in dielectric constant as short hydroxyl-terminated adsorbates are replaced by long-chain C_{22} adsorbates. The backfilling has minimal effect on film resistance as the defect density is undoubtedly high between adsorbed PSI and the $C_{22}S/Au$ chains. On average the amount of loss of PSI upon exposure to $C_{22}SH$ in $C_{12}E_5$ (aq) is approximately 19 % as estimated from the loss in intensity of the Amide I band. We observe similar losses in PSI when $C_{22}SH$ is not

present (Chapter IV). Therefore, this loss from the surface is not a result of interactions of $C_{22}SH$ with PSI, but rather the result of exposure to the nonionic surfactant $C_{12}E_5$ that presents a more favorable environment for PSI.

When backfilling around PSI adsorbed onto regular HOC_6S/Au substrates, although the surface density of thiolates on the surface is less than that of the cleaved HOC_6S/Au substrates, $C_{22}SH$ only moderately backfills the substrate. (Figure 5.8) This modest backfill is consistent with that observed in the absence of PSI (Figure 5.2e) and may reflect that $C_{22}SH$ cannot penetrate the hydrogen-bonded arrays of thiolates.
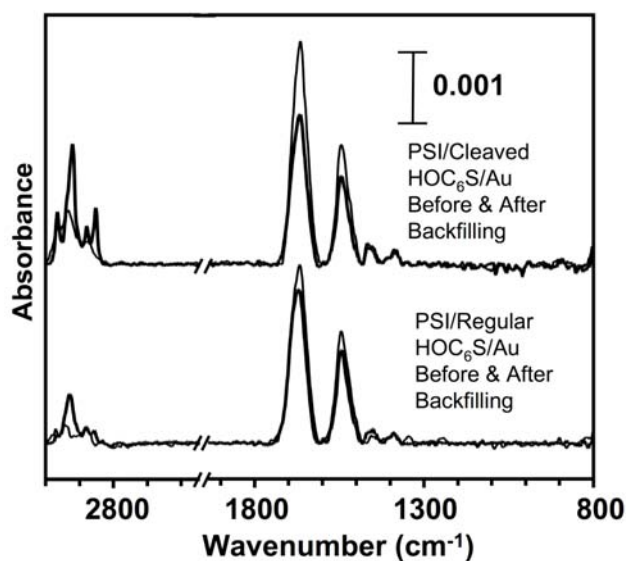
Figure 5.8. RAIR spectra of a cleaved HOC_6S/Au substrate with PSI before (faint line top) and after (dark line top) backfilling with $C_{22}SH$ from $C_{12}E_5$ (aq) for 10 min and a regular HOC_6S/Au substrate with PSI before (faint line bottom) and after (dark line bottom) 10 min backfilling with $C_{22}SH$ from $C_{12}E_5$ (aq). The spectra are offset for clarity.
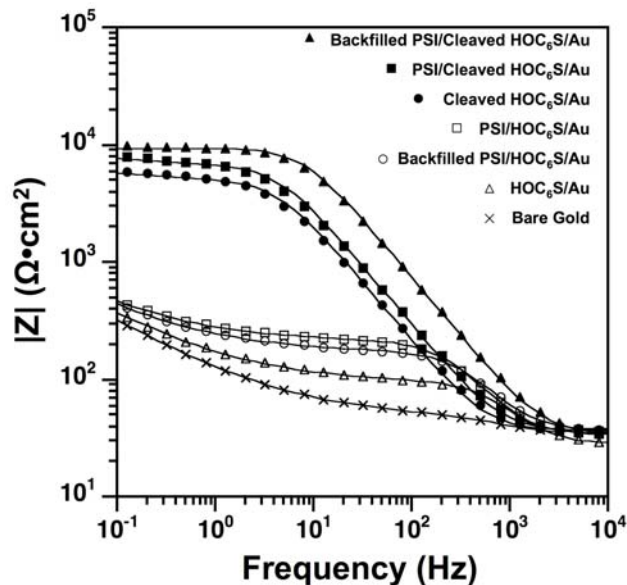
Figure 5.9. Electrochemical impedance spectra in the form of Bode plots for the indicated films upon exposure to 1 mM $K_3Fe(CN)_6$ and 1 mM $K_4Fe(CN)_6$ with 0.1 M Na_2SO_4(aq). Solid curves represent fits of the experimental results by an equivalent circuit model.

Table 5.3. Film capacitance, resistance, Warburg, and contact angles of PSI-modified cleaved and regular HOC_6S/Au monolayers with various modifications.

Monolayer	Advancing Water Contact Angle (°)	Log Rfilm (Ω/cm^2)	Capacitance ($\mu F/cm^2$)	Log [Warburg ($\Omega\,s^{-1/2}$)]
PSI/Cleaved HOC_6S/Au	61 ± 2	3.78 ± 0.18	5.45 ± 0.30	
Backfilled 10 min C_{22}SH- PSI/Cleaved HOC_6S/Au	87 ± 2	3.97 ± 0.10	2.26 ± 0.08	
PSI/HOC_6S/Au	62 ± 1	2.28 ± 0.04	4.12 ± 0.06	2.37 ± 0.005
Backfilled 10 min C_{22}SH- PSI/HOC_6S/Au	66 ± 3	2.12 ± 0.02	3.90 ± 0.02	2.38 ± 0.007

Conclusions

      We have prepared a HOC_6S/Au monolayer through base-mediated hydrolysis of an ester-linked fluorocarbon terminal group, and this cleaved monolayer exhibits a higher surface density of thiolates than regular HOC_6S/Au monolayers and demonstrates that the exchange of thiolates is not simply controlled by the surface density of pre-adsorbed thiolates, but rather the molecular structure. The resulting cleaved HOC_6S/Au films have a slightly lower surface energy than those of regular HOC_6S/Au films and a loss of regularity in molecular structure, which aids in the successful backfilling of a longer methyl-terminated ω-alkanethiol ($C_{22}SH$). We have also demonstrated that, as it applies to an integral membrane protein surrounded by a nonionic surfactant, the presence of a loosely packed monolayer structure does not, by itself, contribute to an increase in PSI adsorption. We have also observed that for the surfactant assisted delivery of PSI, an increase in the chain length of the hydrocarbon backbone of hydroxyl-terminated ω-alkanethiols contributes to a sharp decrease in the amount of PSI adsorbed and may be due to increased van der Waals interactions between the gold substrate and the protein. Successful backfilling and/or place exchange of the cleaved HOC_6S/Au monolayer with and without adsorbed PSI occurs within 10 min in the presence of $C_{22}SH$ in $C_{12}E_5$(aq), whereas regular HOC_6S/Au monolayers inhibit this process and are not as easily exchanged.

References

1.   Berron, B.; Jennings, G. K., Loosely Packed, Hydroxyl Terminated SAMs on Gold. *Langmuir* **2006,** submitted.

2.   Lahann, J.; Mitragotri, S.; Tran, T.-N.; Kaido, H.; Sundaram, J.; Choi, I. S.; Hoffer, S.; Somorjai, G. A.; Langer, R., A Reversibly Switching Surface. *Science* **2003,** 299, (5605), 371-374.

3.   Fukushima, H.; Seki, S.; Nishikawa, T.; Takiguchi, H.; Tamada, K.; Abe, K.; Colorado, R., Jr.; Graupe, M.; Shmakova, O. E.; Lee, T. R., Microstructure, Wettability, and Thermal Stability of Semifluorinated Self-Assembled Monolayers (SAMs) on Gold. *Journal of Physical Chemistry B* **2000,** 104, 7417-7423.

4.   Choi, E. J.; Foster, M. D.; Daly, S.; Tilton, R.; Przbycien, T.; Majkrzak, C. F.; Witte, P.; Menzel, H., Effect of Flow on Human Serum Albumin Adsorption to Self-Assembled Monolayers of Varying Packing Density. *Langmuir* **2003,** 19, (13), 5464-5474.

5.   Bain, C. D.; Whitesides, G. M., Formation of 2-Component Surfaces by the Spontaneous Assembly of Monolayers on Gold from Solutions Containing Mixtures of Organic Thiols. *Journal of the American Chemical Society* **1988,** 110, (19), 6560-6561.

6.   Ostuni, E.; Grzybowski, B. A.; Mrksich, M.; Roberts, C. S.; Whitesides, G. M., Adsorption of Proteins to Hydrophobic Sites on Mixed Self-Assembled Monolayers. *Langmuir* **2003,** 19, (5), 1861-1872.

7.   Capadona, J. R.; Collard, D. M.; Garcia, A. J., Fibronectin adsorption and cell adhesion to mixed monolayers of tri(ethylene glycol)- and methyl-terminated alkanethiols. *Langmuir* **2003,** 19, (5), 1847-1852.

8.   Ichii, T.; Fukuma, T.; Kobayashi, K.; Yamada, H.; Matsushige, K., Phase-Separated Alkanethiol Self-Assembled Monolayers Investigated by Non-Contact AFM. *Applied Surface Science* **2003,** 210, (1-2), 99-104.

9.   Otzen, D. E.; Oliveberg, M.; Hook, F., Adsorption of a Small Protein to a Methyl-Terminated Hydrophobic Surfaces: Effect of Protein-Folding Thermodynamics and Kinetics. *Colloids and Surfaces B-Biointerfaces* **2003,** 29, (1), 67-73.

10.   Stranick, S. J.; Atre, S. V.; Parikh, A. N.; Wood, M. C.; Allara, A. L.; Winograd, N.; Weiss, P. S., Nanometer-Scale Phase Separation in Mixed Composition Self-Assembled Monolayers. *Nanotechnology* **1996,** 7, 438-442.

11.   Ko, B. S.; Babcock, B.; Jennings, G. K.; Tilden, S. G.; Peterson, R. R.; Cliffel, D.; Greenbaum, E., Effect of Surface Composition on the Adsorption of Photosystem I onto Alkanethiolate Self-Assembled Monolayers on Gold. *Langmuir* **2004,** 20, (10), 4033-4038.

12.   Park, J.-S.; Smith, A. C.; Lee, T. R., Loosely Packed Self-Assembled Monolayers on Gold Generated from 2-Alkyl-2-Methyl Propane-1,3-Dithiols. *Langmuir* **2004,** 20, 5829-5836.

13.   Choi, E. J.; Foster, M. D., The Role of Specific Binding in Human Serum Albumin Adsorption to Self-Assembled Monolayers. *Langmuir* **2002,** 18, (2), 557-561.

14.   Weinstein, R. D.; Moriarty, J.; Cushnie, E.; Colorado, R.; Lee, T. R.; Patel, M.; Alesi, W. R.; Jennings, G. K., Structure, Wettability, and Electrochemical Barrier Properties of Self-Assembled Monolayers Prepared from Partially Fluorinated Hexadecanethiols. *Journal of Physical Chemistry B* **2003,** 107, (42), 11626-11632.

15.   Schonherr, H.; Vancso, G. J., *AFM Study on Lattice Orientation and Tribology of SAMs of Fluorinated Thiols and Disulfides on Au(111): The Influence of the Molecular Structure*. ACS Symposium Series: 2001; Vol. 787, p 15-30.

16.   Bandrup, J.; Immergut, E. H., *Polymer Handbook*. Third ed.; John Wiley & Sons: New York, NY, 1989; p Section V, page 16.

17.   Wang, J.; Kenseth, J. R.; Jones, V. W.; Green, J.-B. D.; McDermott, M. T.; Porter, M. D., SFM Tip-Assisted Hydrolysis of a Dithiobis(succinimidoundecanoate) Monolayer Chemisobred on a Au(111) Surface. *Journal of the American Chemical Society* **1997,** 119, 12796-12799.

18.   Amado, E.; Kressler, J., Synthesis and Hydrolysis of α-ω-Perfluoroalkyl-Functionalized Derivatives of Poly(ethylene oxide). *Macromolecular Chemical Physics* **2005,** 206, 850-859.

19.   Kutsuna, T. U.; Chandra, A. K.; Sugie, M.; Sekiya, A., Effect of Fluorine Substitution on the Rate for Ester Hydrolysis: Estimation of the Hydrolysis Rate of Perluoroalkyl Esters. *Journal of Molecular Structure: THEOCHEM* **2003,** 635, (1-3), 83-89.

20.   Bilkadi, Z.; de Lorimier, R.; Kirsch, J. F., Secondary alpha-Deuterium Kinetic Isotope Effects and Transition-State Structures for the Hydroylsis and Hydrazinolysis Reactions of Formate Esters. *Journal of the American Chemical Society* **1975,** 97, (15), 4317-4322.

21.   Jencks, W. P.; Gilchrist, M., Nonlinear Structure-Reactivity Correlations. The Reactivity of Nucleophilic Reagents towards Esters. *Journal of the American Chemical Society* **1968,** 90, (10), 2622-2637.

22.   Dordi, B.; Schonherr, H.; Vancso, G. J., Reactivity in the Confinement of Self-Assembled Monolayers: Chain Length Effects on the Hydroylsis of N-Hydroxysuccinimide Ester Disulfides on Gold. *Langmuir* **2003,** 19, 5780-5786.

23.   Frey, S.; Heister, K.; Zharnikov, M.; Grunze, M.; Tamada, K.; Colorado, R., Jr.; Graupe, M.; Shmakova, O. E.; Lee, T. R., Structure of Self-Assembled Monolayers of Semifluorinated Alkanethiols on Gold and Silver Substrates. *Israel Journal of Chemistry* **2000,** 40, 81-97.

24.   Brantley, E. L.; Jennings, G. K., Fluorinated Polymer Films from Acylation of ATRP Surface-Initiated Poly(Hydroxyl Methacrylate). *Macromolecules* **2004,** 37, (4), 1476-1438.

25.   Engquist, I.; Lestelius, M.; Liedberg, B., Microscopic Wettability of Ester- and Acetate-Terminated Self-Assembled Monolayers. *Langmuir* **1997,** 13, 4003-4012.

26.   Dubois, L. H.; Nuzzo, R. G., Synthesis, Structure, and Properties of Model Organic-Surfaces. *Annual Review of Physical Chemistry* **1992,** 43, 437-463.

27.   Nuzzo, R. G.; Zegarski, B. R.; Dubois, L. H., Fundamental-Studies of the Chemisorption of Organosulfur Compounds on Au(111) - Implications for Molecular Self-Assembly on Gold Surfaces. *Journal of the American Chemical Society* **1987,** 109, (3), 733-740.

28.   Tsukamoto, K.; Kubo, T.; Nozoye, H., Structure of Mercaptoalcohol Self-Assembled Monolayers on Au(111). *Applied Surface Science* **2005,** 244, 578-583.

29. Finklea, H. O., *Electrochemistry of Organized Monolayers of Thiols and Related Molecules on Electrodes*. Marcel Dekker: New York, 1996; Vol. 19, p 109-335.

30. Miller, W. J.; Abbott, N. L., Influence of van der Waals Forces from Metallic Substrates on Fluids Supported on Self-Assembled Monolayers Formed from Alkanethiols. *Langmuir* **1997,** 13, 7106-7114.

VOLTAMMETRIC STUDIES OF PHOTOSYSTEM I DIRECT
ELECTROCHEMISTRY

Introduction

In plants and cyanobacteria, photosynthesis relies on many proteins that enable

electron transfer, such as cytochromes, photosystems, and iron-sulfur systems. The

Photosystem I (PSI) protein complex transfers electrons unidirectionally across the

thylakoid membrane. Within PSI, the electron transfer occurs across multiple redox

centers, from the photoexcited P700 center, a specialized chlorophyll a dimer, to iron-

sulfur clusters ($F_X/F_A/F_B$) terminating at the F_B cluster.[1, 2]

PSI exhibits photodiode characteristics and thus is good candidate for the newly

developing field of nanoscale or molecular electronics,[3] due to its small size and the

ability to isolate it from an abundant and renewable source. The electrons flow from

P700 to F_B, and these sites could be interfaced with metal electrodes[4] to create

nanocircuits. Thus, understanding and controlling the electrochemistry of these two

redox centers of PSI is crucial.

The well known "Z-scheme" presents the standard reduction potentials for the

electrochemically active centers involved in photosynthesis, including the PSI-bound

centers.[1, 2] None of the values reported in the Z-scheme have been measured directly

with the use of electrochemistry, but were either determined with electron paramagnetic

resonance (EPR), spectroelectrochemistry, or estimated.[5] These potential values can

change as the conditions surrounding the protein complex are modified: different

detergents used for the isolation of PSI will lead to different standard potentials.[2, 6] However, reported potentials for the most important PSI electron carriers are dispersed around the following values (V vs normal hydrogen electrode, NHE): + 0.50 for P700, -1.00 for A_0, -0.80 for A_1, -0.73 for F_X, -0.59 for F_A, and -0.53 for F_B.[2, 5]

The direct electrochemistry of a PSI center, either as a part of the thylakoid membrane[7, 8] or isolated[9] in solution, has been demonstrated previously without clearly identifying either redox site. The photocatalytic behavior of PSI was studied,[7-9] proving that PSI can be electrochemically active in solution, but no direct measurement of the reduction potentials of the redox sites involved in photocatalysis was shown. A couple of recent papers present direct electrochemistry data for PSI. Kievit and Brudvig[6] reported the reduction potential for the P700 center (+0.49 vs NHE), while no mention of the other redox centers was made; the PSI complex was adsorbed onto Au electrodes modified with either sodium thioglycolate or dithiodipyridine. Munge et al.[10] assigned peaks for A_1 (-0.54 vs NHE) and the F_A/F_B centers (-0.19 vs NHE), but the P700 center was not visible, although the potential window was scanned in the region where this center should be present; the PSI complex was trapped in a lipid film deposited onto graphite electrodes.

The study of the PSI electrochemistry when the protein is embedded in the thylakoid membrane (where all PSI centers have the same orientation)[1] is problematic because the membrane/electrode interface is not as well characterized as the alkanethiol/Au interface, for example. Either all donor or all acceptor sites of the proteins embedded in the thylakoid membrane are possibly within electron transfer distance to the underlying electrodes, but not both, so that the studied configuration is

149

undetermined (i.e., the solution will contain many membrane parts, and it is impossible to assess how many membrane parts are at the electrode and what is the configuration for each of them). Good electronic communication to this membrane is not assured by physical overlay with the electrode. As opposed to the thylakoid membrane, the PSI centers can freely rotate in a solution to bring both sites within electron transfer distances at an electrode. However, proteins typically adsorb onto bare electrodes in a random orientation and aggregate or denature on the electrode surface.[6] To solve this issue, the electrode can be modified such that the protein will orient on its surface in a known configuration. For example, Au electrodes modified with particular ω-alkanethiols selectively adsorb and orient PSI.[11-13]

Figure 6.1 displays a schematic for the ideal PSI orientations that would enable the study of the P700 and the F_A/F_B centers. The Au electrode is modified with a self-assembled monolayer (SAM) that directs the adsorption of PSI into a known configuration as a function of the terminal group X.[11, 12] PSI must have either the donor side (Figure 6.1a, for the study of P700) or the acceptor side (Figure 6.1b, for the study of F_A/F_B) in contact with the modified surface of the electrode to undergo a redox reaction, giving rise to appropriate oxidative and reductive currents in a voltammogram. In the absence of light, there is no electron transfer across PSI from P700 to F_B, and thus we are able to study the electrochemistry of the specified centers. In this chapter, we present both the direct electrochemistry of PSI (PSI 40),[14] with the identification of the P700 and the F_A/F_B centers, as well as the direct photoelectrochemical properties of this protein complex after immobilization on a SAM-modified Au substrate.
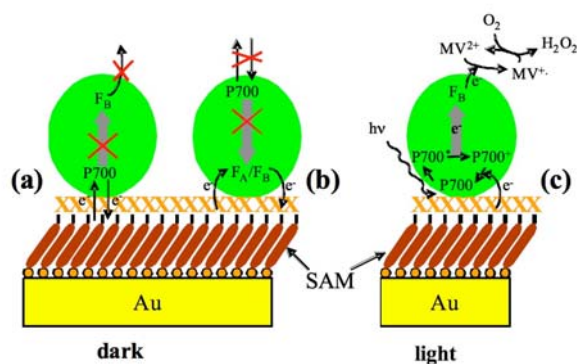
Figure 6.1. Schematic of electron transfer associated with PSI; in the dark, the electrochemistry of both P700 (a) and F_A/F_B (b) centers can be studied; in the light, in the presence of an electron acceptor (MV^{2+}), all electron transfer sites are active (c).

Results and Discussion

Direct Electrochemistry

We have performed cyclic voltammetry (CV) and square wave voltammetry (SWV) experiments of the PSI centers stabilized in aqueous solution by 1 mM Triton X-100 surfactant and adsorbed to the surface using hydroxyl-terminated thiol (HSC_6OH or HSC_8OH) SAMs on Au disk electrodes. According to Lee et al.,[13] the adsorption of PSI onto a hydroxyl surface should result in approximately 70% of the PSI complexes oriented with the P700 center closest to the electrode (Figure 6.1a), and the remaining 30% in other unknown configurations. Table 6.1 presents the different SAMs that we have investigated for the direct electrochemistry. The best results were obtained for SAMs derived from HSC_6OH and HSC_8OH. Different terminal groups were used as controls since they either did not allow PSI adsorption (HSC_5CH_3)[12] or did not orient PSI in a favorable manner for our studies (HSC_2COOH,[13] tiopronin). SAMs prepared from

151

other hydroxyl-terminated thiols did not yield distinguishable electrochemical signals for PSI. The short-chained monolayers (HSC_2OH, HSC_4OH) were likely too disorganized and the long-chained monolayers ($HSC_{11}OH$) might have been too insulating to allow for efficient electron transfer to the reaction centers of PSI.

Table 6.1. SAMs tested for PSI signal and experimentally determined P700/P700$^+$ redox potential.

SAM Type	PSI signal higher than background?	E_{P700} (V vs NHE)
HSC_2OH	No	-
HSC_2COOH	No	-
HSC_4OH	No	-
HSC_5CH_3	No PSI adsorption	-
HSC_6OH	Yes	$+0.51 \pm 0.03$
Tiopronin	No	-
HSC_8OH	Yes	$\sim +0.5$
$HSC_{11}OH$	No	-

The P700 center clearly shows reversible electrochemical behavior. Table 6.2 compares our values obtained for PSI/HOC$_6$S/Au electrodes with the literature data available for P700 and F_A/F_B from EPR spectroelectrochemistry[2] and electrochemistry.[6,10] These values can change as the conditions surrounding the protein complex are modified: different detergents used for the isolation of PSI will lead to different standard potentials possibly because the number of available components involved in the electron transfer process can vary from detergent to detergent.[2, 6] Our value for the P700 center (+0.51 V vs NHE) is in good agreement with the EPR data[2] and with the findings of Kievit and Brudvig[6] who have recently reported direct physisorbed electrochemistry in which the P700 center was moderately stable, and the F_B center was not observed. Their reported reduction potential for P700 is +0.49 V vs NHE.[6]

Table 6.2. Comparison of experimental results ($E_{1/2}$ for PSI/HOC$_6$S/Au electrodes) with E^0 literature values (all values are in V vs NHE).

Active Center	EPR (Literature)	Electrochemistry (Literature)	CV (Experimental Results)*	SWV (Experimental Results)
P700	+0.50	+0.49	+0.51 ± 0.03	+0.48 ± 0.06
F$_A$/F$_B$	-0.59(F$_A$)/-0.53(F$_B$)	~ -0.19	N/A	Anodic: -0.28 ± 0.05
				Cathodic: -0.45 ± 0.07
				Average: -0.36 ± 0.05

* All experimental values are averaged for at least five different runs, and the results presented were obtained for at least two different PSI extractions.

By comparison to the results in Figure 6.2b, the CV peaks for P700 from Kievit and Brudvig are barely discernible; however, they present a baseline corrected SWV where the P700 peaks are visible. The difficulty in observing clear PSI-related peaks in their experiments reflects a lack of oriented connectivity to the P700 redox center. Our method of studying the direct electrochemistry of the P700 center improves the magnitude of the recorded signal and clearly demonstrates reversible CV peaks for P700/P700$^+$. We have obtained the same results as those presented in Figure 6.2 for different electrodes and different PSI extractions. The peak potential values displayed in Figure 6.2 are part of the averaged values presented in Table 6.2. For the control experiments where no PSI was present, we did not observe the peaks we display for PSI in Figure 6.2. Actually, for the control experiments (no PSI) the signal was not higher than the background.

We have also observed an enhanced electrochemical signal for the P700 center on PSI/HOC$_8$S/Au electrodes (Figure 6.3). We were not able to employ the background subtraction technique as described in Figure 6.2, since in the case of the HSC$_8$OH SAM the PSI peaks were not well defined compared to the background. Figure 6.3 displays the
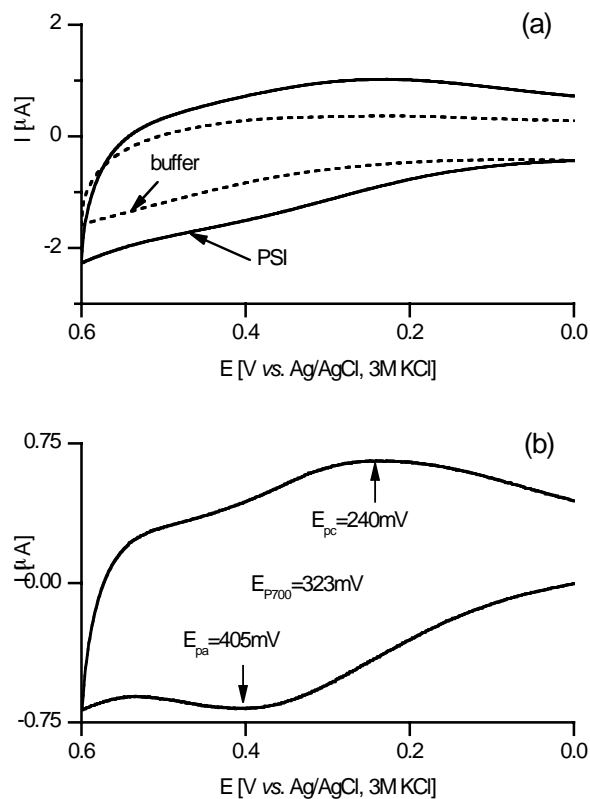
Figure 6.2. (a) CVs of PSI solution (solid line) and of buffer with no PSI (dashed line) for a HOC$_6$S/Au electrode (for the solid line CV the electrode was exposed overnight to the PSI solution; for the dashed line the CV was taken prior to immersing in PSI). The buffer is 200 mM phosphate, pH 7.0, with 1 mM Triton X-100. (b) CV corrected for background was obtained from the curves displayed in (a): solid - dashed line and shows the direct electrochemistry of PSI. Au disk working electrode area was 0.03 cm^2.

PSI CVs for three different electrodes (solid lines), and the signal is reproducible from one electrode to another. The differences between the PSI runs and the control (buffer) runs are (1) for the controls, the electrodes were immersed overnight in buffer with no PSI (200 mM phosphate, pH 7.0, 1 mM Triton X-100), while the electrodes for the PSI CVs were immersed overnight in PSI solutions (2) the control CVs were obtained in plain buffer (200 mM phosphate, pH 7.0, 1 mM Triton X-100), whereas the PSI CVs were

obtained in PSI solution. The PSI signal is consistently higher for the PSI runs vs the controls. Since the only difference between the PSI and the control runs is the presence of the protein, based on the results for the HSC_6OH SAM, the enhanced signal for the HSC_8OH SAM in Figure 6.3 results from the $P700/P700^+$ redox reactions. While we cannot clearly identify the $P700/P700^+$ peaks on the voltammograms, probably because of the slower electron transfer kinetics through the thicker SAM, the SAM derived from HSC_8OH presents itself as potentially useful for practical applications, since it forms a more ordered monolayer than the HSC_6OH monolayer. The non-Faradaic current is smaller at the HOC_8S/Au electrode than the HOC_6S/Au electrode, suggesting that the blocking behavior of the HOC_8S/Au monolayer implies a more organized SAM.
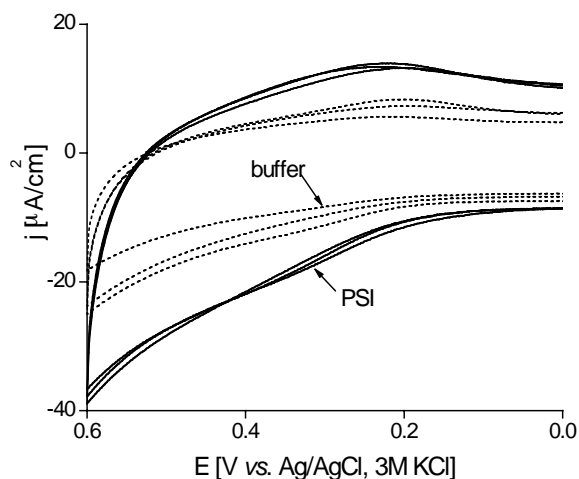

Figure 6.3. CVs of PSI solution (solid line) and of buffer with no PSI (dashed line) for different HOC_8S/Au electrodes (for the solid line CV the electrodes were exposed overnight to the PSI solution; for the dashed line CV the electrodes were exposed overnight to buffer). The buffer is 200 mM phosphate, pH 7.0, with 1 mM Triton X-100. The signal for PSI is consistently higher than the one for the buffer. Au disk working electrode areas were 0.03 cm^2.

The SWVs for the PSI/HOC$_6$S/Au electrodes also demonstrate reversible peaks for P700/P700$^+$ upon background subtraction (similar to the one preformed for the results displayed in Figure 6.2). In the SWVs for the buffer runs (dashed lines, Figures 6.4a and 6.4b), we can observe the Au oxide peak near the P700 peak. Although these two peaks are close, the P700 peak can still be distinguished since the PSI signal is more intense. The peak potential values displayed in Figure 6.4 are part of the averaged values in Table 6.2. For the control experiments where no PSI was present, we did not observe the peaks we display for PSI in Figure 6.4 since the background was not lower than the control signal. The peaks at -0.3/-0.5 V vs NHE are reproducible and likely to be the F$_A$/F$_B$ active centers; they are small in comparison reflecting the dominant orientation of P700 near the electrode surface. As a molecular diode, PSI does not permit reverse orientations (Figure 6.1b) from the remaining 30% of the PSI protein complexes. The peak seen at -0.5 V vs NHE (Figure 6.4d) is very close to the edge of the solvent window, and its appearance is possibly due to a very slight shift in the potential window (e.g., a slight shift in the reference potential). However, when the controls are run we cannot observe the peak at -0.3 V vs NHE (Figure 6.4c). For the F$_A$/F$_B$ voltammetric peaks, the separate identification of each component is not possible. The peaks in Figure 6.4c-d appear as a consequence of a redox process involving F$_A$ or F$_B$ individually. These iron-sulfur clusters are so closely spaced with respect to their standard reduction potentials as to appear together according to Rusling et al.[10] They assigned CV and SWV peaks for F$_A$/F$_B$ (-0.19 V vs NHE) but were not able to distinguish between different iron-sulfur clusters. Their reported values differ by 400 mV from the values obtained with spectroelectrochemical titrations (Table 6.2).[2] This probably results from the

composition of the electrolyte solution in which their measurements were performed and from PSI being trapped in a lipid film at the surface of the electrode. In their work, there is no sign of P700, although the electrochemistry is performed in a potential window that would allow for a P700 signal. Our method allows for observation of both the P700 and the F_A/F_B peaks on the same SWV plot.
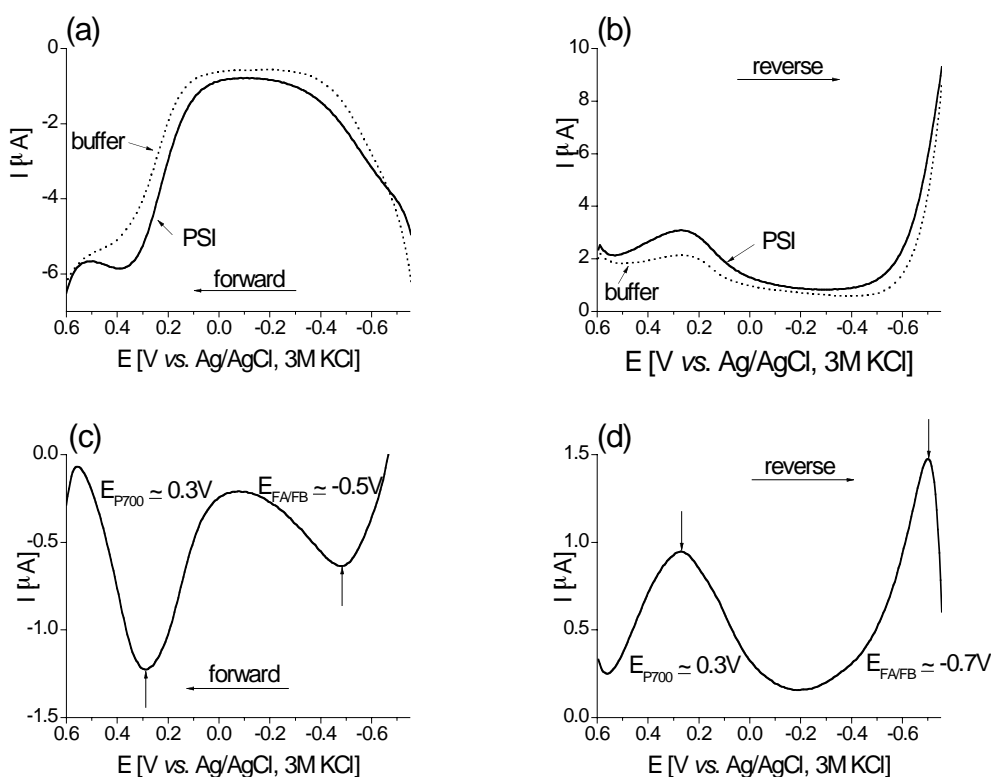

Figure 6.4. (a) Forward and (b) reverse scan SWVs of PSI solution (solid line) and of buffer with no PSI (dashed line) for a HOC_6S/Au electrode (for the solid line SWV the electrode was exposed overnight to the PSI solution; for the dashed line the SWV was taken prior to immersing in PSI). The buffer is 200 mM phosphate, pH 7.0, 1 mM Triton X-100. (c) Forward and (d) reverse scan SWVs corrected for background were obtained from the corresponding curves displayed in (a) and (b) solid – dashed line and they show the direct electrochemistry of PSI. Au disk working electrode area was 0.03 cm^2.

Photocatalysis

Under illumination of PSI, photons induce electron-hole pair separation resulting in a reduced F_B acceptor site and oxidized $P700^+$ donor site so that these sites will be available for direct electron transfer (Figure 6.1c). Once the P700 center is photoexcited, an electron will transfer to the F_B end and out of the PSI. Methyl viologen (MV^{2+}) is an electron acceptor compatible with the F_B center in PSI.[15] Bourdillon et al.[9] have demonstrated that in the presence of MV^{2+} as an electron scavenger, there is a light-controlled electrocatalytic coupling between PSI and cytochrome. Figure 6.1c diagrams the expected photoelectron transfer reactions involving the P700 center. A new electron must transfer to the oxidized $P700^+$ center before the PSI can be re-excited by another photon. In the presence of light, an oxidized $P700^+$ in the active PSI complex will draw electrons from the electrode, leading to an increased electrode current that corresponds to the reduction of the $P700^+$ center.

In Figure 6.5, a larger reduction current was observed for the $P700^+$ center with red light in the presence of MV^{2+}, indicating a rapid turnover of the PSI reaction centers. The potential was set at +0.1 V vs Ag/AgCl, 3 M KCl so that this potential would be outside the Faradaic reduction potentials for MV^{2+} and thus the reduction current observed was only for the $P700^+$ center on the electrode surface. Figure 6.1c diagrams the expected process in the presence of a compound that is a compatible electron acceptor for PSI (e.g., MV^{2+}).[9] In the light, the P700 center gets excited and one electron is transferred across PSI to the F_B center, where it is picked up by MV^{2+}. The presence of the oxygen in solution assures that the electron scavenger (MV^{2+}) is recycled and available for the next electron pickup from PSI. The Au electrode will transfer one

electron to the P700$^+$ center resulting in a reduction current. The PSI clearly shows a photoenhanced current for the P700$^+$ reduction. Controls using similar conditions, except for the protein component, (HOC$_6$S/Au) (Figure 6.5) display only a slight variation in current due probably to the light affecting the underlying metal electrode. A clear, stable photoenhanced current appears only when PSI is present. Figure 6.1c implies that the observation of an increased current is not possible unless the solution contains an electron acceptor compatible with PSI. Figure 6.6 demonstrates that in the absence of MV^{2+} no increase in current can be observed, even if all other conditions are met: PSI adsorbed and oriented on a HOC$_6$S/Au electrode, red light excitation, and the potential for the working electrode (+0.1 V vs Ag/AgCl, 3 M KCl) set such that we would observe electrochemically the reduction of the P700$^+$ center. These experiments demonstrate that we can successfully direct the orientation of PSI on a modified Au electrode while preserving its photoactivity and photodiode characteristics.
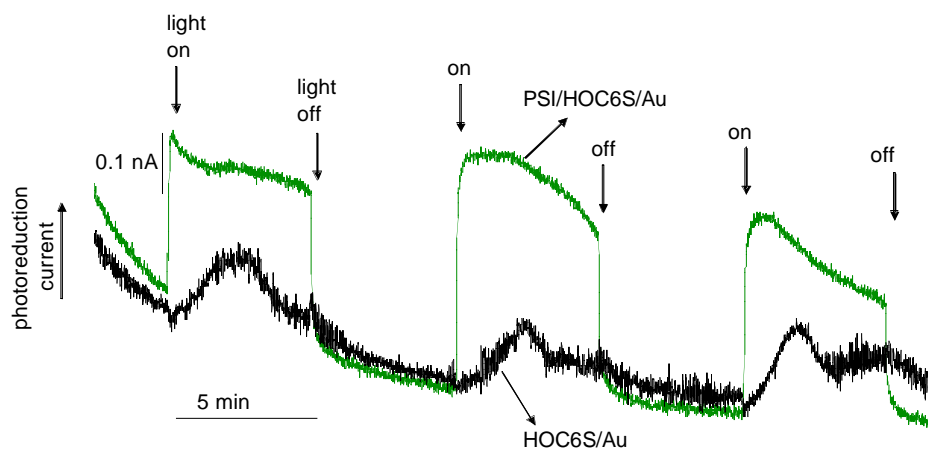
Figure 6.5. Chronoamperometry of PSI/HOC$_6$S/Au (top curve; this electrode was exposed overnight to PSI solution in elution buffer: 200 mM phosphate, pH 7.0, 1 mM Triton X-100) and HOC$_6$S/Au (bottom curve; this electrode was exposed overnight to elution buffer) electrodes in buffer (50 mM phosphate, pH 7) containing 250 μM MV^{2+}. The potential was set at +0.1 V *vs.* Ag/AgCl, 3 M KCl. Au disk WE area was 0.03 cm^2. The electrodes were illuminated with a 250 W cold light lamp through a red filter. Results obtained by Dr. Ciobanu.
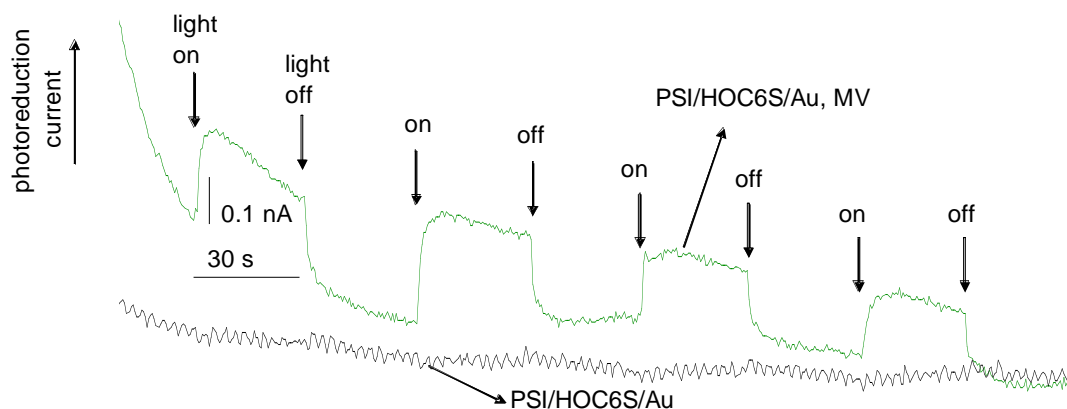
Figure 6.6. Chronoamperometry of PSI/HOC$_6$S/Au electrodes in buffer (50 mM phosphate, pH 7). Only the top curve has 250 μM MV^{2+} present in the solution. The potential was set at +0.1 V *vs.* Ag/AgCl, 3 M KCl. Au disk WE area was 0.03 cm^2. The electrodes were illuminated with a 250 W cold light lamp through a red filter. Results obtained by Dr. Ciobanu.

Conclusions

The use of a HOC_6S/Au SAM for PSI adsorption and orientation allows for the identification of both the P700 and the F_A/F_B peaks on the same voltammogram. The corresponding potentials, E_{P700} = +0.51 V vs NHE and E_{F_A/F_B} = -0.36 V vs NHE are in good agreement with the literature. Although the HOC_8S/Au SAM does not allow for the identification of the PSI active centers on voltammograms, this SAM presents itself as potentially useful for energy conversion applications since it is a more ordered monolayer than the HSC_6OH SAM and still allows for electron transfer into the P700 of PSI immobilized on a surface. We have demonstrated that the PSI complex retains its photoactivity upon immobilization on a SAM-modified Au substrate, opening a whole new possibility for photoelectrochemical devices.

References

1.   Garrett, R. H.; Grisham, C. M., *Biochemistry*. Saunders College Publishing: Forth Worth, 1999.

2.   He, W. Z.; Malkin, R., *Photosynthesis*. 1998; p 29-43.

3.   Das, R.; Kiley, P. J.; Segal, M.; Norville, J.; Yu, A. A.; Wang, L.; Trammell, S. A.; Reddick, L. E.; Kumar, R.; Stellacci, F.; Lebedev, N.; Schnur, J.; Bruce, B. D.; Zhang, S.; Baldo, M., Integration of Photosynthetic Protein Molecular Complexes in Solid-State Electronic Devices. *Nano Letters* **2004,** 4, (6), 1079-1083.

4.   Evans, B. R.; O'Neill, H. M.; Hutchens, S. A.; Bruce, B. D.; Greenbaum, E., Enhanced Photocatalytic Hydrogen Evolution by Covalent Attachment of Plastocyanin to Photosystem I. *Nano Letters* **2004,** 4, (10), 1815-1819.

5.   Chitnis, P. R., Photosystem I: Function and Physiology. *Annual Review of Plant Physiology and Plant Molecular Biology* **2001,** 52, 593-596.

6.   Kievit, O.; Brudvig, G. W., Direct Electrochemistry of Photosystem I. *Journal of Electroanalytical Chemistry* **2001,** 497, (1-2), 139-149.

7.   Agostiano, A.; Goetze, D. C.; Carpentier, R., Cyclic Voltammetry Measurements of the Photoelectrogenic Reactions of Thylakoid Membranes. *Photochemistry and Photobiology* **1992,** 55, (3), 449-455.

8.   Agostiano, A.; Goetze, D. C.; Carpentier, R., Photoelectrochemistry of Thylakoid and Sub-Thylakoid Membrane Preparations - Cyclic Voltammetry and Action Spectra. *Electrochimica Acta* **1993,** 38, (6), 757-762.

9.   Proux-Delrouyre, V.; Demaille, C.; Leibl, W.; Sétif, P.; Bottin, H.; Bourdillon, C. J., Electrocatalytic Investigation of Light-Induced Electron Transfer Between Cytochrome c_6 and Photosystem I. *Journal of American Chemical Society* **2003,** 125, (45), 13686-13692.

10.   Munge, B.; Das, S. K.; Ilagan, R.; Pendon, Z.; Yang, J.; Frank, H. A.; Rusling, J. F., Electron Transfer Reactions of Redox Cofactors in Spinach Photosystem I Reaction Center Protein in Lipid Films on Electrodes. *Journal of American Chemical Society* **2003,** 125, (41), 12457-12463.

11.   Ciobanu, M.; Kincaid, H. A.; Jennings, G. K.; Cliffel, D. E., Photosystem I Patterning Imaged by Scanning Electrochemical Microscopy. *Langmuir* **2005,** 21, 692-698.

12.   Ko, B. S.; Babcock, B.; Jennings, G. K.; Tilden, S. G.; Peterson, R. R.; Cliffel, D.; Greenbaum, E., Effect of Surface Composition on the Adsorption of Photosystem I onto Alkanethiolate Self-Assembled Monolayers on Gold. *Langmuir* **2004,** 20, (10), 4033-4038.

13.   Lee, I.; Lee, J. W.; Greenbaum, E., Biomolecular Electronics: Vectorial Arrays of Photosynthetic Reaction Centers. *Physical Review Letters* **1997,** 79, (17), 3294-3297.

14.   Lee, I.; Lee, J.; Stubna, A.; Greenbaum, E., Measurement of Electrostatic Potentials above Oriented Single Photosynthetic Reaction Centers. *Journal of Physical Chemistry B* **2000,** 104, 2439-2443.

15.   Fujii, T.; Yokoyama, E.-i.; Unoue, K.; Sakurai, H., The Sites of Electron Donation of Photosystem I to Methyl Viologen. *Biochimica Et Biophysica Acta* **1990,** 1015, 41-48.

CHAPTER VII

CONCLUSIONS AND FUTURE WORK

Conclusions

The work presented herein demonstrates fundamental aspects towards incorporation of Photosystem I (PSI) into a photoelectrochemical device including the guided direction of PSI adsorption, direct electrochemistry, entrapment, and photocatalysis on a surface.

Based upon previous work at Vanderbilt, PSI was successfully patterned on a surface through microcontact printing of self-assembled monolayers (SAMs) on gold. By patterning alternating chemical functionality on a substrate, PSI selectively adsorbed to regions of high-energy surface as opposed to low-energy surface. Because the substrates consisted of opposing chemical functionalities, such as hydroxyl- (high-energy) and methyl-terminal (low-energy) groups, scanning electrochemical microscopy (SECM) was used to image the substrates based upon changes in conductivity of the substrate after each modification.

The successful direct electrochemistry of PSI, in the dark, proved to depend on the chain length of hydroxyl-terminated SAM used to immobilize PSI on the substrate. Direct electron transfer occurred when the hydroxyl-terminated monolayer was of intermediate chain length (n = 6 to 8 methylene units), but not when the monolayer was short (n = 2, 4) due to monolayer disorder or long (n = 11) due to increased distances for electron tunneling. In particular, the use of a HOC_6S/Au SAM allowed for the

identification of both the P700 and F_A/F_B corresponding potentials, $E_{P700} = +0.51$ V vs NHE and $E_{F_A/F_B} = -0.36$ V vs NHE, respectively, and were in good agreement with literature values.

The electrochemistry or photocatalysis of PSI, in the light, demonstrated the transfer of electrons through PSI on a substrate to the solution-phase electron acceptor methyl viologen. Under illumination of red light, photon induced electron-hole pair separation in PSI resulted in the transfer of an electron from the P700 center through the protein to the F_B end and on to an artificial electron acceptor, methyl viologen, which is compatible with the F_B center in PSI. Importantly, these results demonstrate the conversion of light to current by an immobilized monolayer of PSI to achieve a current density of $3 - 6$ nA/cm^2.

In order to suppress the amount of background current and entrap PSI on the substrate, mimicking the thylakoid membrane of plants, PSI atop HOC_6S/Au was backfilled by exposure to a solution containing a long-chain alkanethiol from both organic solvents and aqueous micellar solutions. The incoming alkanethiol filled the inter-protein spaces providing hydrophobic stabilization of the physically adsorbed PSI. The integral membrane protein, PSI, was resistant to denaturation even upon exposure to organic solvents.

Disorganized hydroxyl-terminated SAMs were designed by adsorbing partially fluorinated disulfides to the gold surface and then hydrolytically cleaving away the fluorocarbon tail group. The use of hydroxyl-terminated surfaces with different packing densities did not enhance PSI adsorption; however, varying the packing density of the hydroxyl-terminated monolayer did provide an enhanced rate of backfilling by

165

docosanethiol. The amount of PSI adsorbed onto hydroxyl-terminated surfaces was enhanced as the chain length of the alkanethiol was reduced, reflecting the likely importance of van der Waals interactions between PSI and the gold substrate through the intervening SAM.

Future Work

Platinization of PSI Immobilized on a Substrate and Connectivity with a Conductive Polymer

The steps discussed throughout this work prove that PSI is active after immobilization on a gold substrate. In order to complete the circuit of the photoelectrochemical device shown in Figure 1.4, the top of PSI or the F_B end must be physically connected to a conductive material. Greenbaum and co-workers have demonstrated that Pt, Os, Ru, and Ir can be photoreduced onto the reducing sites of PSI complexes that were free in solution.[1] They demonstrated the ability to photoreduce protons and produce H_2 at these metallic sites.[2] While this demonstrates the successful platinization of PSI from solution, the platinization of PSI complexes immobilized on a substrate has not yet been established. However, progress in the Cliffel lab with atomic force microscopy (AFM) images is promising and suggests that the platinization of PSI immobilized on a substrate can be accomplished.

Once platinization of PSI is achieved, the next step for completion of the circuit is to coat the top with a conductive polymer that could then be easily integrated with a hardware connection. Polyaniline (PANI) is a conductive polymer that is transparent in the visible wavelength region and reflective in the infrared wavelength region. For future

work, the incorporation of PANI with a transparent indium-tin-oxide layer could lead to multiple layers and increased currents.

Covalent Attachment of PSI at Surfaces

The master's work of Brian Babcock,[3] examined the covalent attachment of PSI on a surface. The strategy involved binding lysine residues of PSI, some of which are exposed near the P700 reaction center, through an amide linkage with an acid-terminated monolayer that is pre-reacted with N-hydroxysuccinimide (NHS). Reaction of this NHS ester with PSI results in covalent attachment. From Babcock's work, the covalent attachment of PSI through NHS chemistry dramatically stabilizes the secondary structure of PSI. However, because of the significant number of lysine residues in PSI, the actual control over the binding events is limited. Evans et al.[4] suggest that covalent attachment methods increase the photocatalytic hydrogen evolution of PSI in solution.

By using various covalent attachment methods, that are not restricted to the linkage of lysine residues, the percentage of PSI complexes whose electron transfer vectors are randomly oriented on the surface could possibly be reduced and the stability of PSI on the surface could likely be increased. An alternative covalent attachment method using a Traut's reagent (2-iminothiolane hydrochloride) can be used to convert primary amines of PSI to thiol groups that can chemically adsorb onto gold without using a SAM, which could eliminate the effects of electron transfer decay and tunneling issues associated with the use of a SAM. Frolov et al.[5] demonstrated that attachment of cyanobacterial PSI directly to the Au surface through the sulfur bond found in cysteine residues did not modify the photochemical properties of PSI. The number of cysteine

167

residues in the *PsaA* and *PsaB*[6] components are significantly reduced as compared to the number of lysine residues, which could lead to better targeting and well defined control of adsorption and orientation.

<u>Immobilization and Entrapment of PSI on a Surface through Langmuir-Blodgett Films</u>

This dissertation demonstrated the successful entrapment of PSI immobilized on a substrate through the backfilling of inter-protein void spaces with a longer-chained alkanethiol. An alternative to this would be the entrapment of PSI on a surface within a Langmuir-Blodgett (LB) film. Using LB films, PSI is not exposed to solvents after being immobilized on the surface and the entrapment of PSI is created in a single step. LB films can also mimic the thylakoid membrane environment that houses PSI naturally on a surface.

<u>Spectroelectrochemistry of PSI Immobilized on Optically Transparent Electrodes</u>

In Chapter VI, the photocatalysis of PSI immobilized on Au substrates in the presence of an artificial electron acceptor, methyl viologen, was demonstrated. Methyl viologen itself is photoactive and results in the creation of a radical species that can be observed with a peak at 399 nm and a band around 601 nm under a nitrogen environment.[7, 8] With appropriate controls, the kinetics of electron transfer from PSI to methyl viologen could be examined through the use of spectroelectrochemistry, where ultra-violet/visible spectra are collected along with the electrochemical data. An optically transparent electrode, created by the evaporation of a very thin layer of gold, will allow for the optical monitoring of electron transfer events. Methyl viologen has been

demonstrated to insert itself within SAM modified electrodes,[9] and this possibility should be further investigated for the monitoring of methyl viologen interactions with PSI on SAMs.

References

1.   Lee, J. W.; Collins, R. T.; Greenbaum, E., Molecular Ionic Probes: A New Class of Hill Reagents and Their Potential for Nanofabrication and Biometallocatalysis. *Journal of Physical Chemistry B* **1998,** 102, 2095-2100.

2.   Lee, J. W.; Lee, I.; Laible, P. D.; Owens, T. G.; Greenbaum, E., Chemical Platinization and its Effect on Excitation Transfer Dynamics and P700 Photooxidation Kinetics in Isolated Photosystem I. *Biophysical Journal* **1995,** 69, 652-659.

3.   Babcock, B. D. Immobilization of Photosystem I onto Gold Surfaces: An Analysis by Fourier Transform Infrared Spectroscopy. Master's Thesis, Vanderbilt University, Nashville, 2001.

4.   Evans, B. R.; O'Neill, H. M.; Hutchens, S. A.; Bruce, B. D.; Greenbaum, E., Enhanced Photocatalytic Hydrogen Evolution by Covalent Attachment of Plastocyanin to Photosystem I. *Nano Letters* **2004,** 4, (10), 1815-1819.

5.   Frolov, L.; Rosenwaks, Y.; Carmeli, C.; Carmeli, I., Fabrication of a Photoelectronic Device by Direct Chemical Binding of the Photosynthetic Reaction Center Protein to Metal Surfaces. *Advanced Materials* **2005,** 17, (20), 2434-2437.

6.   Wilma Kirsch; Seyer, P.; Herrmann, R. G., Nucleotide Sequence of the Clustered Genes for Two P_{700} Chlorophyll *a* Apoproteins of the Photosystem I Reaction Center and the Ribosomal Protein S14 of the Spinach Plastid Chromosome. *Current Genetics* **1986,** 10, 843-855.

7.   Shah, S. S.; Amin, S.; Nazir, M. Y. K., Micellar Effect of Anionic, Cationic, and Nonionic Surfactants on Electron Transfer Process of Methylviologen Measured by UV-Visible Spectroscopy. *Journal of the Chemical Society of Pakistan* **2003,** 25, (4), 276-280.

8.   Alam, M. M.; Ito, O., Self-Repairing Photosensitized Electron Transfer from Thiones to Methyl Viologen in Aqueous Media. *Journal of Physical Chemistry A* **1999,** 103, 1306-1310.

9.   John, S. A.; Ohsaka, T., Stabilization of the Assemblies of Short Chain Alkyl Chain Asymmetric Viologens on Alkanethiol-Coated Electrodes. *Electrochimica Acta* **1999,** 45, 1127-1133.

APPENDIX A

PHOTOSYSTEM I EXTRACTION AND QUANTIFICATION METHODS

Photosystem I (PSI) Extraction

The first PSI preparation was done by Anderson and Boardman in the 1960s, but the first intact PSI centers were isolated by Mullet and co-workers in 1980 using sucrose gradient centrifugation of Triton X-100 solubilized pea thylakoid membranes. This PSI center (PSI-110) was composed of approximately 11 protein subunits and contained about 110 Chl molecules per P700. PSI-110 exhibited the 730 nm longer wavelength fluorescence maximum at 77 K, characteristic of light harvesting complex I (LHCI). After a second PSI preparation, they obtained PSI-65 which showed a maximum fluorescence emission at 77 K of about 690 nm, characteristic of reaction center I.[1] Their goal was to lower the chlorophyll-to-P700 ratio to facilitate the optical monitoring of electron carriers.[2] This is the main reason for isolation of PSI-40 which represents 40 chlorophylls to one P700 unit. In a single extraction, various ratios of chlorophyll-to-P700 can be obtained. PSI-40 can be extracted from the thylakoid membrane using the method of Reeves and Hall.[3]

The Day Before: Prep

2 buffers, 1 medium, and the spinach (All need to be stored in the fridge overnight.)

Elution Buffer: 0.2 M Phosphate Buffer pH 7.0 with TritonX-100 (0.05% wt/vol)

Na_2HPO_4 – 20.6146 g
NaH_2PO_4 – 16.9878 g
Triton X-100 – 0.5 g   in 1 L H_2O

NOTE: Triton - In order to dissolve the Triton, first dissolve the other components of the solution in water. Carefully, weigh out the Triton on the corner of a small weighing boat. Use a pipette to spray the solution onto the Triton containing weigh boat while allowing it to run into the beaker, this probably needs to be done a dozen times to get all of the Triton off the weighing boat. The weigh boat should not be soapy.

Adjust to pH 7.0 with NaOH

Column Buffer: 0.01 M Phosphate Buffer pH 7.0

Na_2HPO_4 – 1.0186 g
NaH_2PO_4 – 0.8556 g   in 1 L H_2O

Adjust to pH 7.0 with NaOH

Re-suspending Medium: 50 mM HEPES pH 7.6

Sorbitol – 6.0116 g
EDTA – 0.0584 g
$MgCl_2·6H_20$ – 0.0203 g
$MnCl_2·4H_2O$ – 0.0198 g
HEPES – 1.1915 g
Triton X-100 - 1.0 g   in 100 mL H_2O

See the note on Triton under the Elution Buffer.
Adjust to pH 7.6 with NaOH

Spinach:

All of the center veins and the major side veins should be trimmed away. Also remove any sections that are discolored or damaged.

Get the freshest baby spinach you can find. A single bag from Harris Teeter gives over forty grams when trimmed if you do not discard a lot of the spinach in the bag.

Regenerating Buffer: 0.5 M Phosphate Buffer pH 7.0

This is used to regenerate the column for reuse of the hydroxylapatite; however, we typically do not reuse the hydroxylapatite due to a slowed elution so this buffer is not necessary.

Na_2HPO_4 – 25.7347 g
NaH_2PO_4 – 21.2504 g   in 500 mL H_2O

Adjust to pH 7.0 with NaOH

The Day Of: Extraction

Grinding Medium**: pH 6.5**

Sorbitol – 18.04 g
$Na_4P_2O_7·10 H_2O$ – 1.34 g - Sodium Pyrophosphate
$MgCl_2·6 H_2O$ – 0.24 g
Sodium Ascorbic Acid – 0.11 g   in 300 mL H_2O and place in the freezer.

Adjust to pH 6.5 with HCl and place in the freezer

Hydroxylapatite Column:

The separation is performed in a 3 cm diameter jacketed column. Set this up with the pump in ice water before the hydroxylapatite is ready to pour. Replenish the ice continually so that all of the ice does not melt.

Hydroxylapatite - 15 g   in 200 mL **Column Buffer**

Gently add the column buffer to the hydroxylapatite while swirling the slurry. This is best accomplished by adding about 50 mL of column buffer at a time. Check the bottom of the flask for chunks and break them with a stir rod. Once it is homogeneous, let the gel settle and pour off the supernatant once it is clear. Resuspend and rinse the hydroxylapatite two additional times with column buffer. After the final rinse decant down to a milky white and quickly pour this slurry onto one inch of column buffer. Let the hydroxylapatite settle. Carefully pipette two full loads of the column buffer onto the column by rotating the pipette tip in a circular motion on the side walls of the column, without disturbing the top layer of the column bed, in order to rinse the column. Use a long pipette to bring the column buffer directly above the solution and slowly release the buffer; try to eliminate any force that would dent the hydroxylapatite bed. The buffer that exits the column should be at the same pH as the column buffer prepared the day before. If this did not occur, rinse the column again. Try to leave the column with as little buffer left as possible (~ 1 mm) without letting the column go dry. Wrap the column in aluminum foil to block any light.

Centrifugation:

Make sure that the centrifuge is set up to run at 4°C with the proper centrifuge tube holder installed. Centrifuge tube holder F0850 should be used initially with the larger tubes and holder F0630 is for use with the smaller tubes. The centrifuge will chill faster if the rotor is spinning instead of stationary.

The Cart:

Use the centrifuge in the Wright Lab for the extractions. This requires a cart with the following items:

> On ice in cooler
> > Centrifuge tubes, 8 large sized tubes filled with PSI and 2 empty smaller tubes.
> > Resuspending Medium
> Pipettes
> Cotton swabs
> Kimwipes
> Waste beaker

Macerating Spinach:

Remove the grinding medium from the freezer and shake it. It should be the consistency of melted snow. If there is a significant amount of ice, let it thaw a few minutes. If it is too icy the extraction may not work. Turn off the lights. The spinach leaves should be homogenized in the grinding medium when it looks like melting snow. Several quick bursts in a food processor will homogenize the spinach-grinding medium mixture.

Pass the mixture through 2 layers of cheesecloth followed by 8 layers of cheesecloth. The flask that catches the liquid should be packed on ice and able to hold over 250 mL. Squeeze the liquid out so that at least 250 mL of a green solution is obtained. Quickly add exactly 25 mL to each of the eight larger centrifuge tubes. The tubes are packed on ice and brought to the centrifuge on the cart.

The first centrifuging process in tube holder F0850 should be at 8,000 RCF for 5 seconds. As you place the tubes in the centrifuge, make sure the outsides of the tubes are dry and free from ice, using a Kimwipe. The supernatant should be poured off and the pellet resuspended in two pipette fulls (about 3 mL) of the resuspending buffer. Resuspension should be assisted with cotton swabs on a stick. Add the current contents of four of the initial centrifuge tubes to each of the two smaller tubes and make sure they have identical volumes, and are dry and free of ice before centrifuging. The second centrifuging process in tube holder F0630 should be at 20,000 RCF for 15 min. (All times start once the centrifuge speed has been reached.) The supernatant should still be dark green after this process. Use fast stop button to quickly stop the centrifuging processes. NOTE: The centrifuging step is easiest with the help of someone else who can quickly change the rotor head while another is decanting and resuspending.

Separation:

With the lights off, pipette the supernatant onto the column quickly and carefully. Add column buffer on the top of the supernatant, and try to minimize the mixing between the solutions. Run column buffer through the column until the eluant is clear. Several rinses after the eluant is colorless with column buffer are necessary because this step reduces the amount of unbound chlorophyll in the final product. Minimize the column buffer in the column and fill the column with elution buffer. When the eluant becomes green, catch the product on ice. Typically 25 mL is obtained. Pipette 1 mL of the product into microcentrifuge tubes, remembering to swirl the product frequently so that it is homogeneous as you pipette from it. Keep one of the microcentrifuge tubes in the refrigerator, and the rest should be placed into the -80°C freezer in the Stone Lab after allowing all of the tubes to equilibrate in the refrigerator at 4°C for ~ 5 min.

NOTE: PSI will denature when frozen at -20°C, so do not leave the protein in a typical freezer. Figure 1 demonstrates the effect of temperature on PSI absorption spectra.
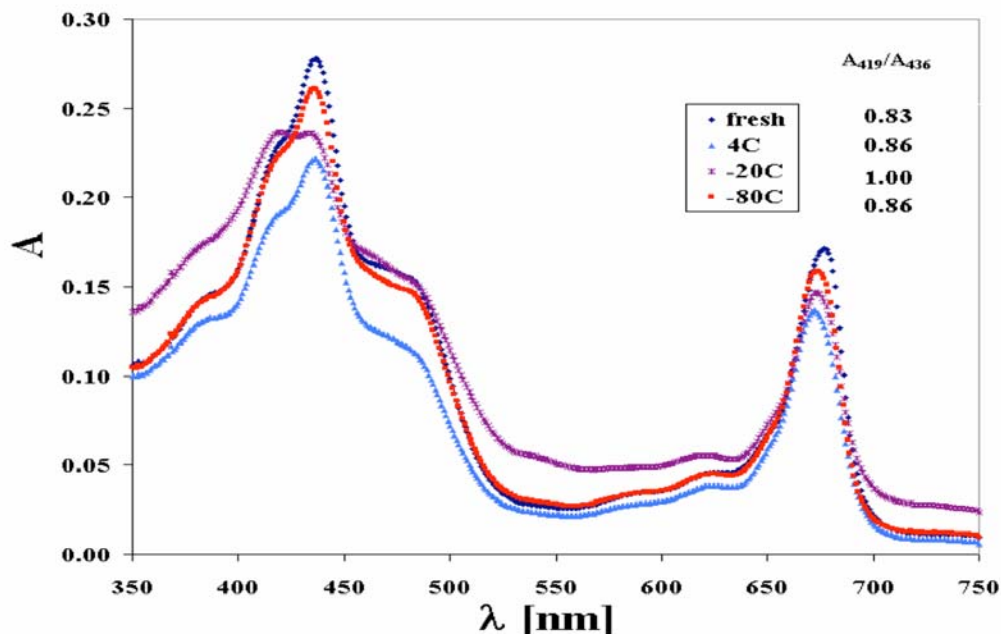
Figure 1. UV visible spectra of PSI fresh after extraction (dark blue), stored at 4°C (light blue), –20°C (purple), and –80°C (red). The ratio of absorbance at 419 nm to 436 nm (A_{419}/A_{436}) is approximately 0.83, 0.86, 1.00, and 0.86 for fresh, 4°C, –20°C, and –80°C, respectively.

The Day After: Quantification

Get to work early in order to defrost PSI from the -80°C freezer. Remove PSI from the deep freezer (-80°C) and place it in the refrigerator for 6 hours before it is ready to be used. Check the one that was left in the refrigerator over night for any separation or solids that might have crashed out of solution.

Be sure that all of the glassware, unless it is plastic, has been rinsed with acetone to remove all PSI from the last quantification. NOTE: acetone will dissolve the centrifuge tubes and the blender!

Part1 - Solutions Required:

1. 80% Acetone (High grade HPLC)/ 20% water by volume – 25 mL total

2. For the oxidation of PSI: 1 M $K_3Fe(CN)_6$ 3.293 g in 10 mL water. Wrap the solution in aluminum foil since it is light sensitive. This solution requires stirring for the salt to dissolve.

3. For the reduction of PSI: 0.5 M sodium ascorbate (not the ascorbic acid form) and 5 mM dithiothreitol (kept in the refrigerator). 0.0991g sodium ascorbate and 0.0008

175

g of dithiothreitol in 1 mL water. Wrap the solution in aluminum foil since it is light sensitive.

4.   Baba[4] Assay buffer: it is easiest to make this solution in a small beaker

50 mM Tricine	0.8959 g
0.1 M Sorbitol	1.8217 g
0.01 M NaCl	0.0585 g
0.05% Triton	0.05 g

See the note on Triton in the Elution Buffer section.

in 100 mL water adjusted to pH 7.8 with NaOH

5.   50 mM Phosphate buffer pH 7.0 – you can buy this in the stockroom. It is the normal buffer used for the standardization of a pH meter.

6.   Filter Spinach Extract.   This proves to be more difficult than one would expect. First, the lights must be off so that the PSI is not degraded. As an isolated pigment protein, PSI is light sensitive. Second, invert the microcentrifuge tube that the extract is stored and defrosted in. This is done to make sure that the solution is homogeneous. Slowly filter the PSI solution into a different microcentrifuge tube through a 0.2 μm filter obtained from Fisher. This is difficult because back-pressure builds up and some of the solution will squirt out. In order to prevent this, go very slowly, especially near the end of the filtering. Losing a few tenths of a mL does not sound bad, but because some of the material that you want to quantify remains in the filter, any additional material that you lose causes the concentration to drop. NOTE: Filtering will cause a decrease in PSI concentration regardless of how well the filtering process goes. Some of these problems were eliminated when the frit of the column was changed to a 30 mm disc with a porosity of 25-50 μm (from Ace Glass – Fritted Ware – glass disc pore C 7176-29).

The first drop or two out of the filter is clear, without chlorophyll or PSI. As you continue to pass the solution through the filter, the color will change to green. If some of the solution is lost, the final concentration will not represent a properly filtered solution, and thus is not comparable to previous work.

NOTE: Filtering was only used for electrochemistry and patterning experiments.

Part 2 – The Analysis:

PSI Absorption Spectrum

A dual beam experiment using UV-Vis from 350 – 750 nm of the PSI in phosphate buffer.

Cuvette one – the reference cuvette to be placed in the far slot – 2500 µL Phosphate buffer

Cuvette two – the sample cuvette to be placed in the nearest slot in the UV-Vis – 2450 µL Phosphate buffer and 50 µL spinach extract. Be sure to invert the solution on the way to the spectrophotometer so that it is well mixed.

Use kimwipes to make sure there are no fingerprints on the cuvettes.

NOTE: If the features do not show up in this assay, after you repeat the analysis, there is no need to continue with any other experiments.

Quantification of Chlorophyll Content

A single beam experiment using 2500 µL of Acetone/Water mixture in one cuvette and 2450 µL Acetone/ Water plus 50 µL Spinach extract in the second cuvette. Mix by inverting and use the caps or the acetone mixture will evaporate. The absorbance of these solutions needs to be compared and recorded at 645 nm, 652 nm, and 663 nm in this order. Set-up menu parameters requiring modification are: single beam, 5 replicates, and the wavelength. When the zero button is pressed it will ask for the blank, place the reference cuvette containing only the acetone/water mixture in the nearest slot to zero the absorbance. Afterwards, the sample will be requested and the reference cuvette will be replaced by the sample cuvette with the spinach extract and acetone mixture. Be sure to clean the cuvettes with Kimwipes.

According to Arnon,[5] the concentration of chlorophyll content can be determined using UV visible spectroscopy and acetone. Because each chlorophyll molecule has a different peak wavelength, we can calculate the total and individual concentrations of *Chl a* and *Chl b* by measuring the absorption of the extraction solution at three distinct wavelengths in 80% acetone and 20% water. Below are the equations used to correlate the absorption to chlorophyll content.

$$C_a = 0.0127\ A_{663} - 0.00269\ A_{645} \tag{1}$$

$$C_b = 0.0229\ A_{645} - 0.00468\ A_{663} \tag{2}$$

$$C = C_a + C_b = A_{652}\ /\ 34.5\ \text{(mg/mL)} \tag{3}$$

<u>Quantification of P700 Content</u>

A dual beam experiment using UV-Vis from 650 – 750 nm of the PSI in the BABA assay

Each cuvette should have 2275 µL of BABA assay and 100 µL of PSI. Mix by inverting. Take the scan, repeat the scan after five minutes. Add 120 µL of water to the reference cuvette. Simultaneously add 5 µL of Na-ascorbate solution to the reference cuvette and 125 µL of the potassium ferricyanide solution. Quickly invert both cuvettes and run scan. Wait 15 minutes and run the scan again. Export the 5 minute baseline and the 15 minute scan into an excel file and subtract the two runs. Take the difference between isosbestic point (725 nm) and the peak. This value and the three values from the single wavelength experiments give the chlorophyll totals and the PSI ratio.

To quantify the concentration of P700 (the active reaction center in PSI) so that we may determine the amount of chlorophyll per reaction center, we use UV visible difference spectroscopy. One cuvette contains a mixture of PSI complexes, ferricyanide, and assay buffer while the second cuvette contains a mixture of PSI complexes, sodium ascorbate, and assay buffer.[4] The difference spectrum of ferricyanide-oxidized minus ascorbate-reduced is recorded and subtracted from a background difference spectrum of solutions without the oxidizing and reducing chemicals. The red absorbance minimum for P700 is around 700 nm. To calculate the P700 concentration, the difference between the absorbance minimum around 700 nm and the absorbance corresponding to 725 nm (the isosbestic point) is determined and an extinction coefficient[6] of 64,000 M^{-1} cm^{-1} applied to quantify the concentration in the assayed solution:[7]

$$C = \frac{\Delta A}{\varepsilon * l} \quad (4)$$

where ΔA is the change in absorbance from 725 nm to 700 nm, ε is the extinction coefficient, l is the path length of cuvette, and C is the concentration.

<u>Sodium Dodecyl Sulfate (SDS) Polyacrylamide Gel Electrophoresis (PAGE) of PSI</u>

SDS-PAGE is a popular method for the separation and characterization of proteins. Shapiro et al.[8] was the first to demonstrate that the anionic detergent SDS allowed for molecular weight dependent migration through a polyacrylamide gel. Denaturing SDS-PAGE is run when the protein is denatured after heated with a thiol reagent to break apart disulfide bonds in the protein. Approximately 1.4 g of SDS to 1 g of protein leads to the assumption that the charge of the protein becomes insignificant.[9] However, membrane

proteins can cause a significant amount of error on molecular weight measurements obtained by SDS-PAGE gels.[10]

Figure 1 demonstrates the result of running a NuPAGE 4-12% Bis-Tris polyacrylamide gel, with MES running buffer, on PSI after inclusion of dithiothreitol and boiling to denature the protein. Extracts collected at various times from an extraction result in differences in the components observed in the gel. The first sample out of the hydroxylapatite column contains a large number of PSI components while each subsequent sample is reduced in the number of components.
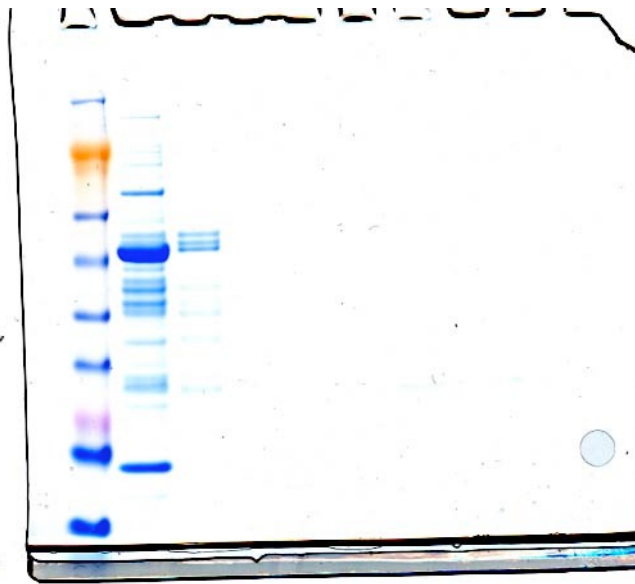
Figure 2. PSI components observed in SDS PAGE using an Invitrogen NuPAGE 4-12% Bis-Tris gel run with MES buffer without filtering the spinach extract and compared to See Blue Plus 2 MW marker (first lane). First extract sample (2nd lane), second extract sample (3rd lane). Extract samples that are not observable in the figure include samples 3-8 and correspond to lanes 4-9, however, molecular weights are approximated in Table 1.

In order to obtain molecular weights of each individual component in PSI, a Ferguson plot[9, 11] as shown in Figure 3, allows for the correlation of molecular weights of the sample from the mobility of a standard molecular weight marker, which in this case is See Blue Plus 2. The buffer used during electrophoresis influences the distance to which proteins migrate through the gel, therefore, the molecular weights of the standard will be varied depending on the buffer.
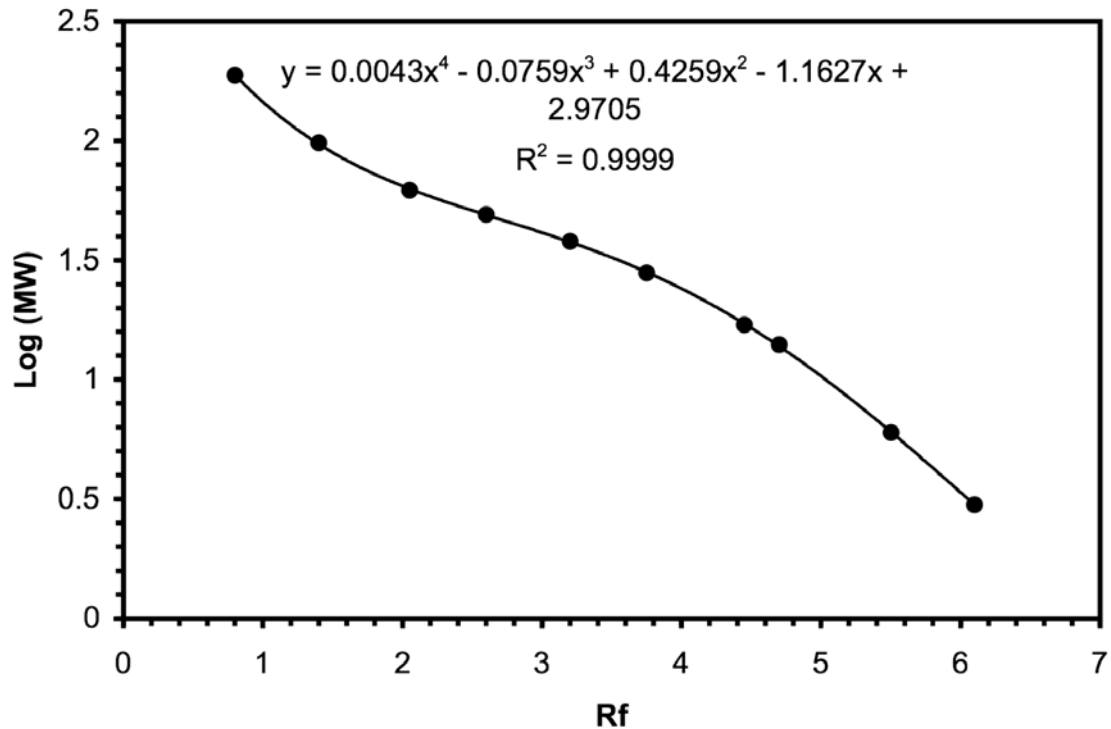
Figure 3. Plot of the log of molecular weight (MW) versus the relative mobility (R_f) or distance of migration of the components of spinach extracted PSI (unfiltered) using a polynomial fit, which ensures a higher accuracy. The data shown is the See Blue Plus 2 Molecular Weight Protein Standard on a NuPAGE 4-12% Bis-Tris gel using MES running buffer.

Table 1 displays the molecular weights observed for components of a PSI extract for all eight samples obtained. According to the molecular weights given in Table 1, all subunits of PSI are observable as well as additional components that could be a result of residues of PSII, ATP synthase, cytochrome c, etc. Mentioned earlier in Chapter I, Triton X-100 was observed to strip off the light harvesting complexes[12]. While the first sample extracted from Triton X-100 treated spinach retains the light harvesting complexes as shown in Table 1, the last samples obtained from the hydroxylapatite column specifically only contain the light harvesting complexes and nothing else. This suggests that the light harvesting complexes are stripped from the PSI, but only from the spinach extract that first comes into contact with Triton X-100 and creates a gradient throughout the column. This method could be used to obtain both fractions that contain only light harvesting complexes or a combination of PSI that has bound light harvesting complexes.

Table 1. Molecular weights (kDa) of PSI components observed in SDS PAGE using an Invitrogen NuPAGE 4-12% Bis-Tris gel run with MES buffer without filtering the spinach extract and compared to See Blue Plus 2 Molecular Weight (MW) marker (Figure 3).

Sample 1	Sample 2	Sample 3	Sample 4	Sample 5	Sample 6	Sample 7	Sample 8
145.24	145.24						
105.75	105.75						
96.77	96.77						
92.82	92.82						
79.89							
68.28							
61.34							
55.74	55.74						
51.01	53.29						
44.89	51.01						
39.36	41.16						
37.57	37.57	37.57					
32.31	32.31	32.31	32.31	32.31	32.31	32.31	
23.84	23.84			23.84	23.84	23.84	23.84
19.11	19.11	19.11	19.11	19.11	19.11	19.11	19.11
12.33	16.21	17.63	17.63	17.63			
11.18	14.85						
9.10	13.55						
6.55	9.10						
	6.55						

Upon filtering the PSI extract with a 0.2 μm syringe filter, the number of components observed in SDS-PAGE is increased for the first sample, and dramatically decreased for the following samples as seen in Table 2. However, the same trend of elimination of components except for light harvesting complexes, is similarly observed without filtering. Possibly, the smaller molecular weight components could be attributed to a loss of *PsaI*, *PsaJ*, and *PsaK*. A loss in these PSI subunits would also result in a loss of the light harvesting complexes as well as the *PsaL* and *PsaF* components that are interdependent. A loss in *PsaL* could result in a loss of *PsaH* and *PsaO*. A loss in *PsaF* could lead to a loss of the binding of plastocyanin.

Table 2. Molecular weights (kDa) of PSI components observed in SDS PAGE using an Invitrogen NuPAGE 4-12% Bis-Tris gel as shown in Figure 1 run with MES buffer after filtering the spinach extract with a 0.2 μm syringe filter from Fisher and compared to See Blue Plus 2 MW marker (Figure 3).

Sample 1	Sample 2	Sample 3	Sample 4	Sample 5
177.21				
161.36				
136.36				
126.45	126.45			
117.89				
110.44				
98.22				
90.87				
81.09				
77.83				
72.15				
69.63	69.63			
67.29				
63.00				
59.09				
57.22				
55.40	55.40			
51.84	53.61			
46.56	47.44	44.79		
37.67	39.46			
35.88	35.88	35.88	35.88	35.88
32.31				
30.54				
27.05	28.78	28.78	28.78	
22.05	25.35			
16.07				
12.24	12.24			

SUPPLEMENTAL EXPERIMENTAL RESULTS

Research Quartz Crystal Microbalance

Effect of Flow Rate on PSI Adsorption on $HOC_{11}SH$

An ultra low flow peristaltic pump (from VWR) was used in conjunction with a Maxtek Research Quartz Crystal Microbalance (RQCM) with a phase-locked oscillator and flow cell to determine the in situ adsorption of PSI onto SAM-modified Au substrates.
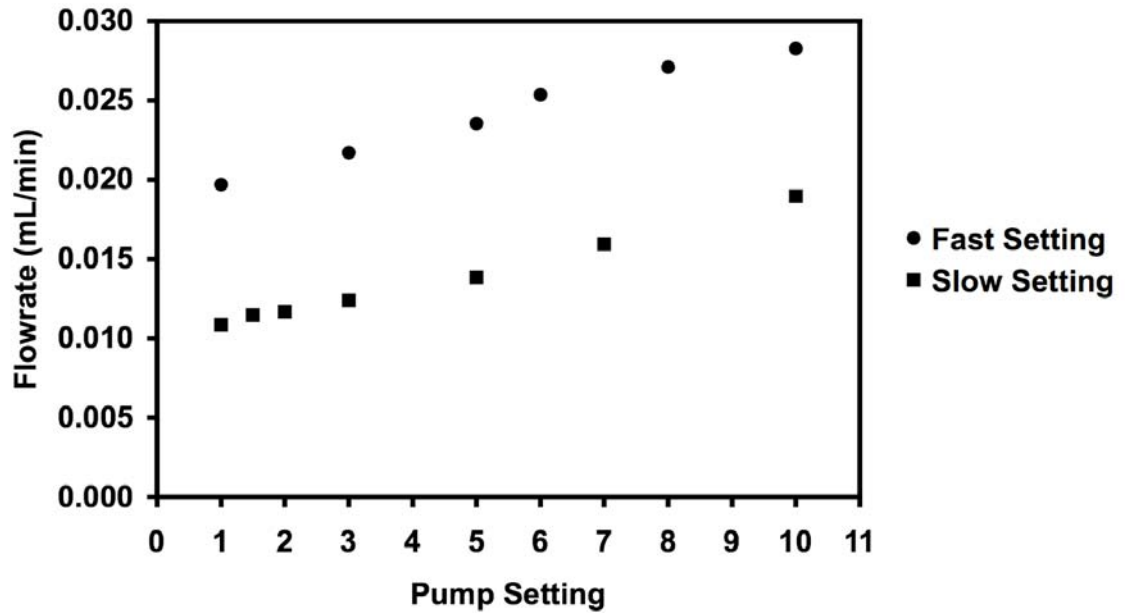
Figure 4. Pump curves for VWR ultra low flow peristaltic pump using 3/32 inch nipples and 1/16 inch tubing.

Table 3. Pump flow rates for Figure 4.

Speed	Setting	Flowrate (mL/min)
Fast	10	0.028
	8	0.027
	6	0.025
	5	0.0235
	3	0.0217
	1	0.0197
Slow	10	0.0189
	7	0.0159
	5	0.0138
	3	0.0124
	2	0.0117
	1.5	0.0115
	1	0.0109
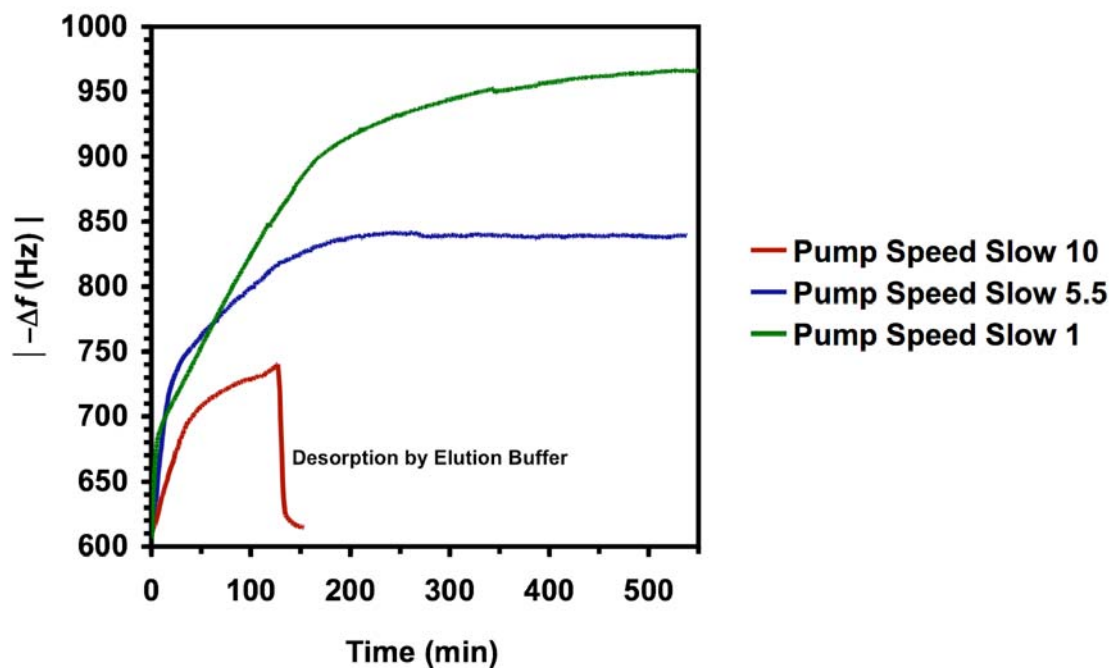
Figure 5. Effect of flow rate (found in Fig. 4 and Table 3.) on PSI adsorption on $HOC_{11}S/Au$ at room temperature. P700 concentration of 2.2 x 10^{-6} mol/L (chl concentration of 0.57 mg/mL). All measurements were done with elution buffer flowing over the $HOC_{11}S/Au$ first until reaching equilibrium and then reversing the pump and flowing PSI. Peristaltic pump was reversed and elution buffer was allowed to desorb PSI at the fastest flowrate.
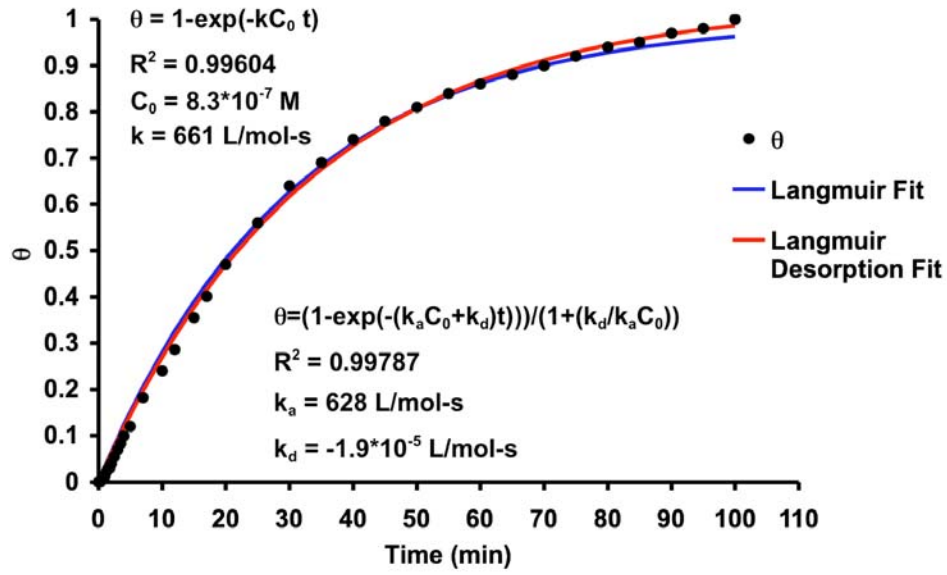
Figure 6. PSI adsorption fits from RQCM results of PSI (P700 of 8.3 x 10^{-7} mol/L) on HOC$_{11}$S/Au using 1st order Langmuir models with and without desorption.

The quartz crystal microbalance has emerged as a popular technique for monitoring interfacial events due to its ability to perform real-time, rapid, and highly sensitive measurements of resonant frequency, which can be related to film mass with nanogram sensitivity.[13] Quartz crystal resonators became a prominent analytical device after Sauerbrey's discovery in 1959 of the linear relationship between the frequency response, ΔF, and deposited mass, ΔM

$$A \, \Delta F = -C_f \, \Delta M \tag{5}$$

where C_f is a sensitivity coefficient and A is the active area of the substrate.[14] Sauerbrey's equation only holds true if the mass layer is strongly coupled to the resonator.[15]

In 1880, Pierre and Jacques Curie found that a pressure exerted on a small piece of quartz caused an electrical potential across the quartz, which is referred to as the piezoelectric effect. However, it is the converse piezoelectric effect that is used in the application of the quartz crystal microbalance, in which applying a voltage across the crystal creates a corresponding mechanical strain. When electrodes are fixed to a quartz crystal and connected to a periodic voltage source, the quartz crystal may be made to vibrate at the frequency of the exciting voltage. If the frequency of the driving voltage is very close to one of the mechanical resonances of the quartz crystal unit, the amplitude of mechanical vibration reaches a maximum. A quartz crystal resonator can be made to oscillate at one of its resonant frequencies by placing it in a feedback network of a closed loop system containing an amplifier. This is called a quartz crystal oscillator and is used to time and frequency control.

The equivalent circuit of an unperturbed piezoelectric quartz crystal resonator can be represented by a simple Butterworth-Van Dyke equivalent circuit as shown in Figure 7. A static capacitance, C_0, arises between the opposite sides of the insulating quartz.

Because the quartz is also piezoelectric, electromechanical coupling gives rise to motional contribution (L_1, C_1, R_1) in parallel with the static capacitance.[16] By modeling the equivalent circuit of the resonator, mathematical equations can be applied to solve for mass adsorption as it corresponds to the change in frequency.

Kanazawa and Gordon have shown that operating the QCM in solution will cause a change in frequency due to the viscous coupling of the liquid to the oscillating device, thus yielding a false sense of mass adsorption. The resonant frequency is affected by both mass and liquid loading, and simple measurement of the resonant frequency alone cannot separate the two.[16] By fitting a circuit model and measuring the change in resistance along with the change in frequency, mass and liquid effects can be separated. As seen in Figure 7, liquid loading causes an increase in inductance and resistance, whereas mass loading only increases the inductance.[16]

Kanazawa and Gordon developed the first equation relating density and viscosity effects to the change in frequency[17]

$$\Delta f = -f_0^{3/2} \left(\eta_L \rho_L / \pi \mu_Q \rho_Q \right)^{1/2} \tag{6}$$

where f_0 is the oscillation frequency of the dry crystal, η_L and ρ_L is the absolute viscosity and density of the fluid, and μ_Q and ρ_Q is the elastic modulus and density of the quartz crystal.
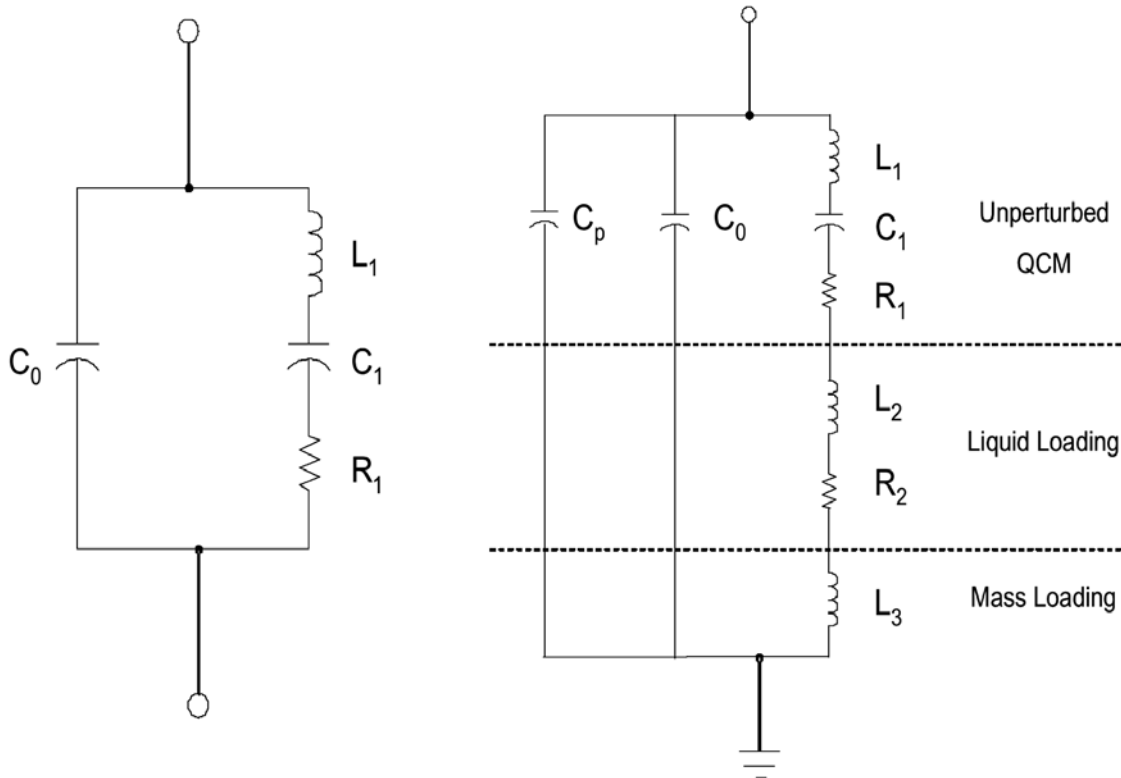
Figure 7. Butterworth Van Dyke equivalent circuit (left) and a circuit model used to separate mass and liquid effects as proposed by Martin, Granstaff, and Frye.[16]

186
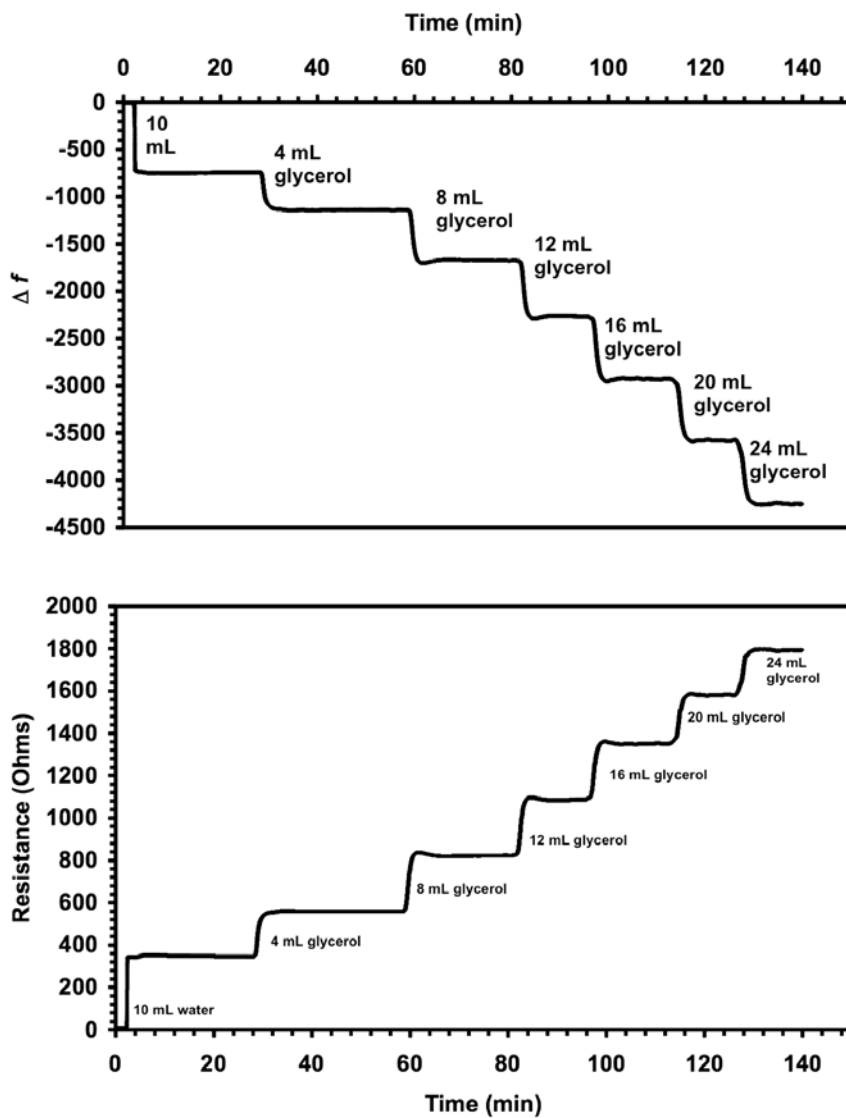
Figure 8. Resistance and frequency change on Au coated QCM with the addition of glycerol in 4 mL step progression. Starting initially with 10 mL of deionized water and then adding 4 mL of glycerol to increase total volume sequentially.
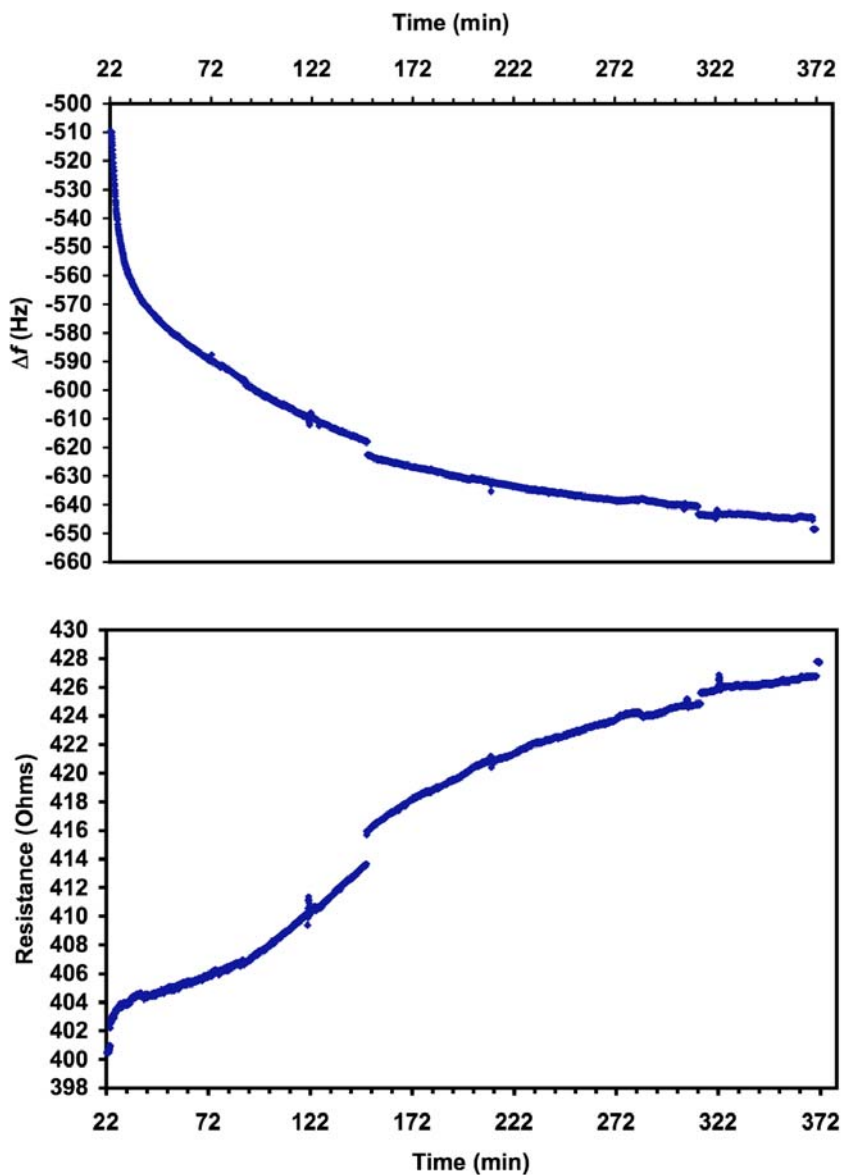
Figure 9. Corresponding change in frequency and resistance for a NHS-modified $HO_2C_{11}S/Au$ substrate after adsorption of PSI (P700 concentration of 7.3×10^{-7} mol/L) at room temperature following equilibrium adsorption of elution buffer at pump speed slow of 5.5.
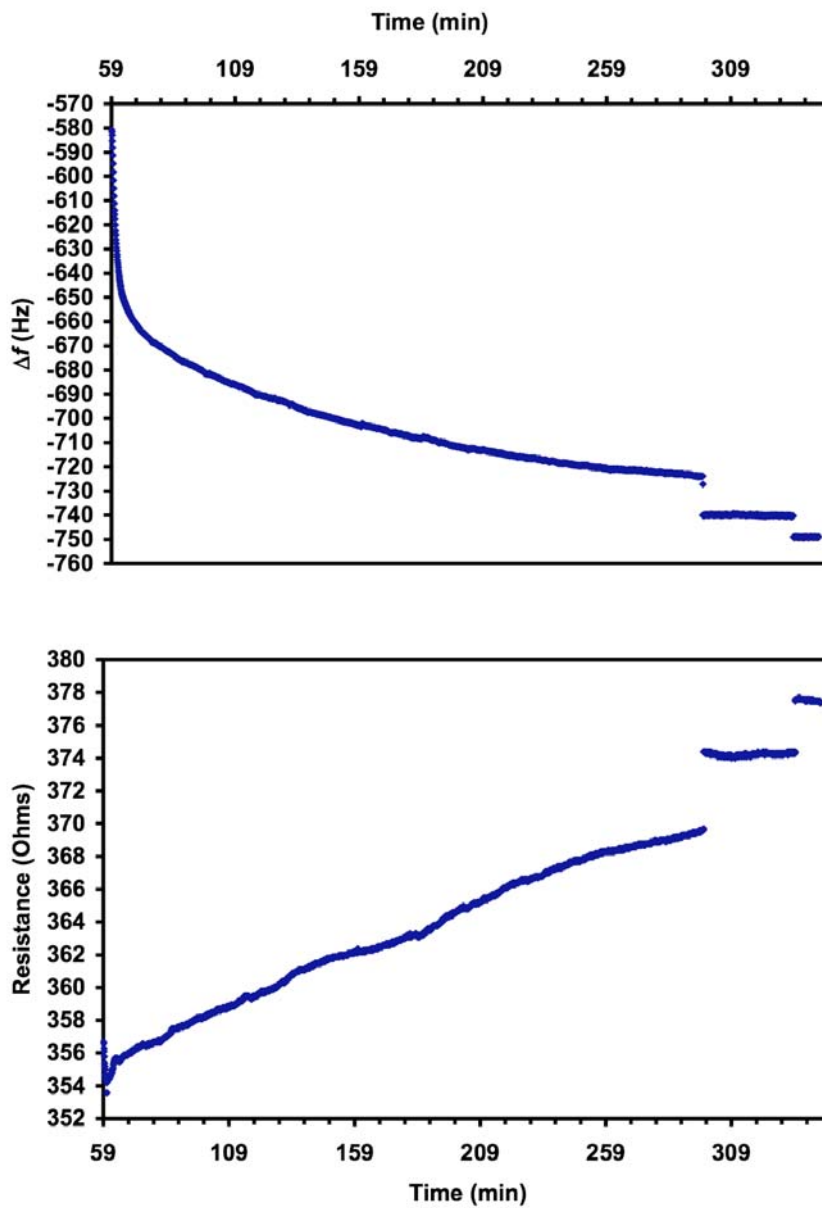
Figure 10. Corresponding change in frequency and resistance for a $HO_2C_{11}S/Au$ substrate after adsorption of PSI (P700 concentration of 7.3 x 10^{-7} mol/L) at room temperature following an equilibrium adsorption of elution buffer at a pump speed slow of 5.5.
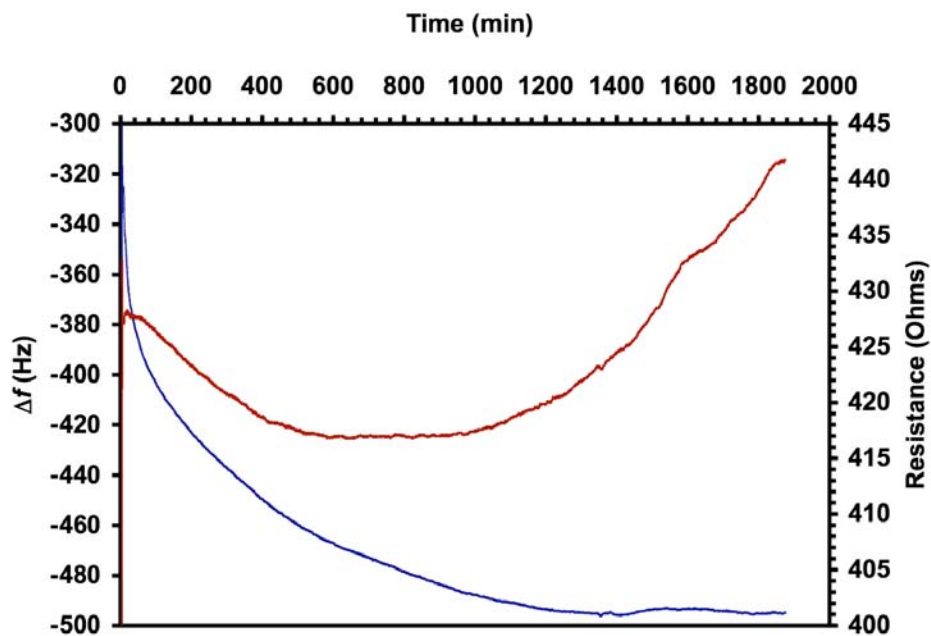
Figure 11. Overnight 2-aminoethanethiol on Au polished quartz crystal after adsorption of PSI (P700 concentration of 1.02 x 10^{-6} mol/L) at room temperature and run at 50% speed on the cytosensor to help eliminate bubbles. Blue curve is the change in frequency, while the red curve is the change in resistance.

190

Both ellipsometry and RAIRS was performed on PSI-modified $HOC_{11}S/Au$ substrates when PSI was allowed to adsorb at 4°C for 4 h and 24 h and then taken out of solution and left in air over the course of 24 days.
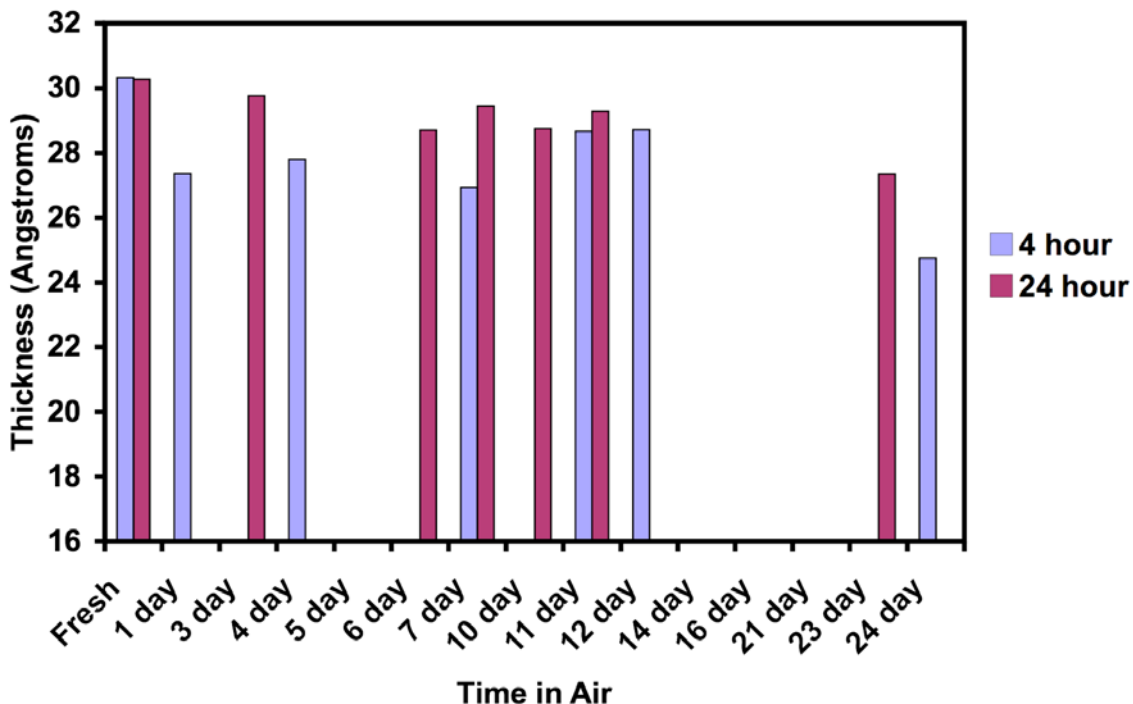
Figure 12. SE thickness of PSI (diluted in half with water to final P700 concentration of 3.33×10^{-6} mol/L) and monitoring effect of adsorption time of PSI in refrigerator and the effect when leaving the PSI-modified $HOC_{11}S/Au$ substrate sample in air over time. SE data taken at 82°, 83°, 84° using a refractive index of 1.46 (so thicknesses are underestimated since the refractive index of PSI is 1.33).

191
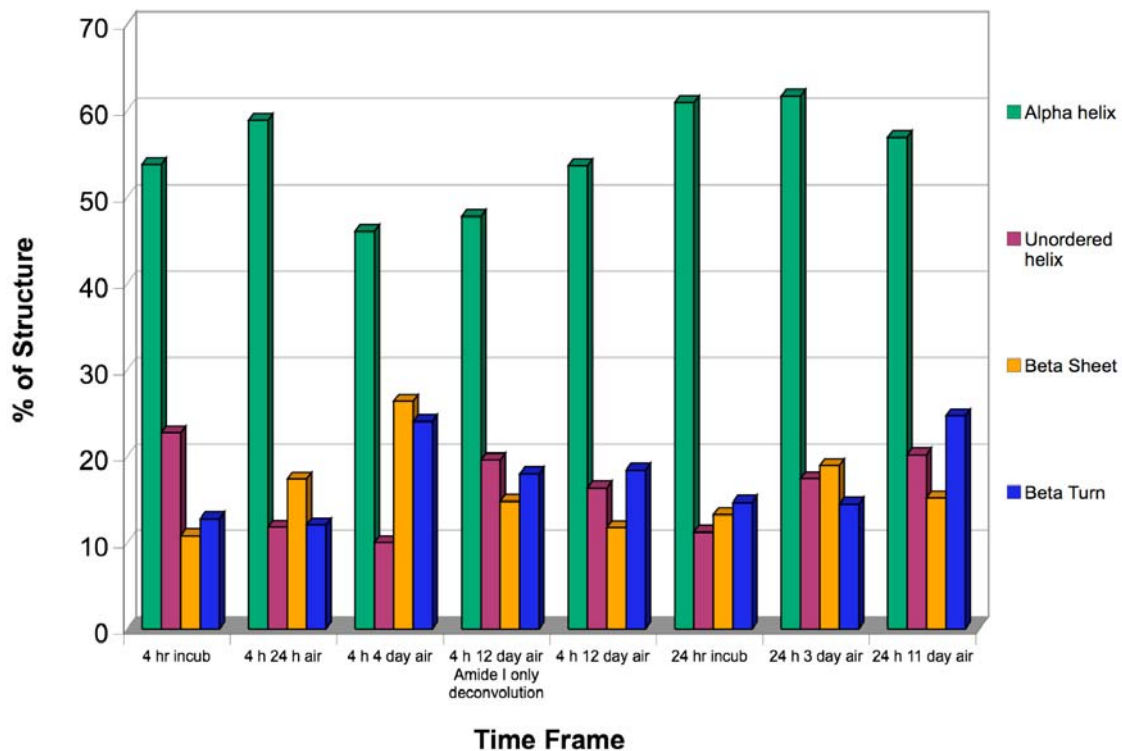
Figure 13. Secondary structure of PSI samples (from Figure 11) after exposure to air as determined by deconvolution of the Amide I band of RAIR spectra. The first five sets represent the change of the 4 h PSI adsorbed $HOC_{11}S/Au$ substrate in air, while the last three sets represent the change of the 24 h PSI adsorbed $HOC_{11}S/Au$ substrate in air.

Methyl Viologen Cyclic Voltammograms
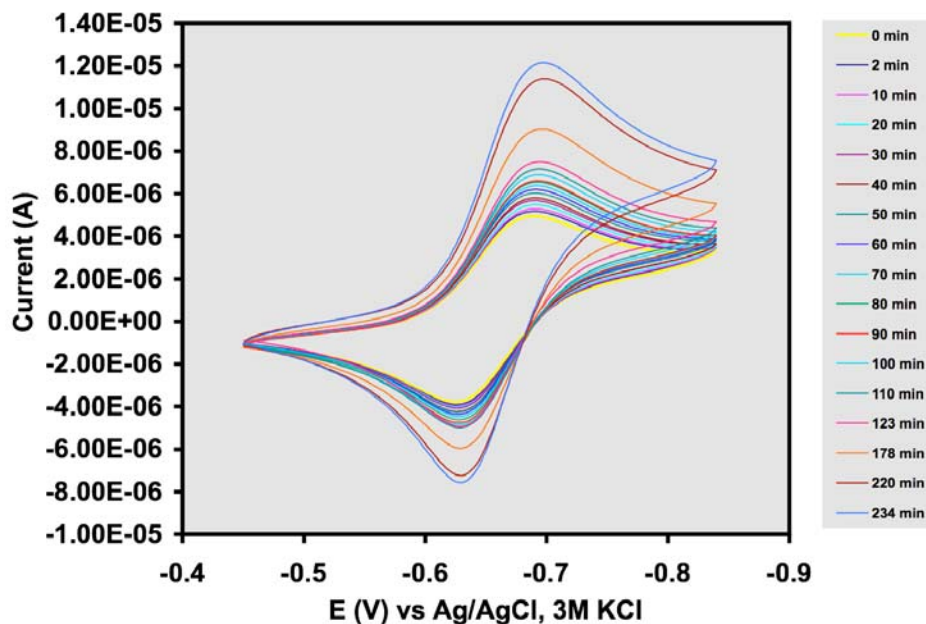
Figure 14. CV of NHS-modified $HO_2C_{11}S/Au$ disk electrode after PSI adsorption as a function of blue light at an intensity of ~20 to 30 W in 1mM methyl viologen in 0.5 M phosphate buffer pH 7.0.
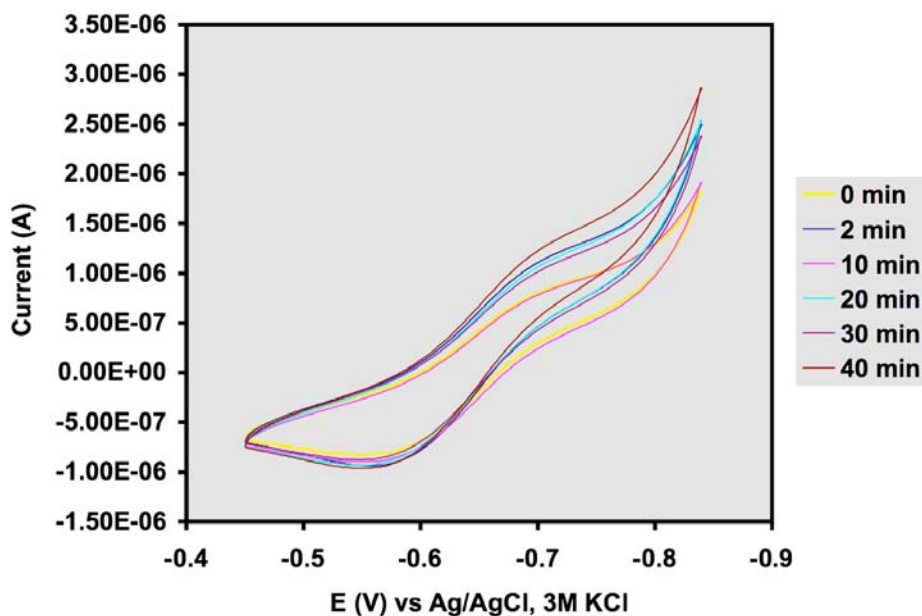

Figure 15. CV of $H_3CC_{11}S/Au$ disk electrode after PSI adsorption as a function of blue light at an intensity of ~20 to 30 W in 1mM methyl viologen in 0.5 M phosphate buffer pH 7.0.
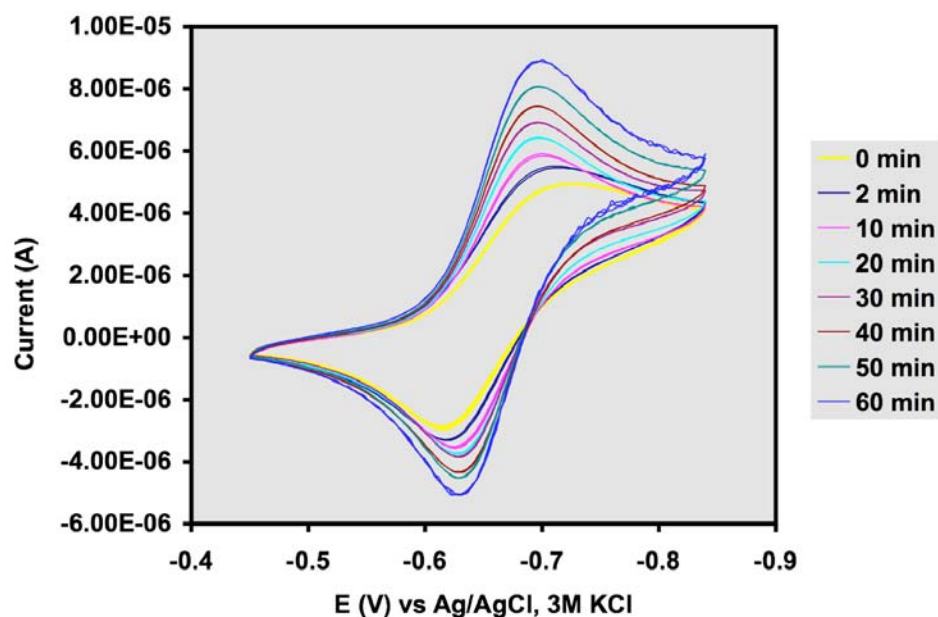
Figure 16. CV of HOC$_{11}$S/Au disk electrode after PSI adsorption as a function of blue light at an intensity of ~20 to 30 W in 1mM methyl viologen in 0.5 M phosphate buffer pH 7.0.
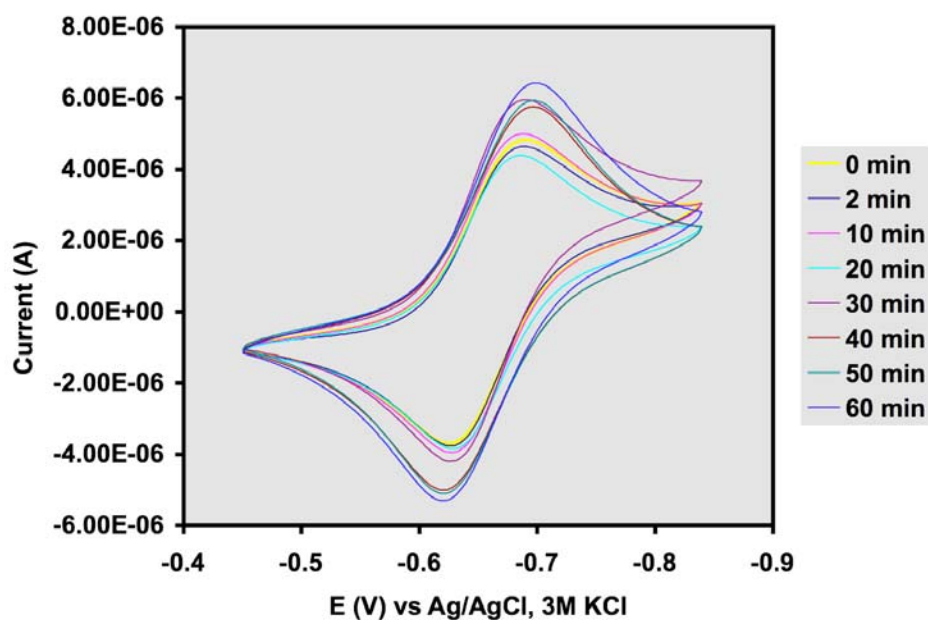

Figure 17. CV of HO$_2$C$_{11}$S/Au disk electrode after PSI adsorption as a function of blue light at an intensity of ~20 to 30 W in 1mM methyl viologen in 0.5 M phosphate buffer pH 7.0.
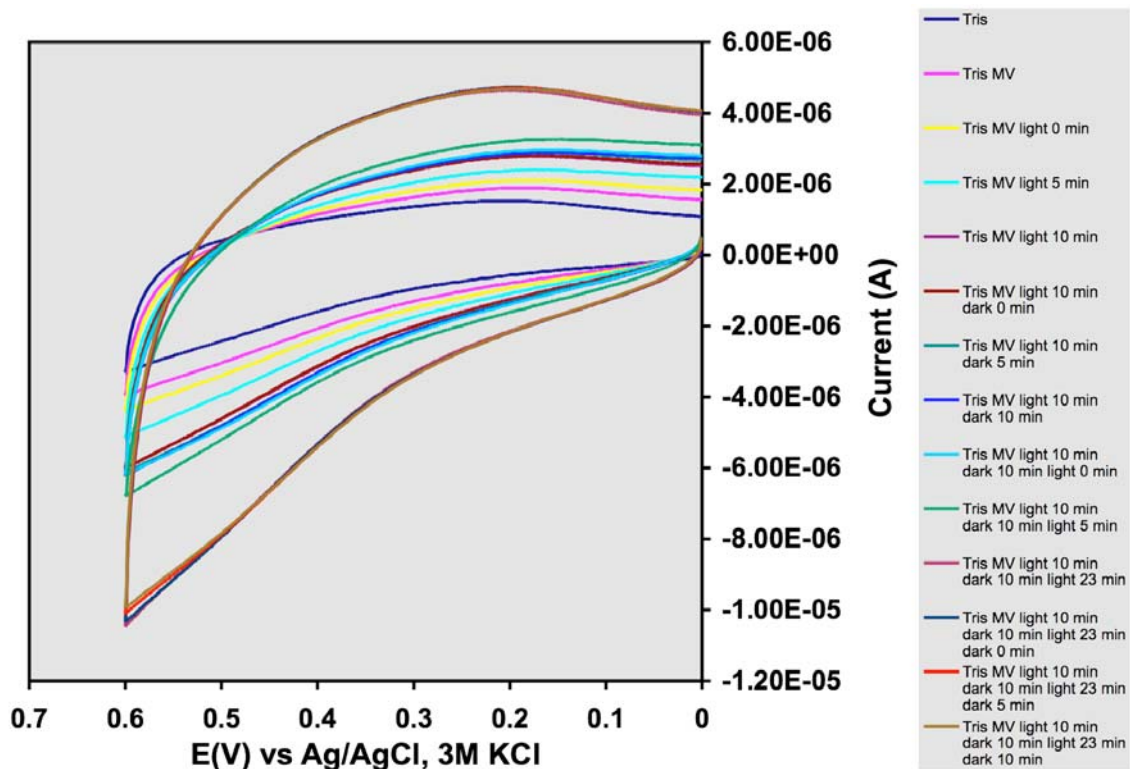
Figure 18. CVs of PSI adsorbed onto HOC$_6$S/Au flat substrates in the presence of 0.25 mM methyl viologen in 50 mM Tris buffer with light and dark cycles of ~20 to 30 W intensity at a scan rate of 0.25 V/s. (Current increases)
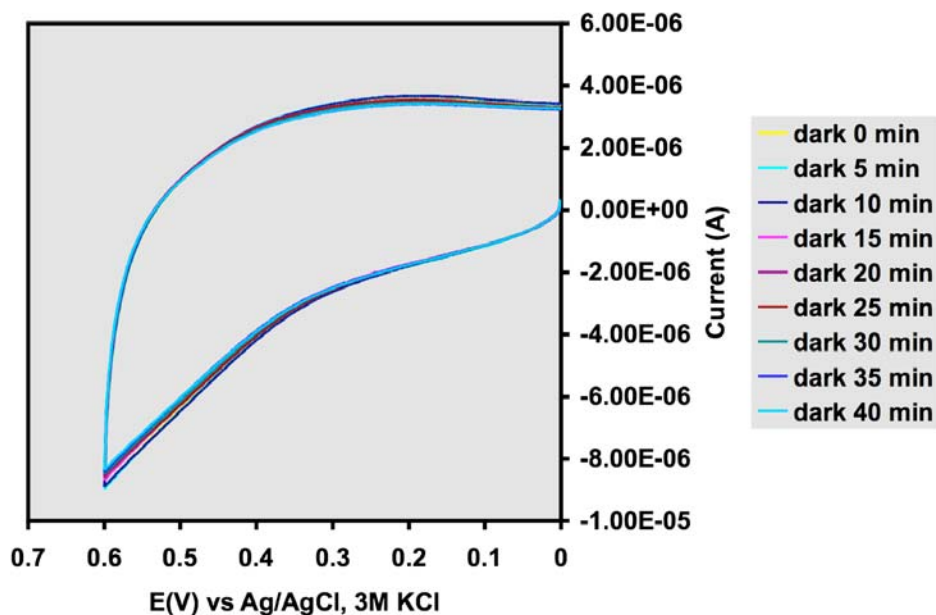

Figure 19. CVs of PSI adsorbed onto HOC$_6$S/Au flat substrates in the presence of 0.25 mM methyl viologen in 50 mM Tris buffer in the dark at a scan rate of 0.25 V/s. (Current decreases)

195
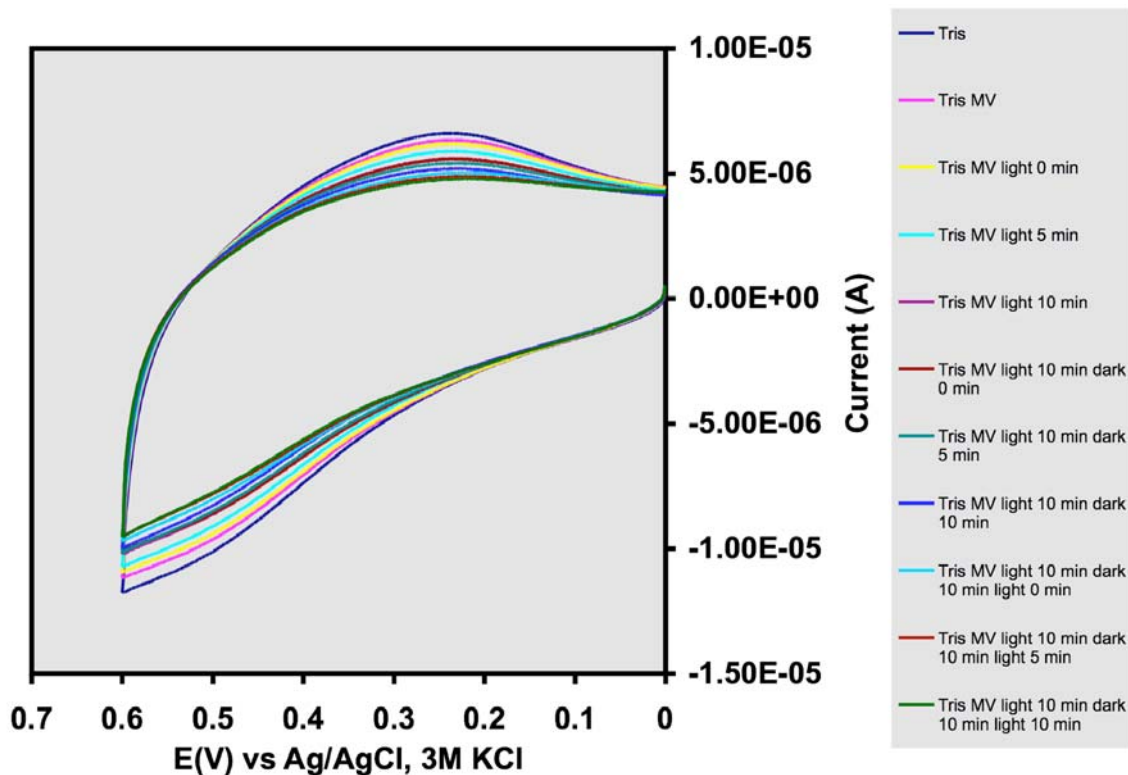
Figure 20. CVs of elution buffer adsorbed onto HOC$_6$S/Au flat substrates in the presence of 0.25 mM methyl viologen in 50 mM Tris buffer with light and dark cycles of ~20 to 30 W intensity at a scan rate of 0.25 V/s. (Current decreases)

<u>Effect of Triton Concentration on PSI Adsorption on Various Au Modifications</u>

It was hypothesized that the adsorption of Triton X-100 controls the mechanism for the adsorption of the membrane protein, PSI. In order to support this hypothesis, the adsorption of PSI was studied under conditions where the concentration of Triton X-100 is above and below the critical micelle concentration (cmc of ~ 0.2 mM).
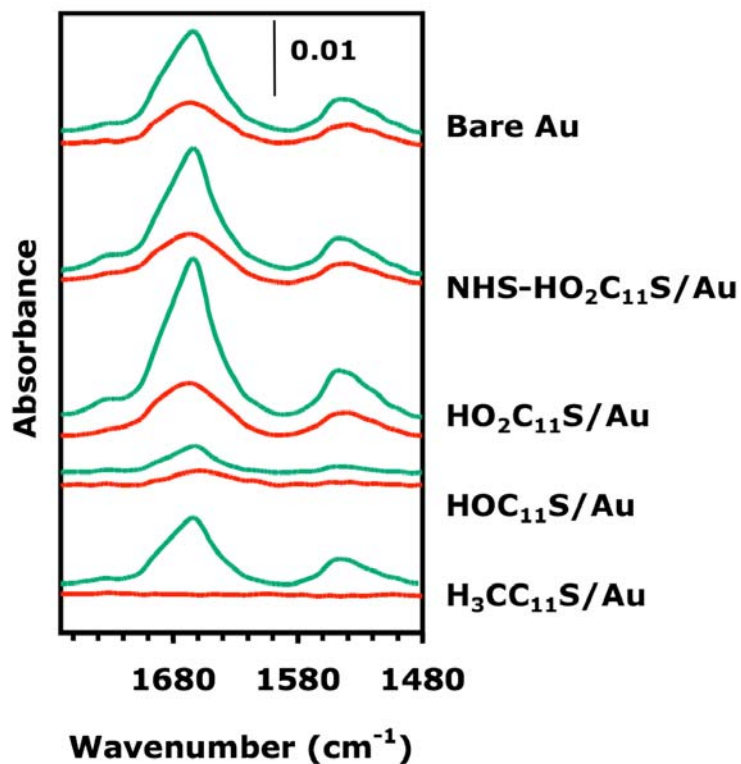

Figure 21. RAIR spectra of the Amide I and II bands of 1 month PSI adsorption when Triton X-100 concentration is above the cmc (green curves) at 0.773 mM by diluting PSI concentration with elution buffer and below the cmc (red curves) to 0.03 mM by diluting PSI with 0.2M phosphate buffer at pH 7. Adsorption at 4°C on various surface modifications of Au and spectra are offset for clarity.

When the Triton X-100 concentration is below the cmc, PSI will adsorb onto a methyl-terminated surface. However, when the surfactant concentration is above the cmc, Triton X-100 forms a dense bilayer and prevents PSI adsorption.

References

1.   Raghavendra, A. S., *Photosynthesis: A Comprehensive Treatise*. Cambridge University Press: 1998.

2.   Pessarakli, M., *Handbook of Photosynthesis*. Marcel Dekker: New York, 1996.

3.   Reeves, S. G.; Hall, D. O., Higher Plant Chloroplasts and Grana: General Preparative Procedures (Excluding High Carbon Dioxide Fixation Ability Chloroplasts). In *Methods in Enzymology*, Colowick, S. P.; Kaplan, N. O., Eds. Academic Press: New York, 1980; Vol. 69, pp 85-94.

4.   Baba, K.; Itoh, S.; Hastings, G.; Hoshina, S., Photoinhibition of Photosystem I Electron Transfer Activity in Isolated Photosystem I Preparations with Different Chlorophyll Contents. *Photosynthesis Research* **1996,** 47, 121-130.

5.   Arnon, D. I., Copper Enzymes in Isolated Chloroplasts, Polyphenoloxidase in *Beta Vulgaris*. *Plant Physiology* **1949,** 24, (1), 1-15.

6.   Shiozawa, J. A.; Alberte, R. S.; Thornber, J. P., The P700-Chlorophyll a -Protein: Isolation and Some Characteristics of the Complex in Higher Plants. In *Archives of Biochemistry and Biophysics*, Academic Press: 1974; Vol. 165, pp 388-397.

7.   Markwell, J. P.; Thornber, J. P.; Skrdla, M. P., Effect of Detergents on the Reliability of a Chemical Assay for P-700. *Biochimica Et Biophysica Acta* **1980,** 591, (2), 391-399.

8.   Shapiro, A. L.; Vinuela, E.; Maizel, J. V., Jr., Molecular Weight Estimation of Polypeptide Chains by Electrophoresis in SDS-Polyacrylamide Gels. *Biochemical and Biophysical Research Communications* **1967,** 28, (5), 815-820.

9.   Hames, B.; Rickwood, D., *Gel Electrophoresis of Proteins*. IRL Press: Washington, DC, 1981; Vol. 1, p 1-33.

10.   Frank, R. N.; Rodbard, D., Precision of Sodium Dodecyl Sulfate-Polyacrylamide-Gel Electrophoresis for the Molecular Weight Estimation of a Membrane Glycoprotein: Studies on Bovine Rhodopsin. *Archives of Biochemistry and Biophysics* **1975,** 171, (1), 1-13.

11.   Allen, R. C.; Budowle, B., *Gel Electrophoresis of Proteins and Nucleic Acids: Selected Techniques*. Walter de Gruyter: Berlin; New York, 1994; p 338.

12.   Horspool, W. M.; Song, P.-S., *CRC Handbook of Organic Photochemistry and Photobiology*. CRC Press, Inc.: 1994.

13.   Lee, S. W.; Hinsberg, W. D., Determination of the Viscoelastic Properties of Polymer Films using a Compensated Phase-Locked Oscillator Circuit. *Analytical Chemistry* **2002,** 74, (1), 125-131.

14.   Buttry, D. A., *Applications of the Quartz Crystal Microbalance to Electrochemistry*. Marcel Dekker: New York, 1992; Vol. 17.

15.   Janshoff, A.; Galla, H.-J.; Steinem, C., Piezoelectric Mass-Sensing Devices as Biosensors - An Alternative to Optical Biosensors? *Angewandte Chemistry International Edition* **2000,** 39, 4004-4032.

16.   Martin, S. J.; Granstaff, V. E.; Frye, G. C., Characterization of a Quartz Crystal Microbalance with Simultaneous Mass and Liquid Loading. *Analytical Chemistry* **1991,** 63, (20), 2272-2281.

17.   Kanazawa, K. K.; Gordon, J. G., The Oscillation Frequency of a Quartz Resonator in Contact with a Liquid. *Analytical Chimica Acta* **1985,** 175, 99-105.